Characterising the marine atmospheric boundary layer with spaceborne SAR

Owen P. O'Driscoll

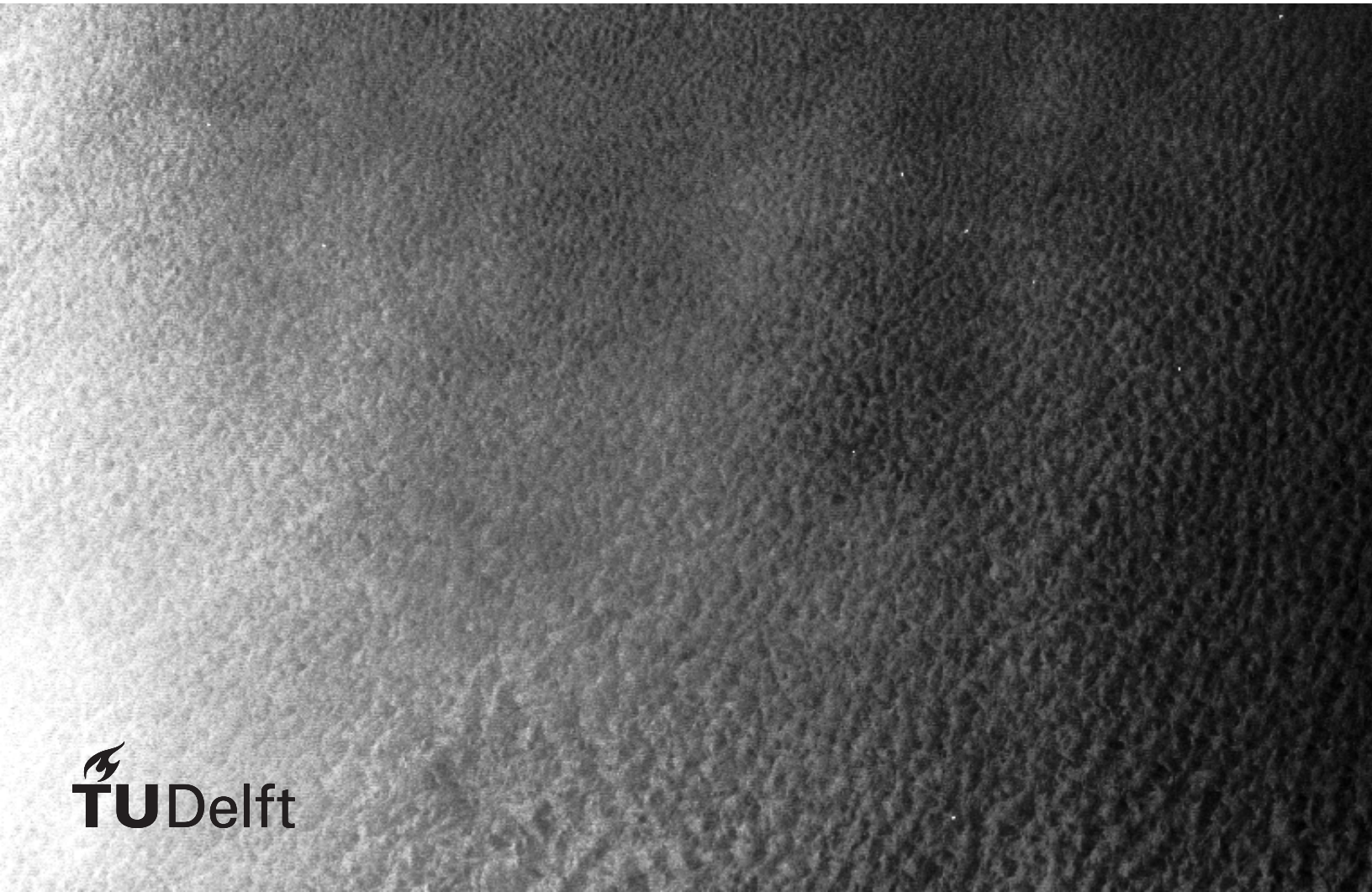

TU Delft

Characterising the marine atmospheric boundary layer with spaceborne SAR

by

Owen P. O'Driscoll

to obtain the degree of Master of Science

at the Delft University of Technology,

to be defended publicly on September 29th, 2021 at 16:00.

Student number:	4592611	
Project duration:	March 1st, 2021 – September 29th, 2021	
Thesis committee:	Dr. ir. Paco López-Dekker,	TU Delft, chairman
	Dr. Marcel Kleinherenbrink,	TU Delft, supervisor
	Dr. Louise Nuijens	TU Delft
	Dr. Sukanta Basu	TU Delft

An electronic version of this thesis is available at http://repository.tudelft.nl/.

Cover image contains Sentinel-1 SAR amplitude image of the ocean surface from an area off the coast of Portugal, taken on December 9th, 2020.

TU Delft

Preface

This project was carried out to obtain a master's degree from the Geoscience and Remote Sensing department at the TU Delft Civil Engineering and Geosciences faculty. The nature of this project captures both the geoscience (ocean-atmosphere interactions) and remote sensing (spaceborne radar observations) aspects of the study track.

Quite a few people have supported me during this project. In particular I would like to thank Louise Nuijens and Sukanta Basu for sharing their precious time, suggestions and expertise while dealing with my (often ill-phrased) questions. Also thanks to Lorenzo Iannini and Andreas Theodosiou for helping me out with technical matters even when the wise sages of various internet fora were without answers.

There is no way I can avoid thanking my friends and family for their ongoing support over the past few months, or for that matter, during my entire academic career. Special thanks to Estela for her timely distractions and for our pleasant "thesis competition".

And of course many thanks to my supervisors Paco López-Dekker and Marcel Kleinherenbrink. While continuously pointing out the right direction, they surely made these last few months both a unique and delightful experience!

Owen P. O'Driscoll
Delft, September 2021

Abstract

Oceans play a vital role in the regulation of Earth's intricate climate system. The majority of gas and energy exchanges occurring at the ocean-atmosphere interface are driven by small-scale, $\mathcal{O}(1\text{ km})$, coupled processes. Despite its importance, too few observations have been able to capture the ocean-atmosphere coupling at scales smaller than $\mathcal{O}(10\text{ km})$. This has led to poor parameterisation in climate models. In an effort to enhance our understanding of the ocean-atmosphere coupling, this study aims to test and improve upon two separate Marine Atmospheric Boundary Layer (MABL) characterisation methodologies (called algorithm 2A and algorithm 2B) put forward by Young et al. (2000). Algorithms 2A and 2B relate processed Synthetic Aperture Radar (SAR) image properties to a specific atmospheric state through use of surface-layer similarity theory and a combination of surface-layer and mixed-layer similarity theory respectively. Results of both methods indicate significant inherent limitations. Algorithm 2A's utility is curbed by uncertainty introduced during the estimation of Convective Boundary Layer depth Z_i and spectral power-law extrapolation. Algorithm 2B suffers from uncertainty introduced by the dimensionless energy dissipation rate ψ. As a result of these (and other) uncertainties, the estimated atmospheric instability can be off by a factor 2 or more. Further analyses suggest shortcomings in the applicability of the Geophysical Model Function (GMF). It is hypothesised that both employed GMFs underestimate the horizontal wind-field variance at scales relevant to turbulent convection, which subsequently manifests itself as (part of) the observed average 50% overestimation of absolute Obukhov length and subsequent 33% underestimation of the atmospheric instability. Additional research is required to support and quantify the GMF-induced underestimation hypothesis. Inspired by algorithm 2B, a third method (algorithm 2C) is developed which circumvents major uncertainties inherent to both algorithm 2A and 2B. However, due to limitations of its own, algorithm 2C is incapable of replacing algorithms 2A or 2B for a large range of atmospheric instabilities. If improved upon and successfully employed, spaceborne characterisation of the MABL could benefit climate studies by providing a wealth of continuous and global atmospheric-state measurements on scales previously unavailable.

Contents

Nomenclature

Abbreviations

$\mathcal{O}$	Order of magnitude
CBL	Convective Boundary Layer
CMOD	C-band Model
CNN	Convolutional Neural Network
DFT	Discrete Fourier Transform
ECMWF	European Centre for Medium-Range Weather Forecasting
ERA5	ECMWF Reanalysis 5th Generation
ESA	European Space Agency
GMF	Geophysical Model Function
GOES − E	Geostationary Operational Environmental Satellite-East
GRD	Ground Range Detected
IW	Interferometric Wide swath mode
ln	Natural Logarithm
MABL	Marine Atmospheric Boundary Layer
MAD	Median of Absolute Deviation
MOST	Monin-Obukhov Similarity Theory
NRCS	Normalised Radar Cross Section
PSD	Power Spectral Density
RMSE	Root Mean Square Error
S1 OCN	Sentinel-1 Ocean product
S1	Sentinel-1
SAR	Synthetic Aperture Radar

SNAP	Sentinel Application Platform	
TKE	Turbulent Kinetic Energy	
p	Probability of erroneously rejecting the null hypothesis	

Constants

α	Kolmogorov constant	0.5
β	Isotropy correction factor	1 or $\frac{4}{3}$
κ	Von Kármán constant	0.4
ν	Kinematic viscosity of air	1.5×10^{-5} m^2 s^{-1}
π	Pi	3.141592
ρ_{air}	Air density	1.2 kg m^{-3}
a	Charnock constant	0.011
C_p	Heat capacity air	1005 J kg^{-1} K^{-1}
g	Gravitational acceleration	9.8 m s^{-2}

Variables

χ	Stability correction factor	
$\Delta\xi$	Frequency bin width	Hz
ϵ	TKE dissipation rate	m^2 s^{-3}
$\overline{w'T'}$	Heat flux, kinematic	K m s^{-1}
ϕ	Scatterometer incidence angle	$^\circ$
ϕ_ϵ	Dimensionless gradient profile function	
ψ	Dimensionless energy dissipation rate	
ψ_m	Profile function	
σ_u	Horizontal wind-field standard deviation	m s^{-1}
τ	Surface stress	N m^{-2}

θ	Scatterometer look direction w.r.t. wind direction	$^\circ$
ξ	Spatial frequency	m^{-1}
C_{dn}	Drag coefficient, neutral	
C_d	Drag coefficient	
C_H	Heat transfer coefficient	
E	Heat flux, latent	$\mathrm{W\ m}^{-2}$
$E(...)$	Energy spectrum	A^2
$F(...)$	Frequency spectrum	A
f_i	Dimensionless frequency	
H	Heat flux, sensible	$\mathrm{W\ m}^{-2}$
L	Obukhov length	m
L_v	Latent heat of vaporisation	$\mathrm{J\ kg}^{-1}$
N	Number of samples	
n	Temporal frequency	s^{-1}
R	Specific humidity	$\mathrm{kg\ kg}^{-1}$
r	Specific humidity	$\mathrm{g\ kg}^{-1}$
$S(...)$	Power Spectral Density	$\mathrm{A}^2\ \mathrm{Hz}^{-1}$
T_0	Water surface temperature	approximated by 293 K
T_v	Virtual potential temperature	approximated by 293 K
T_{10}	Temperature at 10 metres	K
T_{SST}	Water surface temperature (saildrone)	K
U	Wind speed	$\mathrm{m\ s}^{-1}$
$u,\ v,\ w$	Parallel, perpendicular and vertical wind components respectively	$\mathrm{m\ s}^{-1}$
u_*	Friction velocity	$\mathrm{m\ s}^{-1}$

w_*	Convective velocity scale	m s^{-1}
x	Profile function empirical constant	
z	Measurement height	m
z_0	Aerodynamic roughness length	m
Z_i	CBL depth	m
δ	Wind direction, clockwise from north	$^\circ$

Introduction

1.1 Research relevance

Climate is regulated by the oceans, which combined cover over 70% of the Earth's surface (NOAA, 2020). Ocean warming accounts for over 90% of the Earth's energy inventory increase between 1971 and 2010, where the majority of excess energy storage occurs in the upper 700 m of the ocean (IPCC, 2013). The gas and energy exchanges occurring between the Marine Atmospheric Boundary Layer (MABL) and the water surface are vital for climate descriptions (Smith et al., 1996). The dominant convective processes within a MABL in which vertical transport of air parcels attempts to re-establish equilibrium (i.e. an unstable MABL) are structured as microscale, $\mathcal{O}(< 3$ km) (Stull, 1988), two-dimensional rolls and three-dimensional cells (Sikora and Ufermann, 2004). Sikora and Ufermann (2004) notes three domains for which MABL convection is important. Firstly, on the micro- to mesoscale (2 km to 2,000 km) MABL convection can directly affect meteorological conditions. Secondly, on the meso- to macroscale (2,000 km to 20,000 km) the fluxes induced by MABL convection are critical for weather forecasting. Lastly, on long temporal scales the statistical properties of MABL convection (such as occurrence frequency and induced flux) are important for global climate modelling. The range in spatial and temporal scales of these domains highlights the impact of MABL convection on processes orders of magnitude greater than that of the MABL itself.

In light of current climate research, the impact of MABL convection on large temporal and spatial scales is particularly important. The Earth system contains a host of intricate feedback loops and non-linear couplings between processes occurring at different temporal or spatial scales (ESA, 2020). For example, the majority of energy transport and gas fluxes between the ocean and atmosphere are driven by small-scale, $\mathcal{O}(1$ km), coupled processes (ESA, 2020). The complexity and scale of these processes necessitates parameterisation in climate models (Trindade et al., 2019; ESA, 2020). Due to a lack of high-quality observations with which to constrain models, the parameterisation of these small-scale processes is among the main sources of uncertainty for climate projections (Trindade et al., 2019; ESA, 2020). Thus, by continuous and successful characterisation of the MABL, an improved parameterisation of the air-sea coupling can be achieved which by extension leads to improved global climate models.

1.2 Research aim

Synthetic Aperture Radar (SAR) observations of the oceans are used for a multitude of scientific and civil purposes. Its all-weather capability makes it a suitable tool for ship and oil spill detection, sea ice monitoring, wind field mapping, wave spectrum retrieval, studying tropical cyclones and near-shore bathymetry estimation (Alpers and Hennings, 1984; Vachon et al., 2004, 2012; Foster, 2013; Wiehle et al., 2019). Unlike the coarser $\mathcal{O}(10$ km) resolution of scatterometers, the $\mathcal{O}(100$ m) resolution of SAR observations allows it to resolve scales relevant to MABL-induced convection (at the cost of directional ambiguity). Two-dimensional rolls and three-dimensional cells alter the local wind field. The altered wind fields whip up surface waves which leads to increased surface roughness and stronger backscatter of the emitted radio wave (Hersbach, 2008), leaving identifiable roughness patterns visible to SAR. Through observing these MABL-induced roughness patterns one can derive several properties of the MABL state. Gerling (1986) and Zecchetto et al. (1998) derive wind direction from two-dimensional rolls and three-dimensional cells respectively, Wackerman et al.

(1996) estimates the depth of the convective part of the MABL, i.e. the Convective Boundary Layer (CBL) depth, using two-dimensional rolls, Sikora et al. (1997) estimates the CBL depth using three-dimensional cells and Quilfen et al. (1998) estimates the wind field within tropical cyclones using a Geophysical Model Function (GMF). A GMF relates the intensity of the backscattered signal to surface stress and, in turn, an estimated wind speed. Young et al. (2000) displays the possibility of inferring several MABL properties from SAR data by extracting spectral statistics from the convection-induced roughness patterns. ESA's Sentinel-1 mission has acquired millions of ocean covering SAR observations since launch (Wang et al., 2019a). Applying Young's methodology on this vast archive of data could yield new insights into the air-sea interactions between the ocean and the atmosphere. The aim of this study is to test the characterisation of the MABL using SAR data. This characterisation consists of the estimation of wind direction, average wind speed, friction velocity, horizontal wind-field variance, CBL depth and Obukhov length. Of particular interest are the latter three parameters as these cannot be derived on relevant scales with contemporary scatterometers. Successful derivation of these parameters can aid the calibration of ocean-atmosphere coupling models by providing global, near real-time MABL information on horizontal scales previously unavailable.

1.3 Research question

The main research question of this study is

"To what extent is it feasible to characterise the state of the marine atmospheric boundary layer over the ocean by means of spectral analysis of Sentinel-1 SAR amplitude observations?"

1.4 Research sub-questions

In order to answer the main question, the following sub-questions are addressed

1. *What imprints does the MABL leave on the water surface?*

   Both oceanic and atmospheric processes determine the water-surface structure (Young et al., 2000). In order to characterise the MABL it must first be understood what signatures it leaves on the water surface.

2. *Can the imprints caused by the MABL be separated from other signal sources?*

   The horizontal scale of oceanographic and atmospheric phenomena overlap (Young et al., 2000). Perfect separation of the individual signal components is not always possible. The relevant signals have to be separated in order to perform further analyses.

3. *Are the employed GMFs capable of estimating the MABL-induced wind-field variations?*

   GMFs are used to relate the radar backscatter intensity to wind fields. Originally designed for the estimation of average wind speeds on $\mathcal{O}(10$ km$)$ scales, it is hypothesised that these GMFs may fail to accurately estimate wind-field slopes for resolutions two orders of magnitude higher, e.g. $\mathcal{O}(0.1$ km$)$. The GMF assumes the surface stress to be caused by a wave field at a particular development stage. However, the rapidly changing wind fields prevailing during turbulent convection may prevent the wave fields from reaching the development stage implicitly assumed by the GMF, which would result in the

derived wind fields failing to capture the convection-induced wind-field variability. If indeed the case, failure of the GMFs is expected to lead to underestimation of the variability occurring at scales relevant to turbulent convection and thus underestimation of the horizontal wind-field variance.

4. *How can the MABL's imprints be related to a MABL state?*

   Once the MABL-induced water-surface signatures have been isolated and transformed into a representative wind field, it must be related to characteristics of a specific MABL state. Different empirical relations should enable this connection. An understanding of the shallow atmosphere is required in order to select and implement the correct empirical relations whilst taking into account their respective limitations.

1.5 Research outline

Relevant background information regarding the MABL, its imprints on the water surface, the SAR measuring tool and GMFs are described in section 2. The methodology to retrieve MABL properties from SAR observations is described in section 3 with an in-depth description of the study areas and validation data following in section 4. Characterisation results for these study areas and a discussion of said results are provided in section 5. Conclusions regarding the characterisation performance are presented in section 6, along with recommendations.

Background

2.1 Marine Atmospheric Boundary Layer

Stull (1988) and Sikora and Ufermann (2004) describe the MABL as that part of the atmosphere directly influenced by the surface. Smith et al. (1996) describes the atmospheric boundary layer as the turbulent zone between the water surface and non-turbulent atmosphere. Perhaps the most intuitive description is provided by Augstein et al. (1974) as "that part of the atmosphere where physical processes induced at the sea surface are detectable". Although the exact definition of the MABL, or one of its synonyms, varies per author, the general description consistently refers to a layer between the ocean surface and the free atmosphere.

The MABL is often subdivided into several atmospheric layers. For this study the most important of these layers are the surface layer and the convective/mixed layer. Within the surface layer there are constant turbulent fluxes, regardless of whether the overlying layer is turbulent or stable (Stull, 1988). The surface layer occupies approximately the lowest 10% of the MABL, almost touching the water surface were it not for a thin layer separating the two in which molecular transport exceeds turbulent transport (Stull, 1988). During turbulent convection the surface layer is capped by the mixed layer. The height of the latter is denoted by Z_i, which frequently appears as an important parameter in equations. Different definitions of Z_i are provided by different authors (or sometimes even one and the same author); Deardorff (1974); Young (1987); Stull (1988) define Z_i as the top/depth of the well-mixed layer within the MABL, Kaimal et al. (1976); Panofsky et al. (1977); Zecchetto et al. (1998) describe it as the height of the lowest inversion, Cheynet et al. (2018) as the inversion height and Young (1988); Sikora et al. (1995, 1997) as the convective boundary layer depth. The above definitions all refer to the same height, namely one below which a well mixed, convective layer exists which is capped by an inversion. The capping inversion is visible in atmospheric profiles as it coincides with relatively strong vertical gradients of temperature and humidity. Due to the turbulent mixing within the Convective Boundary Layer (CBL), its vertical gradients of potential temperature and humidity are small (Malkus, 1958; Augstein et al., 1974; Kaimal et al., 1976; Stull, 1988). For the sake of consistency, this study will refer to the layer below Z_i as the CBL.

The dominant convective processes within an unstable MABL are structured as microscale two-dimensional rolls and three-dimensional cells (Sikora and Ufermann, 2004). Examples of the latter and the former are shown in Figure 2.2 and Figure 2.4 respectively. These convective modes are not mutually exclusive. During a transition from cells to rolls, or vice versa, the characteristics of both modes can be observed (e.g. Figure 14.5 in Sikora and Ufermann, 2004). Results shown in Mourad (1996) appear to contain signals of cells neatly aligned within developed rolls and Zecchetto and De Biasio (2002) performed a statistical analysis of cells located in rolls using wavelet transformations.

2.1.1 Three-dimensional cells

A typical ocean is slightly warmer than the overlying atmosphere (Smith et al., 1996). Such temperature differences introduce turbulent convective transport (Stull, 1988; Zecchetto et al., 1998). The resulting atmospheric convection is structured as the aforementioned rolls or cells (e.g. Wackerman et al., 1996; Zecchetto et al., 1998; Young, 2000; Sikora and Ufermann, 2004). Three-dimensional cells occur frequently under low wind-speed conditions with large temperature differences between ocean and air (Dorman and

Mollo-Christensen, 1973; Woodcock, 1975; Young et al., 2000). The horizontal scale of microscale three-dimensional cells is in the order of hundreds of metres to low kilometres (Sikora et al., 1999; Young et al., 2002). Kaimal et al. (1976) found the dominant wavelength of horizontal velocity within three-dimensional cells to be a function of Z_i, namely $1.5Z_i$. Likewise, Young (1988) found a ratio of 1.5 from a separate measurement campaign. Sikora et al. (1995) shows that the expected downdraft pattern caused by three-dimensional cells approximately follows the predicted ratio and that these patterns are visible in radar imagery. The ratio of 1.5 is not carved in stone, Sikora et al. (1995) found a ratio of 1.98 ± 0.5 whereas Caughey and Palmer (1979) observes a lesser ratio. Based on the findings of previous research an aspect ratio of 1.5 can be used as a rule of thumb (Sikora et al., 1997). The aspect ratio does not hold for weakly capped inversion layers or mesoscale cells. Convection within the cells is composed of localised up- and downdrafts (Sikora and Ufermann, 2004). In Figure 2.1 a two-dimensional cross section of a three-dimensional convective cell is shown.

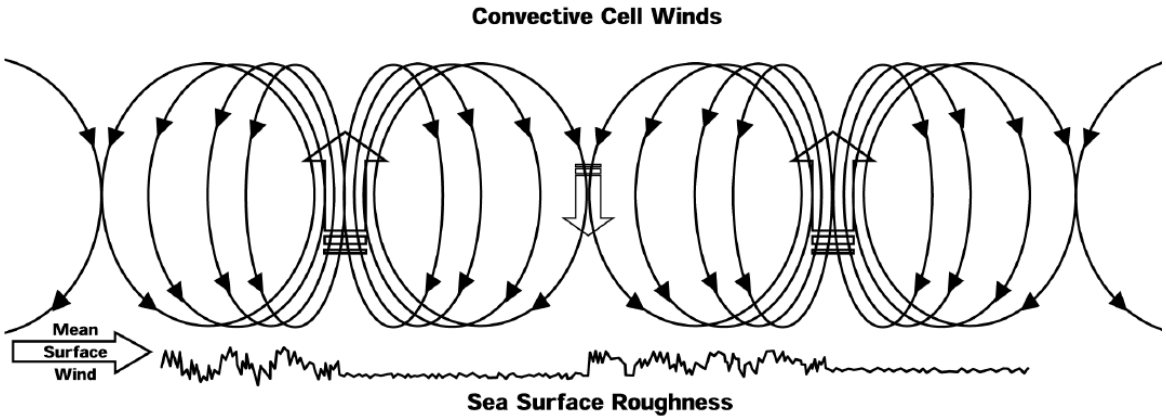

Figure 2.1: Cross section of a three-dimensional cell (Sikora and Ufermann, 2004).

At the locations of downdraft the turbulent air spreads radially and perturbs the water surface. The downdraft wind decreases the magnitude of surface perturbation directed opposite the mean wind direction and amplifies the perturbation in the along-wind direction (Sikora et al., 1995; Sikora and Ufermann, 2004). In summary, surface signatures of three-dimensional cells consists of cell-like structures, also referred to as mottling (Sikora and Ufermann, 2004; Sikora et al., 1997) or cat paws (Dorman and Mollo-Christensen, 1973; Stull, 1988; Sikora et al., 2006), with scales in the order of several hundreds of metres (Stull, 1988) and the greatest variation in perturbation in the along-wind direction (Zecchetto et al., 1998). Concerning the latter point, Sikora et al. (2006) notes that, depending on the specific atmospheric conditions, the approximate orientation of three-dimensional cells can be significantly misaligned with that of the mean wind field.

2.1.2 Two-dimensional rolls

Two-dimensional rolls are created in the presence of thermal differences between layers (similar to three-dimensional cells) and sufficient wind shear at the air-sea interface (Etling and Brown, 1993; Sikora and Ufermann, 2004). Etling and Brown (1993) notes that two-dimensional rolls can also, but less frequently, be caused by inflection point instability during neutral atmospheric stratification. Similar to three-dimensional cells, the downdraft of two-dimensional rolls perturbs the water surface resulting in characteristic pat-

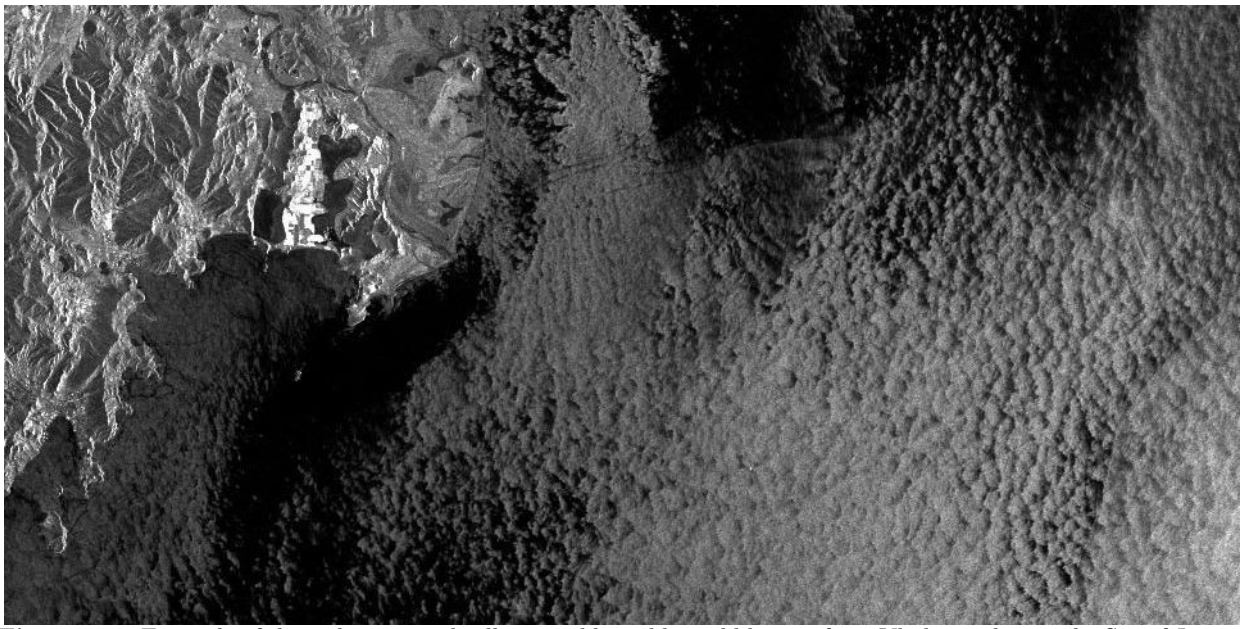

Figure 2.2: Example of three-dimensional cells caused by cold wind blowing from Vladivostok over the Sea of Japan, approximate cell size: $\mathcal{O}$(km), Orbit: 20455, Frame: 2763, Satellite: ERS-2, Date: 20-03-1999 (ESA, 2021).

terns (Sikora and Ufermann, 2004; Wackerman et al., 1996; Etling and Brown, 1993). Contrary to three-dimensional cells, the greatest variation in surface perturbation occurs in the cross-wind direction. The exact orientation of the two-dimensional structures depends not only on the surface wind but also on the geostrophic wind above the roll structures, see Figure 2.3. Faller (1964) notes a 13° bias to the right of the mean surface-wind direction, Lemone (1973) notes an alignment of -5° to 20° to the left of the geostrophic wind and Wackerman et al. (1996) notes possible bias ranges between 13° and 75° to the right of the mean surface-wind direction, the majority of which within 13° and 30°. In a recent study of roll vortices observed with Sentinel-1 WV mode, the orientation deviated from the surface wind with an angle of -1.77° ± 25.18° with no bias to either side of the wind direction (Wang et al., 2019a). The author notes more research is ongoing into this unexpected finding. The spread in wind orientation with respect to roll orientation will complicate wind-direction estimation.

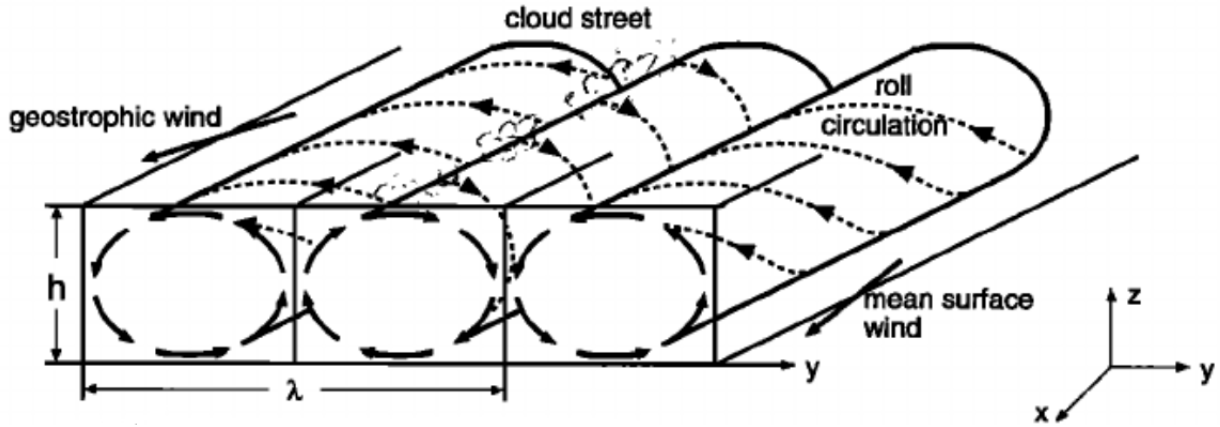

Figure 2.3: Cross section of two-dimensional rolls, (Alpers and Brümmer, 1994).

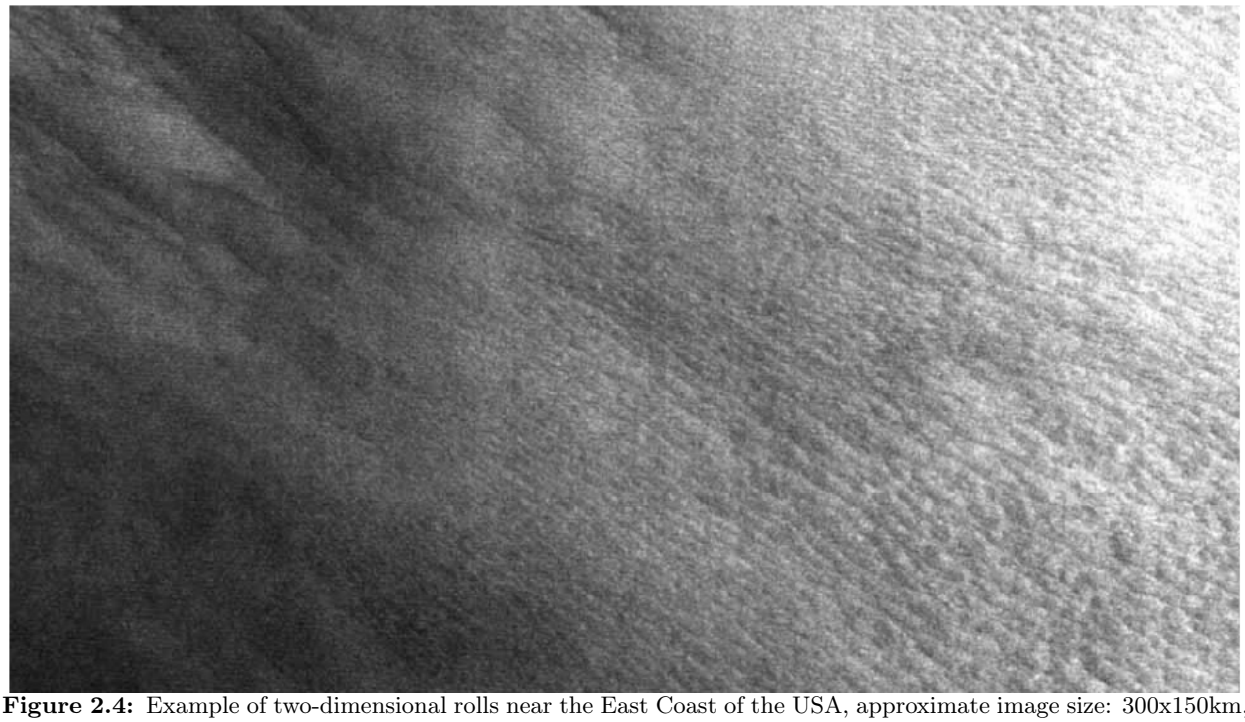

Figure 2.4: Example of two-dimensional rolls near the East Coast of the USA, approximate image size: 300x150km, Satellite: RADARSAT-1, Date: 06-03-1997 (Sikora and Ufermann, 2004).

Downdrafts occur at spatial distances double that of the roll diameter as two counter rotating rolls are required to form one wavelength λ, see Figure 2.3. The scale of λ is in the $\mathcal{O}$(km) order (Sikora and Ufermann, 2004). Optical imagery often shows cloud streets at the location of updrafts (Etling and Brown, 1993; Sikora and Ufermann, 2004). An optical and radar analysis of the spatial frequency should thus yield similar results despite observing roll imprints on different media; radars observe the downdrafts patterns on the water surface whereas optical sensors observe cloud streaks in the updrafts. More interesting for the purpose of MABL characterisation is that, when confined to the MABL due to a strong inversion, the distance between downdrafts (λ in Figure 2.3) can be used as proxy for Z_i. The aspect ratio λ:Z_i is frequently between 2 to 6, although values higher than 10 have also been observed (Lemone, 1973; Brown, 1980; Etling and Brown, 1993; Wackerman et al., 1996; Young et al., 2002; Wang et al., 2019a). The vertical flux caused by two-dimensional rolls is substantial. According to Etling and Brown (1993), modelling exchanges within the MABL, either for climate or meteorology, without considering the flux induced by two-dimensional rolls is "inappropriate".

2.1.3 Atmospheric turbulence

The atmosphere contains various scales of turbulence. Two-dimensional rolls and three-dimensional cells only occupy a portion of the total turbulence spectrum. Three commonly distinguished scales of atmospheric phenomena are the microscale, mesoscale and synoptic scale (Fiedler and Panofsky, 1970). Microscale phenomena are driven by vertical temperature and wind gradients (Fiedler and Panofsky, 1970) such as those observed during MABL convection. In the spatial domain they occupy wavelengths between 100 m to several kilometres, although usually smaller than $\mathcal{O}$(3 km) (Stull, 1988). Mesoscale phenomena are driven

by horizontal temperature and wind gradients which occupy spatial scales between approximately 2 km and several hundred kilometres (Fiedler and Panofsky, 1970; Nastrom et al., 1984; Lilly, 1989) with synoptic scale phenomena being greater still (Fiedler and Panofsky, 1970). One can distinguish between scales of turbulence by plotting the atmospheric horizontal velocity energy spectrum. The calculation of this spectrum is described in subsection 3.3. The mesoscale follows a -3 and -5/3 power law between approximate horizontal scales 600 - 3000 km and 1 - 200 km respectively (Nastrom et al., 1984; Lilly, 1989). The local atmospheric setting affects the kilometre scale spectral shape. In the presence of sufficient microscale forcing—read turbulent convection in the form of two-dimensional rolls or three-dimensional cells—a +1 power law leads up to a microscale peak located at the hectometre/kilometre scale, followed by yet another -5/3 power law at shorter wavelengths (Young, 2000). Depending on the surface-layer interactions of turbulent eddies with the mean flow, a -1 power law can be found instead of a spectral peak (e.g Katul and Chu, 1998).

The largest scale of horizontal three-dimensional cells was found to be approximately $1.5Z_i$ by Kaimal et al. (1976). Thus, in the presence of three-dimensional cells one expects to find an energy peak in the horizontal velocity spectrum around spatial wavelengths of $1.5Z_i$ (the same holds for two-dimensional rolls although the Z_i multiplier may differ). This is called the production range. The turbulent energy produced at these scales transfers into smaller scales, i.e. large convective eddies dissipate energy and become smaller over time. The energy dissipation results in the well known -5/3 power law in the inertial subrange (Stull, 1988; Lilly, 1989). The entire -5/3 slope past the microscale peak (or plateau) will be referred to as the inertial subrange. If the observed horizontal-velocity energy spectra contain a peak or plateau in the microscale range followed by an inertial subrange, it indicates the presence of microscale convection. However, the spectrum amplitude, and thus the wind-field variance, can still be incorrect whilst simultaneously showing a perfect power law.

2.1.4 Similarity theory

It is complex to model all the underlying physics and interactions occurring within the lower turbulent atmosphere. For some time it has been known that under similar conditions, similar atmospheric behaviour can be observed. Hence the *similar* in similarity theory. By grouping parameters which are likely to influence atmospheric conditions, one can derive and fit empirical functions (Stull, 1988; Smith et al., 1996). Successful examples of such an approach are that of the Monin-Obukhov Similarity Theory (MOST) (Monin and Obukhov, 1954) for the surface layer (hence also referred to as surface-layer similarity) and mixed-layer similarity (e.g. Deardorff, 1970; Kaimal et al., 1972) for the mixed layer. Both these similarity theories are used to characterise the MABL and thus they shall be introduced further below.

2.1.4.1 Monin-Obukhov Similarity Theory MOST provides approximate universal surface-layer profile functions (Wilson, 2008). These functions depend on but a few variables, which, by measuring at a known height, can be used to extrapolate atmospheric behaviour within the entire surface layer. Horizontally homogeneity and quasi-stationary conditions are preconditions for the theory to be applicable (Khanna and Brasseur, 1997). The main scaling parameter in MOST is Obukhov length L. It is related to atmospheric stability and can be interpreted as being proportional to the height above the surface beyond which buoyant production of turbulence dominates over shear production (Stull, 1988). Obukhov length is calculated

following

$$L = -\frac{\overline{T}_v u_*^3}{\kappa g \overline{w'T'_v}}. \tag{2.1}$$

The numerator contains information on the horizontal wind shear whereas the denominator concerns the vertical transport of energy (temperature). The virtual potential temperature T_v is equal to the temperature of a hypothetical dry air parcel at the same pressure and with equal density as a moist parcel for which altitude pressure variations have been removed (Stull, 1988). u_* is the horizontal friction velocity and κ the von Kármán constant. Both are used to connect wind speeds to surface stress. Typically u_* is an order of magnitude smaller than the wind speed at 10 m height. According to Table 1 in Högström (1996) and Table 2 in Foken (2006) $\kappa \approx 0.40$. Gravitational acceleration is denoted by g and vertical wind velocity by w. Over-bars and apostrophes indicate mean (e.g. temporal mean) and fluctuations respectively.

Three-dimensional cells and two-dimensional rolls are created by turbulent heat transport from the water surface into the lower atmosphere. Vice versa is also possible but less prominent (Smith et al., 1996). Thus the mean energy flux, $\overline{w'T'_v}$, is positive and directed upwards. The corresponding Obukhov length is negative which means the atmospheric conditions can be described as an unstable regime (Monin and Obukhov, 1954). This fact will become important later on for the selection of equations. Although MOST has been used for over 50 years, it is not without its limitations. Smedman et al. (2007) argues that for large negative values of L ($-L > 150$ m) near the surface ($z \approx 10$ m) MOST might be incapable of accurately predicting atmospheric behaviour.

2.1.4.2 Mixed-Layer Similarity Mixed-layer similarity is applicable during free convective conditions in the mixed layer (Stull, 1988), hence the name. Free convective conditions includes convection induced by cold air blowing over a warm water surface (Stull, 1988), such as for two-dimensional rolls and three-dimensional cells. The primary scaling parameter in mixed-layer similarity is the convective velocity scale w_* which, according to Deardorff (1970) and Stull (1988), can be calculated following

$$w_* = \left[\frac{g}{T_v} Z_i \overline{w'T'_v}\right]^{1/3} \tag{2.2}$$

By combining a calculated value of w_* with equations presented in subsubsection 3.5.3, mixed-layer similarity can be used to derive L and subsequent atmospheric parameters. It is important to consider the validity of mixed-layer similarity for the expected scenarios. The estimated wind fields are located at 10 m height. Even for conservative boundary layer heights this would likely result in surface-layer—rather than mixed-layer—similarity governed regimes (e.g. Figure 2 in Khanna and Brasseur, 1997). Young (2000) justifies the use of mixed-layer similarity in the surface layer as the conditions encountered under strongly unstable boundary layers in the surface layer should be representative of those in the mixed layer. This introduces a degree of uncertainty into the analysis depending on how representative the surface layer behaviour is with respect to the mixed layer. In a bid to account for such uncertainties, this study will use dimensionless energy dissipation rate ψ values more in line with those encountered in the surface layer, see subsubsection 3.5.3. Whether this alteration is sufficient to justify use of mixed-layer similarity within the surface layer for less unstable atmospheric settings remains open for debate.

2.2 Water surface

2.2.1 MABL signature

The MABL is observed indirectly by identifying its signatures on other physical media. Both the two-dimensional rolls and three-dimensional cells discussed in subsection 2.1 perturb the water surface following unique patterns. The large-scale perturbations of these patterns (hundreds of metres to kilometres) result in a local increase/decrease of water-surface short waves with wavelengths ranging between a few to tens of centimetres (Holt, 2005). Constructive interference of the radar signal can occur when these short waves are equally spaced and of approximately equal size with respect to the radar signal (Holt, 2005). This is known as Bragg scattering and results in increased radio wave backscatter (Vachon et al., 2004; Holt, 2005; Robinson, 2010). Bragg scattering is dominant for VV polarisation between incidence angles of 20° to 70° (Rizaev et al., 2021) for wind speeds greater than 2 ms^{-1} (Holt, 2005). Since these conditions are frequently met for the Sentinel-1 (S1) observed scenes, the side-looking radar onboard S1 is predominantly sensitive to Bragg scattering and, thus, surface roughness at scales comparable to its emitted radio wavelength (Rizaev et al., 2021). The orientation of the surface waves also affects backscatter. That part of the wave oriented towards the radar returns stronger backscatter than that part facing away (Robinson, 2010). This is known as tilt modulation. MABL signatures can be identified as structures within the SAR observation where increased backscatter follows the expected water surface perturbation structures, such as in Figure 2.1 and Figure 2.3. Both Bragg and tilt modulation are weakest for waves propagating in the azimuth direction (Robinson, 2010).

2.2.2 Swell

The water surface contains manifestations of more processes than the two MABL convection processes described above. Oceanic processes (e.g. oceanic eddies, upwelling and bathymetry) and atmospheric processes (e.g. gravity waves, coastal winds and rain events) can perturb the water surface, leaving signatures of their own (Young et al., 2000). The presence of swell is a frequently cited error source in sea-state analyses (e.g. Smith et al., 1996; Sikora et al., 1999; Drennan et al., 1999; Young et al., 2000). Swell originates from strong wind-forcing events such as storms. The low-frequency waves created during these events gradually dissipate their energy and are capable of travelling thousands of kilometres from their original source location (Ardhuin et al., 2009). Swell spatial wavelengths are in the order of hundreds of metres (e.g. Vachon et al., 2004; Toffoli and Bitner-Gregersen, 2017), which can overlap with that of two-dimensional rolls and three-dimensional cells. Swell-induced perturbations of the water surface result in local increases/decreases of radar backscatter. This can negatively affect the wind-speed and surface-stress estimation as it is assumed that the water-surface perturbations are wind induced (Sikora et al., 1999; Robinson and Fangohr, 2010). Errors introduced by swell can be strong enough to prevent any further analysis (Drennan et al., 1999; Young et al., 2000). Furthermore, swell waves are not bound to propagate in the mean wind-speed direction (Smith et al., 1996). The total stress vector caused by both swell and wind can thus be orientated erroneously with respect to the true wind direction. The aforementioned other atmospheric and oceanic processes can also introduce errors but their signal is more easily separated or has a lesser impact than that of swell.

2.3 Sentinel-1

The Sentinel-1 constellation contains two C-SAR carrying satellite platforms with a revisit time of at most 6 days (ESA, 2021a). The C-SAR instrument sends out C-band microwave pulses with a centre frequency of 5.405 GHz (approximately 5.5 cm wavelength) (ESA, 2021b). At these wavelengths the effects of weather on backscatter can, under most circumstances, be ignored, allowing the instrument to make measurements under all weather conditions. The returned signal intensity, also known as backscatter, is used to infer properties of the observed medium. The C-SAR instruments can operate at various modes with different polarisations. This study will use the Interferometric Wide swath mode (IW) with a ground range resolution of 5 by 20 m (prior to resampling). In principal any of the other modes could be used instead. All analysed images were obtained with the C-SAR instrument transmitting and receiving in the vertical (V) polarisation. This is abbreviated by VV. Alternative polarisation settings are transmitting and receiving in horizontal (H) polarisation, abbreviated by HH, or cross polarisation such as VH or HV. VV polarisation performs better for meteorological investigations such as those performed in this study (Ufermann and Romeiser, 1999).

The achievable resolution of a radar is governed by its antenna length. Practical considerations limit the maximum antenna length and thus the achievable resolution. By rapidly changing the orientation of the radar antenna one can illuminate and receive echos from the same target at successive locations in the orbit, see Figure 2.5. Through matching these echos one synthetically increases the antenna's aperture, a.k.a. effective antenna length, which in turn increases the achievable resolution (Chan and Koo, 2008). Hence the acronym SAR, which stands for Synthetic Aperture Radar.

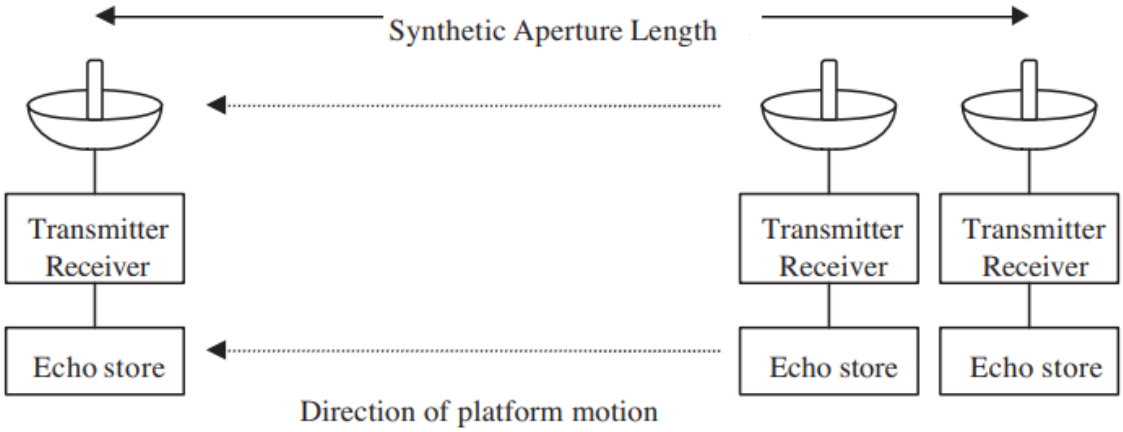

Figure 2.5: SAR principle (Chan and Koo, 2008).

During echo matching it is assumed that the observed targets had a negligible velocity component with respect to their surroundings (Brüning et al., 1990). Targets with a velocity component will be shifted in azimuth direction due to the manner in which SAR data is processed (Holt, 2005). This can result in interesting artefacts such as trains appearing off their tracks. Even within a single pixel, the ocean surface is in constant motion with waves travelling in different directions with variable velocities and accelerations. Resulting artefacts include azimuthal cut-off, smearing and velocity bunching (e.g. Brüning et al., 1990; Kerbaol et al., 1998; Rizaev et al., 2021). These can degrade the ideal image resolution such that the real

resolution is an order of magnitude less, e.g. 20 m resolution to 200 m resolution. The degree of degradation is dependent on the distribution of surface-wave velocities, i.e. the sea state, and the radar platform range-to-velocity ratio (Brüning et al., 1990; Vachon et al., 1994; Rizaev et al., 2021). Zecchetto et al. (1998) was only able to obtain a 4.4 by 4.4 m ground-range resolution using an airborne—rather than spaceborne—radar over a relatively calm water surface.

2.4 Geophysical Model Functions

Geophysical Model Functions (GMFs) are empirical models used to estimate low-resolution, $\mathcal{O}(10\text{ km})$, wind speeds from backscatter measured by scatterometers or SAR systems. Other variables included in GMFs are wind direction and radar incident angle. In the simplest form such a model for C-band systems can be written as

$$\sigma_0 = \text{CMOD}\left(c, U_n, \phi, \theta\right), \tag{2.3}$$

where c represents several fine-tuned constants (28 for CMOD5.N), U_n the current relative equivalent neutral wind speed at 10 m above sea level, ϕ the angle between scatterometer look direction and wind direction, θ the incidence angle of the scatterometer and σ_0 the Normalised Radar Cross Section (NRCS) which quantifies the reflectivity of the object, i.e. the quantity of radio wave backscatter per surface area (Hersbach, 2008). Current relative equivalent neutral wind speed (throughout this study referred to as wind speed or neutral wind speed) is used because the component of the wind vector moving parallel to the surface current vector does not exert a force. Thus, depending on the magnitude and orientation of surface currents, the estimated wind speeds will be over- or underestimated. This study employs inverse CMOD5.N and CMOD-IFR2 models to calculate wind fields from radar images. Multiple combinations of wind speed and incidence angle can yield the same radar backscatter value (Vachon et al., 2004). To resolve this ambiguity the wind direction must be known prior to the application of the inverse model. The retrieval of the wind direction is described in subsection 3.2.

Although originally not designed for Sentinel-1, CMOD5.N is calibrated for C-band scatterometers, allowing Sentinel-1 to use it. The acronym stands for (the 5th iteration of the) C-band model (Hersbach, 2008). The ".N" refers to equivalent neutral wind speeds. For identical wind speeds, winds occurring under unstable atmospheric conditions cause greater surface roughness than their neutral atmospheric counterparts. As the degree of instability is not known, the CMOD algorithm yields equivalent neutral wind speeds i.e. the neutral wind speed with the same perturbing strength as a wind speed with unknown instability (Hersbach, 2010). As discussed in subsection 2.1, during convective processes the atmosphere is turbulent and non-neutral. Because the received radar signal is a function of surface roughness, and thus surface stress, the computed neutral wind speeds can be inverted to calculate the real surface stress without having to account for a turbulent atmosphere. This is detailed in subsubsection 3.5.1. All other parameters require a correction for the non-neutral atmosphere.

Multiple empirical models exist capable of relating wind speed to σ_0. Young et al. (2000) uses a CMOD4-like algorithm which also gives neutral wind speed. A different CMOD branch entirely is presented by Quilfen et al. (1998) called CMOD-IFR2, after the second iteration of a CMOD product developed by

Institude Français de Recherche (pour l'Exploitation de la Mer). In comparison with CMOD5.N, CMOD-IFR2 yields lower wind speed values with relatively greater wind-speed variance for the study areas, see section 5. CMOD5.N is selected as the main GMF for this study since it has enjoyed a decade of improvements and tweaks over CMOD-IFR2. This choice is supported by results from Geldsetzer et al. (2019) who found (slightly) lower biases and RMSE for CMOD5.N in comparison with CMOD-IFR2 and buoy measurements.

Considering that this study employs GMFs at resolutions two orders of magnitude greater than these GMFs were designed for, $\mathcal{O}(0.1$ km) instead of $\mathcal{O}(10$ km), it is fitting to note relevant limitations. The resolution of any GMF-derived wind field is subjected to the SAR-related limitations mentioned in subsection 2.3. In this study it will be assumed that these limitations do not degrade the resolution over spatial wavelengths for which the power laws discussed in subsubsection 2.1.3 hold. There exist less straightforward constraints which hinder the performance of GMFs beyond the physical limitations associated with SAR observations. No GMFs take into account atmospheric and oceanic effects such as rain bursts, swell, surface slicks or currents. These phenomena will yield erroneous wind-speed values if present in the observed area. By comparing wind fields calculated using HH and VV polarisation one might be able to isolate oceanographic effects since HH polarisation is more sensitive to oceanographic signals (Ufermann and Romeiser, 1999). More important for this study is the omission of sea-state effects in most CMOD algorithms. Quilfen et al. (2004) shows improved performance over existing models CMOD-IFR2 and CMOD4 when (partially) accounting for the local sea state. They note the impact of sea state being greatest for falling and rising wind conditions and or anomalous fetch lengths. According to Hersbach (2010), CMOD5, and thus CMOD5.N, does not explicitly take into account sea-state effects. However, while training the CMOD5 GMF, the Charnock constant a—which is an empirical constant that accounts for sea state—was selected as a function of wind speed and thus indirectly incorporated sea-state effects. Hersbach (2010) goes on to note that a large spread in a exists for a given wind speed, implying that a Charnock constant as a function of wind speed alone is insufficient at capturing sea states. This begs the questions whether or not GMFs such as CMOD5.N are capable of estimating high-resolution wind-speed fields since they are not designed to take into account small-scale variations of the sea state associated with turbulent convection.

Methodology

This study aims to estimate atmospheric parameters from SAR amplitude data. These parameters include wind direction δ, wind field U, wind-field variance σ_u^2, friction velocity u_*, Convective Boundary Layer (CBL) depth Z_i and Obukhov length L. This chapter addresses step-by-step the conversion of Ground Range Detected (GRD) radar data to Normalised Radar Cross Section (NRCS) data using the Sentinel Application Platform (SNAP), the derivation of wind directions from NRCS fields, the extraction of u_* from wind fields (using algorithm 1), the computation of turbulence spectra from wind fields, the estimation of Z_i from turbulence spectra and lastly the application of similarity theories employed in algorithms 2A, 2B and 2C to retrieve L and σ_u. A general overview of the methodology is presented in Figure 3.1. Python scripts for the methodology are provided in subsection A.1.

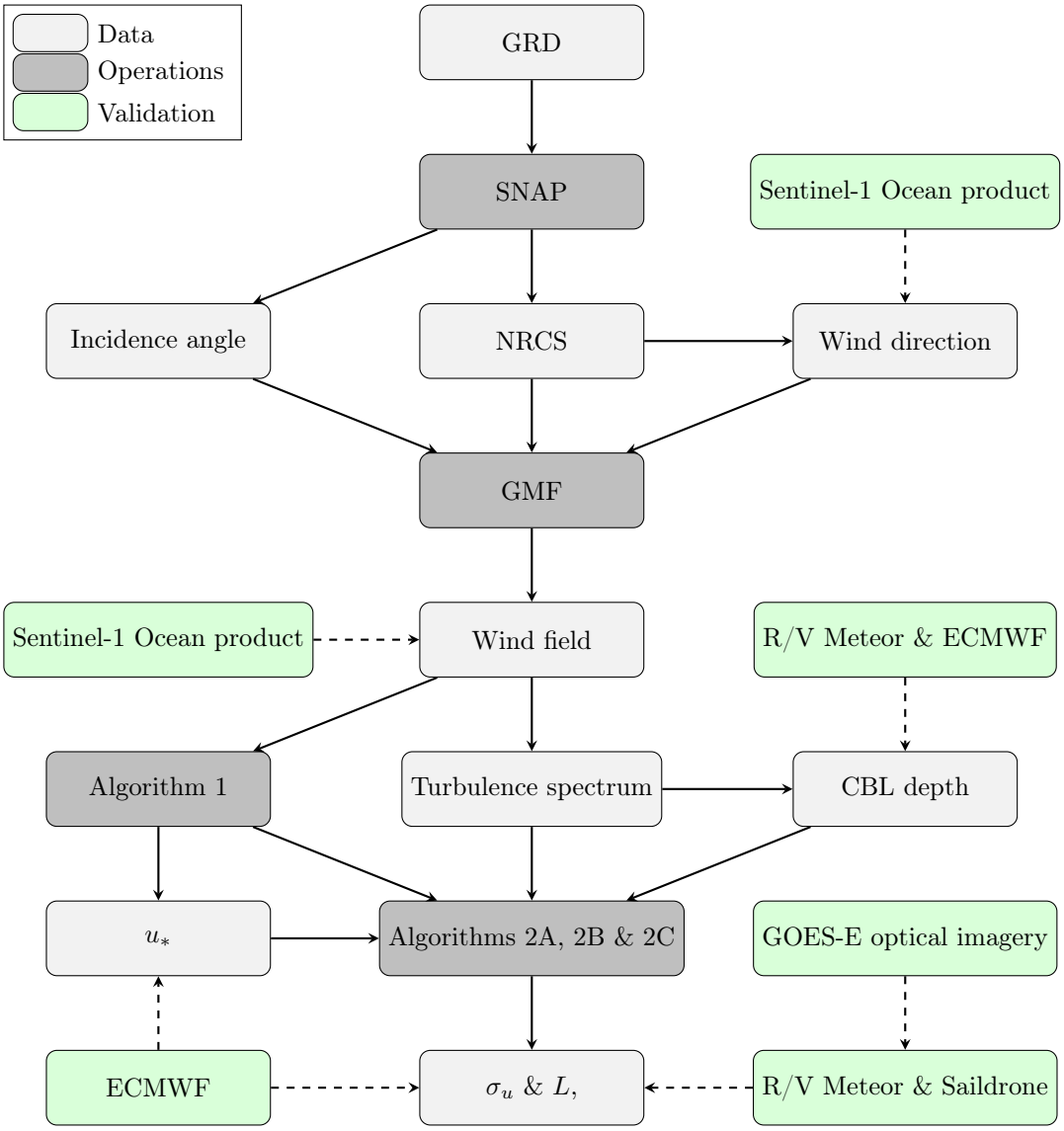

Figure 3.1: Methodology flowchart.

3.1 Normalised Radar Cross Section

Ground Range Detected (GRD) 10 m resolution data downloaded from the Alaskan Satellite Facility is imported into SNAP. Here the data is processed further following the steps outlined by James (2017) and Filipponi (2019). First, if available, the precise orbit of the satellite is updated, improving the positioning accuracy. The Sentinel-1 observation is comprised of three cross-track subswaths (Collecte Localisation Satellites, 2016). The antenna patterns causes a spatially varying noise pattern with sharp discontinuities at the subswath border (Park et al., 2017). Thermal noise removal in SNAP gets rid of this background noise signal. Subsequently the digital number values contained in the GRD file are converted to Normalised Radar Cross Section σ_0 (NRCS). Each pixel in the NRCS image links the observed surface area to a quantity of backscatter. After conversion to NRCS the radar image can be used for quantitative purposes. As an optional step one can apply SNAP multilooking (a low-pass filtering operation) to spatially average pixels. This leads to decreased speckle noise and pixels of desired size. Multilooking was performed to achieve 300 m pixels. This dimension was selected as suitable as it decreased computational load (compared to the standard 10 m pixels) whilst maintaining a high-enough resolution required to observe the convection processes in question. A more elaborate explanation for this resolution is provided in subsubsection 3.3.1.

3.2 Wind direction

The NRCS field is linked to small-scale surface roughness. The surface roughness is closely connected to wind speed and is normally inferred from NRCS using GMFs (see subsection 2.4). The wind direction δ is a required input for the GMF. A frequently used δ estimation method for SAR imagery employs two-dimensional spectral analysis to find the orientation corresponding to the greatest degree of variance (e.g. Gerling, 1986; Wackerman et al., 1996; Zecchetto et al., 1998). This approach relies on the fact that water-surface perturbations tend to be greatest either along- or cross wind, depending on the forcing mechanism. Two-dimensional rolls and three-dimensional cells induce the greatest variation approximately cross- and along wind respectively. Thus, with prior knowledge of the present forcing mechanism, one can estimate δ based on the observed orientation of the greatest variation. The δ estimation performed in this study follows the methods described by Gerling (1986) and Wackerman et al. (1996). The method is adapted to take into account an approximate 90° offset when applied on scenes containing three-dimensional cells (the original method was developed for two-dimensional rolls). When both convective modes are present and interspersed, such as during the transition phase, a 90° ambiguity exists for δ estimates. For such cases one can use validation data to resolve the ambiguity.

First the radar tiles are detrended in range and azimuth to remove the effect of wavelengths longer than those involved in wind-direction estimation as well as to circumvent the effect of variable SAR backscatter as a function of range (Gerling, 1986). Detrending is accomplished by subtracting and subsequently dividing the tile by a low-pass filtered tile. The low-pass filtered tile is created by Gaussian blurring using a kernel size of 10^2 km^2. Similar to Gerling (1986), a two-dimensional Hamming window is applied to the entire detrended tile in order to prevent spectral leakage. Next a two-dimensional Fourier transform is calculated for the detrended windowed tile, yielding its two-dimensional spectrum. Gaussian smoothing is applied to the two-dimensional spectrum to reduce its speckle noise. The location of spectral peaks within this smoothed spectrum give the orientation of greatest variance. Combined with the known satellite heading,

the orientation of greatest variance is converted to a heading with respect to north, i.e. the wind direction δ. Peaks at wavelengths < 400 m are ignored as these are unlikely to be caused by MABL convection. One can also set an upper limit to prevent to the inclusion of spectral peaks originating from mesoscale convection. Rather than relying on peaks only, one can fit a two-dimensional Gaussian function through the wavelengths of interest, similar to Wackerman et al. (1996). In this manner more spectral information is incorporated into the estimation than peaks only. However, for small homogeneous areas this is not expected to improve results.

The method described above contains several error sources of which the most prominent will be mentioned here. First there is the 180° ambiguity introduced by the two-dimensional Fourier spectrum (Robinson, 2010). Zecchetto et al. (1998) proposes a method to resolve this ambiguity by determining the lee side of the wave in the along-wind radar amplitude data. However, this approach was only possible as a result of a favourable measuring setup. Other studies have used the direction of island wind shadows to resolve the ambiguity (e.g. Koch, 2004). Naturally this is only possible if islands or other large wind obstructing structures are present in the observed area. This study will use co-located δ estimates provided by the Sentinel-1 Ocean (S1 OCN) product in order to resolve the ambiguity. For further details on S1 OCN see subsubsection 4.2.4. Then there is the difference between δ estimation for cells versus rolls. Mistaking cells for rolls will lead to approximately 90° error in δ estimation since their respective axes of maximum variability are approximately perpendicular to each other. This can be especially tricky when both modes are present and interspersed such as during a transitional phase. Next is the bias between the orientation of greatest variance and the true wind direction. For two-dimensional rolls this bias follows a distribution (Wackerman et al., 1996; Wang et al., 2019a) meaning δ can only be given in a stochastic sense. For three-dimensional cells the estimated δ's are expected to be within a few degrees of the direction of greatest variation (Sikora et al., 2006). In this study it will be assumed that the δ's for cells are aligned with the true wind direction and that the δ's for rolls are orientated 20° to the left (right) of the axes of greatest variance on the northern (southern) hemisphere. The justification for this value relates to it falling within the range of angle deviations provided in literature (e.g. Wackerman et al., 1996; Wang et al., 2019a). In Figure 3.2a the estimated wind directions are shown for an example scene without compensation for the expected offset. Each arrow represents a wind direction estimated over a 25^2 km^2 area. In Figure 3.2b a 20° compensation is applied which compares more favourably to the S1 OCN wind-direction field in Figure 3.2c.

The radar look angle with respect to the wind direction directly affects the ability to detect SAR wind features and in turn wind direction. Thompson et al. (1983) and Robinson (2010) note that waves travelling perpendicular to the radar look angle yield the least prominent signatures. Thus, structures propagating parallel to the azimuth direction are significantly harder to detect. Phenomena unrelated to convection can also compromise δ estimation if they sufficiently perturb the water-surface stress vector. A catalogue concerning common compromising culprits could certainly contain currents, cloudbursts, coastal circumstances (et) cetera.

3.3 Spectrum calculation

The wind direction, incidence angle and NRCS field are fed into a GMF, which yields a wind field. A one-dimensional turbulence spectrum is computed from this wind field. First the wind field is rotated cross-

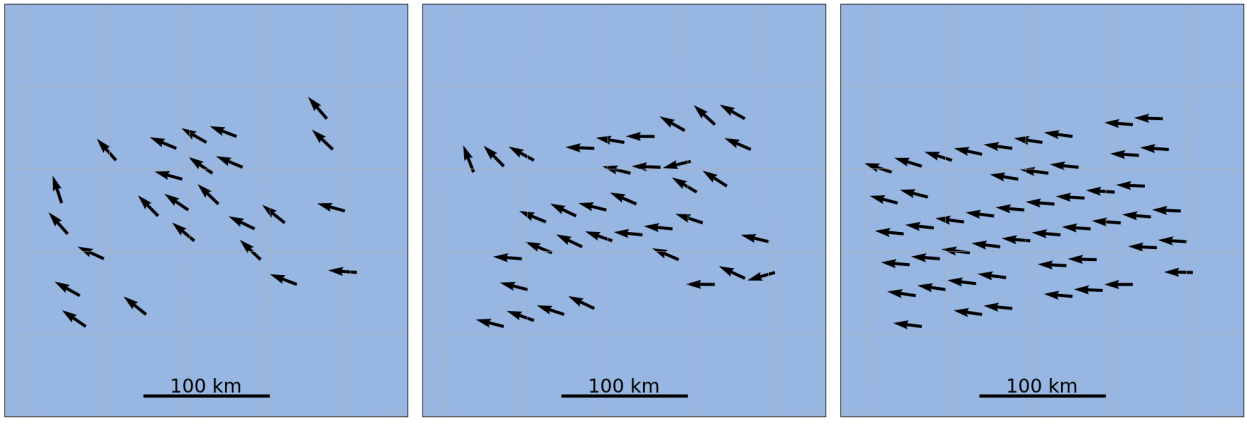

(a) Accounting for no offset **(b)** Accounting for 20° offset **(c)** S1 OCN wind field

Figure 3.2: Effect of wind direction offset for rolls w.r.t. S1 OCN forecast. An increased quantity of estimates pass the quality threshold from left to right, hence the extra arrows. Scene January 27th B, see Table 5.

and along the axis of greatest variability, i.e. the orientation of the spectral peaks found in subsection 3.2. Rotation results in rows of unequal size in the direction parallel/perpendicular to the desired orientation. Clipping ensures that the largest square unaffected by rotation artefacts is extracted (see Figure 3.3). Unless rotation is exactly an integer multiple of 90°, the rotated wind field will be smaller than the original wind field.

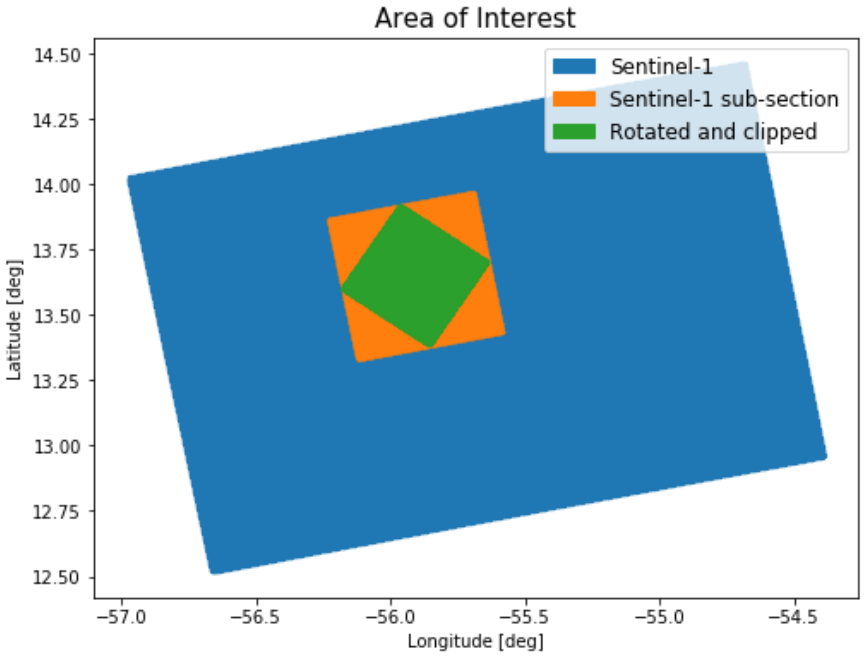

Figure 3.3: Example extent after sub-setting, rotating by 45° and clipping.

Next a normalised Hanning window and a Discrete Fourier Transform (DFT) are performed on a per-row basis. The DFT output is divided by the number of samples in each row N, giving $F(\xi)$, such that

$$F\left(\xi\right) = \frac{\mathrm{DFT}\left(\mathrm{row}\left(i\right)\right)}{N}, \tag{3.1}$$

here ξ refers to spatial frequency and i specifies the row index. Depending on the rotation this will result in either a cross- or along-wind $F(\xi)$. Following Stull (1988), the single-sided energy spectrum $E(\xi)$ is calculated from the positive frequencies of $F(\xi)$ using

$$E\left(\xi\right) = \begin{cases} E\left(\xi_{1\rightarrow nq}\right) = 2|F\left(\xi_{1\rightarrow nq}\right)|^2, & \text{for } N = \text{odd} \\ E\left(\xi_{1\rightarrow nq-1}\right) = 2|F\left(\xi_{1\rightarrow nq-1}\right)|^2, & \text{for } N = \text{even} \\ E\left(\xi_{nq}\right) = |F\left(\xi_{nq}\right)|^2, & \text{for } N = \text{even} \end{cases} \tag{3.2}$$

here ξ_1 is the fundamental frequency and ξ_{nq} is the Nyquist frequency. The DC component ξ_0 is discarded. The sum of all $E(\xi)$ components is identical to the wind-field variance, e.g.

$$\sigma_u^2 = \sum E\left(\xi_{1\rightarrow nq}\right). \tag{3.3}$$

Subsequently the power spectral density is calculated following

$$S\left(\xi\right) = \frac{E\left(\xi\right)}{\Delta\xi}, \tag{3.4}$$

where $\Delta\xi$ is the frequency bin width, which can be calculated by

$$\Delta\xi = \frac{\xi_s}{N_{\mathrm{DFT}}}, \tag{3.5}$$

where ξ_s is the sample frequency, i.e. pixel size, and N_{DFT} is the number bins in the DFT, i.e. the number of samples N in $F(\xi)$. The units of $S(\xi)$ are equal to the input units squared over spatial frequency. Since the input wind field has units of ms^{-1}, the units of $S(\xi)$ are $\mathrm{m}^3\mathrm{s}^{-2}$ ($\mathrm{m}^2\mathrm{s}^{-2}\mathrm{m}^1$) . However, further calculations require temporal spectra $S(n)$ with units of $\mathrm{m}^2\mathrm{s}^{-1}$ rather than spatial spectra. The conversion from spatial $S(\xi)$ to temporal $S(n)$ invokes Taylor's hypothesis. This hypothesis assumes that the studied air parcel is "frozen" whilst propagating through space (Stull, 1988). Invoking Taylor's hypothesis, temporal frequency n is calculated from spatial frequency ξ as

$$n = \xi\overline{U}, \tag{3.6}$$

where $\overline{U}$ indicates mean wind speed. Following equation 1 from Kaimal et al. (1972), this leads to the calculation of $S(n)$ as

$$S\left(n\right) = \frac{1}{\overline{U}} S\left(\xi\right). \tag{3.7}$$

Thus, spatial frequency spectra are divided by the mean wind speed to arrive at the temporal frequency spectra. The latter is used for further calculations and will be referred to as the PSD. Examples of PSDs calculated for a radar scene are presented in Figure A.11.

The presence of anomalous strong reflectors (such as ships) within the study area can skew calculated PSDs. For this reason anomalous PSDs are removed from further analysis. The filter works as follows: first the PSDs are calculated as described above, next the PSDs are scaled with their respective temporal frequency to arrive at $n \cdot S(n)$. The maximum amplitude values of these scaled PSDs are retrieved (which should be the microscale peak) and lastly each scaled PSD whose maximum exceeds twice the median of maxima is excluded. The threshold at twice the maximum is manually set, but it can be varied or optimised.

3.3.1 Spectral filtering

Water-surface stress is the key parameter in estimating MABL properties. The methodology proposed by Young et al. (2000) relates water-surface stress caused by MABL convection to a specific MABL state. The variance of this stress field is used for computations. However, stress at the air-sea interface can be caused by both oceanographic and other atmospheric phenomena. When analysing this variance one should only consider that part induced by MABL turbulence. Significant amounts of variance may be present in the mesoscale part of the spectrum. Attributing this variance to microscale turbulence will contaminate results. Applying a simple band-pass filter is unsuitable because the horizontal scale of MABL turbulence can overlap with other sources of variance (Young et al., 2000). Instead Young et al. (2000) uses spectral models of atmospheric turbulence, such as those by Lilly (1989); Young (2000), to filter the SAR-derived turbulence spectra. This filtering entails the fitting of known spectral models to uncontaminated portions of MABL turbulence spectra, followed by extrapolation of these models into the spectral regions contaminated by unwanted variance. Naturally this requires that sufficiently large uncontaminated sections of the spectra can be attributed to MABL convection and, in turn, used as extrapolation starting points. Work by Mourad et al. (2000) implies that a similar effect can be achieved by spatial averaging to a sufficiently large resolution. The desired resolution for their dataset was found to be approximately 300 m. Young et al. (2000) employs the spectral filtering method whereas the studies by Sikora et al. (1999, 2000); Sikora and Thompson (2002) apply spatial averaging to the resolution found in Mourad et al. (2000). Alternatively one can avoid filtering all together by only using that part of the spectrum known to be unaffected by other sources. This is implicitly assumed in the inertial subrange characterisation approach of subsubsection 3.5.3 which is the second method employed by Young et al. (2000).

This study uses 300 m resolution radar imagery though not for the reason described by Mourad et al. (2000). At 300 m resolution the imaging artefacts discussed in subsection 2.3 are avoided and the two-dimensional spectra showed no unwanted signals such as from swell or speckle, see Figure 3.4a. A two-dimensional spectrum obtained using 50 m pixels displays unwanted signals at high wavenumbers, see Figure 3.4b. Using a 300 m resolution, all one-dimensional spectra obtained for the Barbados study cases displayed approximate -5/3 power law slopes following a plateau or peak. For higher resolutions the expected power laws were compromised. This could be due to spectral projection or leakage of power onto the relevant wavelengths of the -5/3 slope. In particular for non-homogeneous study areas with multiple local spectral peaks one can observe spectral power at higher frequencies projecting itself onto the more relevant lower frequencies.

As an alternative to SNAP multilooking one could use a higher resolution and apply a custom low-pass filter, see Figure 3.4c. Regardless of whether one applies SNAP multilooking or custom low-pass filtering, the resolution should be selected as that which removes unwanted signals whilst simultaneously allowing to resolve the spatial frequencies related to convection. For instance, for shallow mixed layers ($Z_i \leq 400$ m), a higher resolution than 300 m is required to resolve the spectrum at the convective wavelengths.

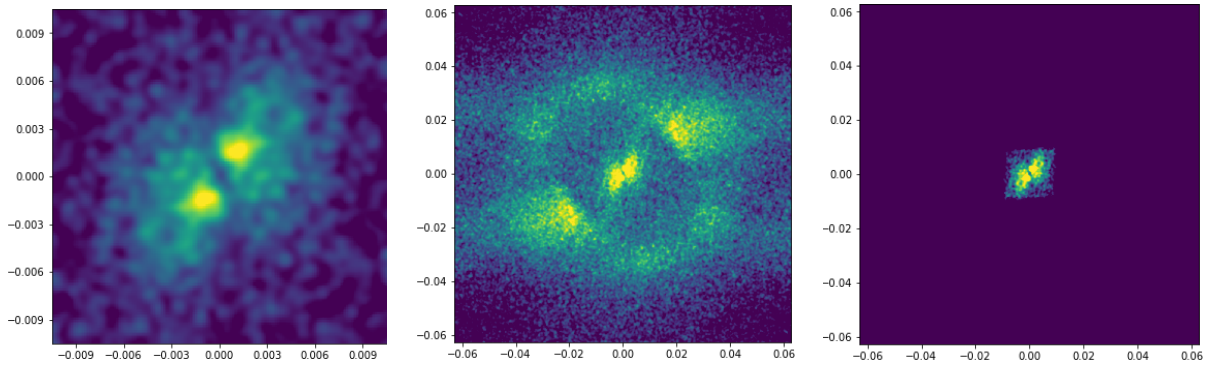

(a) 300 m resolution (Multilooked) **(b)** 50 m resolution **(c)** 50 m resolution, filtered at 600 m

Figure 3.4: Examples of Gaussian smoothed two-dimensional spectra for a subsection of scene January 27th B, see Table 5. Arbitrary amplitude from low (blue) to high (yellow), axes in wavenumber k [rad m^{-1}].

3.4 Convective Boundary Layer depth

Both convective processes discussed in subsection 2.1 provide indirect information on the CBL depth. The large spread in observed aspect ratios of two-dimensional rolls complicates their use in consistent CBL depth estimation. Three-dimensional cells have a more constant aspect ratio near 1.5, as shown by Kaimal et al. (1976) and Sikora et al. (1995). Sikora et al. (1997) utilises this ratio in combination with spectral analyses for CBL depth estimation. This study will use a version of the methodology proposed by Sikora et al. (1997) to estimate Z_i for both cells and rolls.

The PSD from subsection 3.3 is computed and averaged along the desired axis. Next, a Gaussian filter (standard deviations set to two) is applied on the one-dimensional PSD. This increases the robustness of peak estimation as it smooths over minor anomalous peaks. The calculated power at each frequency is multiplied with its respective frequency to arrive at $n \cdot S(n)$. Lastly, the spatial wavelength of the resulting peak location is extracted and divided by the aspect ratio to arrive at the estimated CBL depth Z_i. As previously mentioned, the ratio of 1.5 does not hold for rolls. For these a ratio of 2.0 is selected as this value approaches the statistical mode of aspect ratios provided in Figure 3 from Wang et al. (2019a). That being said, the ratio of 2.0 is on the low side of values estimated in other literature (e.g. Wackerman et al., 1996; Young et al., 2002).

The choice of analysis axis can influence results. For two-dimensional rolls the analysis can only be performed perpendicular to the axis of greatest variance (as little relevant spectral power exists in the along-wind direction). For three-dimensional cells the analysis axis is not fixed. Sikora et al. (1997) determines Z_i through spectral analysis parallel to the along-wind direction. According to Nicholls and Readings (1981), surface imprints of three-dimensional cells are prone to stretching in the along-wind direction. Similarly, Ufermann and Romeiser (1999) found that three-dimensional cells became elliptical during higher wind

speeds. Stretched cellular structures would lead to spectral peaks at lower frequencies and thus overestimation of the CBL depth. For this reason Young et al. (2000) employs cross-wind spectral analysis. However, for the single Barbados scene with three-dimensional cells (namely January 27th A, see Table 5) the spectral peaks in the axis perpendicular to the direction of greatest variance were less evident than their along-wind counterparts (not shown). For this reason the Z_i values for scenes containing three-dimensional cells are retrieved using along-wind spectral analysis despite the fact that this could lead to Z_i overestimation. Estimates for two-dimensional rolls are unaffected.

3.5 Characterisation

Characterisation of the MABL will follow two approaches outlined by Young et al. (2000) as well as a new third approach. The first approach outlined by Young et al. (2000) relies on total wind-field variance and spectral filtering (algorithm 2A) whereas the second relies on the wind-field variance within the inertial subrange (algorithm 2B). The method proposed by Mourad et al. (2000) and subsequently employed by Sikora et al. (1999, 2000); Sikora and Thompson (2002) is a version of algorithm 2A using spatial filtering rather than spectral filtering. Algorithms 2A and 2B employ surface-layer and a mix of surface- and mixed-layer similarity respectively. Both algorithms require correct estimation of the wind field and its variance as well as an initialisation loop (algorithm 1) in which the stress field and friction velocity are calculated using the GMF-retrieved neutral wind field. An adapted version of algorithm 2B is presented as algorithm 2C which uses surface-layer similarity rather than a mix of surface- and mixed-layer similarity.

3.5.1 Algorithm 1: Surface stress

Wind-induced surface stress τ is related to friction velocity u_* and wind velocity following

$$u_*{}^2 = C_d \overline{U^2}, \tag{3.8a}$$

$$\tau = \rho_{\text{air}} u_*{}^2, \tag{3.8b}$$

where C_d is the drag coefficient, $\overline{U}$ the mean horizontal wind speed and ρ_{air} the air density (Monin and Obukhov, 1954; Kaimal et al., 1976; Champagne et al., 1977; Smith, 1988; Fairall et al., 1996). Similar to the approach of Young et al. (2000) and Sikora et al. (2000), $\overline{U^2}$ is given the value of the observed neutral current relative average wind speed at 10 m height retrieved from the GMF. The drag coefficient C_d is calculated following

$$C_d = \left[\frac{\kappa}{\ln(z) - \ln(z_0) - \psi_m} \right]^2, \tag{3.9}$$

where z is the measurement height (10 m for CMOD5.N and CMOD-IFR2), z_0 the aerodynamic roughness length (the height above the surface at which the wind speed becomes zero (Stull, 1988)) and ψ_m the diabatic wind profile function (Stull, 1988). For neutral conditions ($zL^{-1} = 0$) the ψ_m term becomes zero and C_d will be referred to as C_{dn}. Since neutral wind speed is retrieved from the GMF, C_{dn} will be used in algorithm

Table 1: Algorithm 1.

Step	Equations	Operations	Constants
1	Equation 3.8a	$u_* = \sqrt{C_{dn}\overline{U_n}^2}$	initial guess C_{dn}
2	Equation 3.10	$z_0 = a\frac{{u_*}^2}{g} + 0.11\frac{\nu}{u_*}$	a, g, ν
3	Equation 3.9	$C_{dn} = \left[\frac{\kappa}{\ln(z) - ln(z_0)}\right]^2$	z, κ
4		Iterate till convergence	
Final	Equation 3.8a	$\tau = \rho_{air} C_{dn} {U_n}^2$	ρ_{air}

1. In turn the aerodynamic roughness length z_0 can be calculated according to the Charnock relation as (Charnock, 1955; Smith, 1988; Fairall et al., 1996)

$$z_0 = a\frac{{u_*}^2}{g} + 0.11\frac{\nu}{u_*}. \tag{3.10}$$

The Charnock constant a is an empirical measure used to quantify the sea state (Smith et al., 1996). Fairall et al. (1996); Drennan et al. (1999); Young et al. (2000) use a constant value of 0.011 which is supported by Yelland and Taylor (1996) who found that this value holds well for wind speeds between 6 and 13 ms^{-1}. Stull (1988) notes a value of 0.016 for sea measurements and the ECMWF uses $a \approx 0.015$ during January for the area east of Barbados (Figure 14a in Hersbach, 2010). According to Hersbach (2011), the a value for seas with swell hovers around 0.01 whereas for young steep seas it is closer to 0.04. Typical values fall within this range. For consistency, this study will use a value of 0.011. According to the formula presented in Andreas et al. (1989), the kinematic viscosity of air ν is approximately $1.5 \cdot 10^{-5}$ $\mathrm{m}^2\mathrm{s}^{-1}$ for an air temperature of 293 K.

Because roughness length and friction velocity depend on each other, their values are iteratively solved taking an initial estimate of C_{dn} till convergence of the parameters. Results for this iterative loop include an estimate of z_0, C_{dn} and u_*. Once the iterative results converge, $\overline{U^2}$ in Equation 3.8 can be replaced with a per pixel U_n^2 value which, combined with Equation 3.8b, yields a surface-stress field τ sampled at the same spatial interval as the input wind field. The calculated τ field and the values for z_0, C_{dn} and u_* are used in the successive algorithms. Parameters ρ_{air}, a and ν are approximated rather than retrieved from measurements. According to Donelan et al. (1997) and Drennan et al. (1999), the presence of swell can lead to significant errors in the calculation of the above surface parameters. Algorithm 1 is outlined in Table 1.

3.5.2 Algorithm 2A: Variance approach

Equation 2.1 contains unknown $\overline{w'T_v'}$, which cannot be derived at this stage. Thus, instead of using Equation 2.1, an alternative empirical formulation is employed to calculate Obukhov length L. Panofsky et al. (1977) presents an empirical equation created by curve fitting to data from field experiments. Rewriting this to give L yields

$$L = -\frac{Z_i}{\left[1\frac{2}{3}\left(\left(\frac{\sigma_u}{u_*}\right)^2 - 4\right)\right]^{3/2}}. \tag{3.11}$$

Input parameters are CBL depth Z_i, horizontal wind-field standard deviation σ_u and friction velocity u_*. These parameters are derived either directly or indirectly from the SAR-derived wind field. Z_i is retrieved according to the method of Sikora et al. (1997), u_* is estimated in algorithm 1 and σ_u is retrieved from the one-dimensional spatial wind-field energy spectrum $E(\xi)$. Here one can choose to apply spatial or spectral filters prior to the calculation of $E(\xi)$ in order to only include that portion of the wind-field variance induced by MABL convection. Alternatively, one can simply compute the standard deviation of the wind field to retrieve an unfiltered and overestimated σ_u, as is done in this study.

Having calculated L, its value is used to correct the neutral wind field for atmospheric instability. After all, the original wind field calculated through CMOD was valid for neutral atmospheric stratification only. The recalculated wind field U is computed from τ (retrieved at the end of algorithm 1) and C_d by combining Equation 3.8a and Equation 3.8b to form

$$U = \sqrt{\frac{\tau}{\rho_{\text{air}} C_d}}. \tag{3.12}$$

Because of non-neutral conditions, the stability correction introduced by ψ_m for C_d in Equation 3.9 will no longer be zero. Several equations exist to calculate ψ_m, for unstable conditions, i.e. $\frac{z}{L} < 0$, Young et al. (2000) employs (corrected for typo)

$$\psi_m = \ln\left[\left(\frac{1+x^2}{2}\right)^2\right] - 2\tan^{-1}(x) + \frac{\pi}{2}, \tag{3.13}$$

with empirical constant x calculated by

$$x = \left(1 + 16\left|\frac{z}{L}\right|\right)^{1/4}. \tag{3.14}$$

A new value of σ_u is obtained from the recalculated wind field. Resubmitting this value into Equation 3.11 yields an updated value of L. Iterations of calculating L in order to update the stability correction, the recalculated wind field and in turn σ_u converge within ten iterations.

Once L has successfully been determined, its value is used in Equation 2.1 together with u_* from algorithm 1 and constants g and κ. The mean virtual potential temperature $\overline{T_v}$ is not measured directly. Instead a reasonable estimate will be made. At worst this will lead to a few percent error as even for extreme cases the average temperature will not deviate by more than 10% from 293 K. Submitting the above into Equation 2.1 returns the kinematic flux of virtual potential temperature $\overline{w'T'_v}$. Rewriting the equation in terms of $\overline{w'T'_v}$ yields

Table 2: Algorithm 2A.

Step	Equations	Operations	Constants
1	Equation 3.14	$x = \left(1 + 16\left\lvert\frac{z}{L}\right\rvert\right)^{1/4}$	z, initial guess L
2	Equation 3.13	$\psi_m = \ln\left[\left(\frac{1+x^2}{2}\right)^2\right] - 2\tan^{-1}(x) + \frac{\pi}{2}$	-
3	Equation 3.9	$C_d = \left[\frac{\kappa}{\ln(z)-\ln(z_0)-\psi_m}\right]^2$	z, κ, z_0 from algorithm 1
4	Equation 3.12	$U = \sqrt{\frac{\tau}{\rho_{\text{air}} C_d}}$	ρ_{air}, τ from algorithm 1
5	Equation 3.1 Equation 3.2	$U \rightarrow E(\xi)$	
6	Equation 3.3	$E(\xi) \rightarrow \sigma_u$	
7	Equation 3.11	$L = -\frac{Z_i}{\left[1\frac{2}{3}\left(\left(\frac{\sigma_u}{u_*}\right)^2 - 4\right)\right]^{3/2}}$	Z_i from subsection 3.4, u_* from algorithm 1
8		Iterate till convergence	
Final	Equation 3.15	$\overline{w'T_v'} = -\frac{{u_*}^3 \overline{T}_v}{L\kappa g}$	κ, g, estimate of $\overline{T_v}$, u_* from algorithm 1

$$\overline{w'T_v'} = -\frac{{u_*}^3 \overline{T}_v}{L\kappa g}. \tag{3.15}$$

Algorithm 2A is outlined in Table 2.

Multiple versions exist of the empirical formulae used above. For alternative empirical equations to calculate L refer to Panofsky et al. (1977) and Caughey and Palmer (1979) with a recent version provided by Wilson (2008). For strongly unstable conditions all versions give similar values. Significant differences are observed when approaching near neutral conditions (large $|L|$'s). Equation 3.11 returns imaginary values for $\sigma_u/u_* < 2$ although, due to the asymptotic behaviour nearing this point, iterations of the equation tend to fail nearer to $\sigma_u/u_* < 2.5$. The onset of asymptotic behaviour depends on which equation was used. Similarly, different authors provide different equations to compute ψ_m and x. For these refer to Paulson (1970), Young and Kristensen (1992) and Larsén et al. (2004). Of particular interest are those provided by Larsén et al. (2004) as they derive the equations as a function of wave age (while taking into account the effect of swell) and hypothesise an additional dependence on Z_i/L, albeit using a limited sample size.

3.5.3 Algorithm 2B: Inertial subrange approach

The inertial subrange segment of the turbulence spectrum is used in an alternative analysis approach. Rather than analysing the total wind-field variance within an image, one can analyse the variance of the inertial subrange only. This requires a portion of the inertial subrange to follow the -5/3 power law in the one-dimensional spectrum. Because this approach is normalised with frequency, it does not matter at which frequency in the inertial subrange the analysis is performed as long as it falls on the -5/3 slope. The greater the portion of the -5/3 slope considered, the more one can average results. Unlike the variance approach, no spectral (or spatial) filtering is necessary as only (a portion of) the inertial subrange is of interest.

Contamination of the inertial subrange by signals other than the MABL can naturally lead to failure of this method. As both approaches rely on the information contained in the one-dimensional spectrum, they are not truly independent. According to Kaimal et al. (1976) the convective velocity scale w_* is calculated from the PSD following

$$w_* = \sqrt{\frac{(2\pi)^{2/3} {f_i}^{2/3} n S(n)}{\alpha \beta \psi^{2/3}}}, \tag{3.16}$$

where n is temporal frequency which can be calculated from spatial frequency ξ following Equation 3.6, $S(n)$ is the along- or cross-wind PSD at the specified frequency in the inertial subrange, α the Kolmogorov constant of approximately 0.5 (e.g. Kaimal et al., 1976; Smedman et al., 2007, in an overview study Sreenivasan (1995) found α to be closer to 0.53 for scenarios representative of atmospheric surface-layer turbulence), β the isotropy correction factor of 1 and $\frac{4}{3}$ for along- and cross-wind analyses respectively (Kaimal et al., 1976; Caughey and Palmer, 1979; Smedman et al., 2007) and ψ the dimensionless energy dissipation rate for which near-surface overland values appear to fall between 1.0 and 2.5 according to Figure 4 in Kaimal et al. (1976). Considering the observed asymptotic behaviour of near-surface dissipation rates presented in said figure, dissipation rates larger than 2.5 would seem possible depending on the observed z/Z_i. Results obtained in Young et al. (2000) used a mixed-layer value of $\psi = 0.6$, which, according to Young (2000), is valid for buoyancy-driven unstable surface layers. Unless stated otherwise, results in this study are obtained using $\psi = 1.0$. Lastly, f_i represents the dimensionless frequency calculated following

$$f_i = \frac{n Z_i}{\overline{U}}. \tag{3.17}$$

A value for the convective velocity scale, $w_{*,i}$, is obtained for each analysed frequency n_i within the inertial subrange. These values should be near identical meaning they can be averaged to form a single convective velocity scale, w_*, representative of the entire inertial subrange. However, if the inertial subrange is of poor quality or poorly constrained, the observed slope can deviate from the -5/3 powerlaw. Thus, in addition to the spectrum amplitude filter described in subsection 3.3, the spread in $w_{*,i}$ estimates will be used as a second quality filter. If the standard deviations of $w_{*,i}$ estimates are relatively high, the corresponding quality will be considered poor, leading to its exclusion from further calculations. The standard deviations are normalised by dividing with the median $w_{*,i}$ value such that a single threshold can be set for all amplitudes. Unless stated otherwise, this threshold is set to 0.15. Prior to calculating either the mean or normalised standard deviation, all $w_{*,i}$ values are weighted with respect to their frequency, e.g. if the lowest spatial wavelength in the inertial subrange is 650 m than it receives a weight of 1, 975 m receives a weight of 1.5 and 1300 m receives a weight of 2. Weighting reduces the bias caused by the increasing quantity of high frequencies. The final value of w_* is combined with Equation 2.2 which, when rewritten as

$$\overline{w'T'_v} = \frac{{w_*}^3 T_v}{g Z_i}, \tag{3.18}$$

returns the kinematic heat flux $\overline{w'T'_v}$. Plugging the $\overline{w'T'_v}$ value back into a rearranged form of Equation 3.15

Table 3: Algorithm 2B.

Step	Equations	Operations	Constants
1	Equation 3.6	$n = \xi\overline{U} \cdot \chi$	$\chi = 1$ for first iteration
2	Equation 3.17	$f_i = \frac{nZ_i}{\overline{U}\cdot\chi}$	Z_i from subsection 3.4, $\chi = 1$ for first iteration
3	subsection 3.3	$U \cdot \chi \rightarrow S(n)$	$\chi = 1$ for first iteration
4	Equation 3.16	$w_* = \sqrt{\frac{(2\pi)^{2/3} {f_i}^{2/3} nS(n)}{\alpha\beta\psi^{2/3}}}$	$\alpha,\ \beta,\ \psi$
5	Equation 3.18	$\overline{w'T'_v} = \frac{{w_*}^3 T_v}{gZ_i}$	g, Z_i from subsection 3.4, estimate of $\overline{T_v}$
6	Equation 2.1	$L = -\frac{\overline{T}_v u_*^3}{\kappa g \overline{w'T'_v}}$	κ, g, u_* from algorithm 1, estimate of $\overline{T_v}$
7	Equation 3.14	$x = \left(1 + 16\left\lvert\frac{z}{L}\right\rvert\right)^{1/4}$	z
8	Equation 3.13	$\psi_m = \ln\left[\left(\frac{1+x_1^2}{2}\right)^2\right] - 2\tan^{-1}(x_1) + \frac{\pi}{2}$	
9	Equation 3.19	$\chi = 1 - \left(\frac{\psi_m\sqrt{C_{dn}}}{\kappa}\right)$	κ, C_{dn} from algorithm 1
10		Iterate till convergence	
Final	rewritten Equation 3.11	$\sigma_u = u_*\sqrt{4 + 0.6\left(\frac{-Z_i}{L}\right)^{2/3}}$	Z_i from subsection 3.4, u_* from algorithm 1

gives L. The estimated parameters require a stability correction to account for the unstable atmospheric stratification. Young et al. (2000) calculates a stability correction factor χ as

$$\chi = 1 - \left(\frac{\psi_m\sqrt{C_{dn}}}{\kappa}\right), \tag{3.19}$$

where C_{dn} is retrieved from algorithm 1 and ψ_m is computed by plugging the obtained value of L into Equation 3.14 to get x and subsequently ψ_m. Next χ is multiplied with the mean wind speed $\overline{U}$ of Equation 3.17 and the wind field U prior to calculation of $S(n)$ in Equation 3.16. The values for f_i, $S(n)$ and w_* are updated iteratively until convergence. Algorithm 2B is outlined in Table 3. At the end of algorithm 2B one can rewrite Equation 3.11 in terms of σ_u to compare outputs with algorithm 2A.

An interesting difference between the approaches of algorithms 2A and 2B relates to their respective dependence on Z_i. For algorithm 2A it follows from Equation 3.11 that

$$-L \propto Z_i, \tag{3.20}$$

whereas L calculated in algorithm 2B is (mostly) independent of Z_i, since

$$\frac{1}{-L} \propto \overline{w'T'} \propto \frac{{w_*}^3}{Z_i} \propto \frac{\left(\sqrt{{f_i}^{2/3}}\right)^3}{Z_i} \propto \frac{\left(\sqrt{{Z_i}^{2/3}}\right)^3}{Z_i} \propto \frac{\left({Z_i}^{1/3}\right)^3}{Z_i} \propto 1 \tag{3.21}$$

The only dependence on Z_i in algorithm 2B stems from the inertial subrange being selected up to the spatial

wavelengths associated with the microscale peak, which is itself a function of Z_i. This indirect dependence is greatest for poorly estimated inertial subranges which are detected based on $w_{*,i}$ spread and subsequently removed from the analysis. Thus, w_* estimates from the remaining inertial subranges are mostly independent of Z_i.

3.5.4 Algorithm 2C: Turbulent kinetic energy dissipation rate approach

The power within the inertial subrange is used in a third characterisation approach. For algorithm 2C, surface-layer spectral characteristics are employed instead of the mixed-layer spectral characteristics from algorithm 2B. The former is likely more applicable for the 10 m height wind fields retrieved from the GMF. According to Lundquist and Bariteau (2015), the turbulent kinetic energy (TKE) dissipation rate ϵ for unstable conditions is calculated as

$$\varepsilon = \left(\frac{2\pi}{\overline{U}}\right)\left[\frac{n^{5/3}S\left(n\right)}{\alpha\beta}\right]^{3/2}. \tag{3.22}$$

The notable difference between this equation and Equation 3.16 relates to the dependence on ψ. Similar to algorithm 2B, an isotropy correction factor β is included for cross-wind analyses (e.g. Nicholls and Readings, 1981; Oncley et al., 1996). For along-wind analyses $\beta = 1$ and can thus be ignored. Near-surface scaling parameters can be estimated using the obtained ϵ following (Fairall et al., 1990)

$$\phi_e\left(\frac{z}{L}\right) = \frac{\varepsilon\kappa z}{{u_*}^3}. \tag{3.23}$$

The empirical fits to the dimensionless gradient profile function ϕ_ϵ provided in early literature were developed for $\kappa = 0.35$ (e.g. Wyngaard and Coté, 1971; Kaimal et al., 1972). In an overview study of eleven different field studies Kooijmans and Hartogensis (2016) presents an empirical fit which accounts for $\kappa = 0.4$

$$\phi_e\left(\frac{z}{L}\right) = 0.88\left[\left(1 - 2.06\frac{z}{L}\right)^{-1/4} - \frac{z}{L}\right], \tag{3.24}$$

A Monte-Carlo approach is applied to solve Equation 3.24 for Obukhov length L. If Equation 3.23 yields $\phi_e < 0.88$, no solution can be obtained from Equation 3.24. Having obtained L, a stability correction χ is calculated and applied in a similar fashion as for algorithm 2B. Iterations are performed till convergence. Similar to algorithm 2B, an inertial subrange normalised standard deviation filter is applied.

In essence algorithm 2C is identical to algorithm 2B as the analysis relies on the power within the inertial subrange. The main difference relates to the dependencies of w_* and ϵ; unlike algorithm 2B, algorithm 2C is unaffected by the uncertainty relating to ψ. As an additional benefit algorithm 2C does not rely on Z_i, which is a source of uncertainty for algorithm 2A.

Algorithm 2C is not without its own shortcomings. For $|z/L| < 0.2$ the empirical fits to ϕ_ϵ, either from Wyngaard and Coté (1971); Kaimal et al. (1972) or Kooijmans and Hartogensis (2016), struggle to account for the observed spread in ϵ and thus ϕ_e, see Figure 3.5. This could indicate other parameters at play which are

Table 4: Algorithm 2C.

Step	Equations	Operations	Constants
1	Equation 3.6	$n = \xi\overline{U} \cdot \chi$	$\chi = 1$ for first iteration
2	subsection 3.3	$U \cdot \chi \rightarrow S(n)$	$\chi = 1$ for first iteration
3	Equation 3.22	$\varepsilon = \left(\frac{2\pi}{\overline{U}}\right)\left[\frac{n^{5/3}S(n)}{\alpha\beta}\right]^{3/2}$	$\alpha,\ \beta$
4	Equation 3.23	$\phi_e\left(\frac{z}{L}\right) = \frac{\varepsilon\kappa z}{{u_*}^3}$	κ, z, u_* from algorithm 1
5	Equation 3.24	$\phi_e\left(\frac{z}{L}\right) \rightarrow L$	range of L estimates to select reasonable L
6	Equation 3.14	$x = \left(1 + 16\left\lvert\frac{z}{L}\right\rvert\right)^{1/4}$	z
7	Equation 3.13	$\psi_m = \ln\left[\left(\frac{1+x^2}{2}\right)^2\right] - 2\tan^{-1}(x) + \frac{\pi}{2}$	
8	Equation 3.19	$\chi = 1 - \left(\frac{\psi_m\sqrt{C_{dn}}}{\kappa}\right)$	κ, C_{dn} from algorithm 1
9		Iterate till convergence	
Final	rewritten Equation 3.11	$\sigma_u = u_*\sqrt{4 + 0.6\left(\frac{-Z_i}{L}\right)^{2/3}}$	Z_i from subsection 3.4, u_* from algorithm 1

not directly incorporated in the formulation. Considering the observed spread of ϕ_e and that for CMOD5.N $z = 10$ m, for characterisation this implies algorithm 2C will perform poorly for $|L| > 50$ m. Moreover, though Equation 3.23 may be less sensitive to the natural spread in ϵ for $|L| < 10$ m, Figure 3.5 shows the equation was fitted to few data points with a high degree of relative uncertainty. In other words, algorithm 2C is expected to provide reasonable results for a small stability range only; the scatter of ϕ_e complicates the use of algorithm 2C for relatively high values of $|L|$ whereas for lesser values of $|L|$ algorithm 2C suffers from propagated uncertainty originating from the empirical fit. Algorithm 2C is outlined in Table 4.

When the observed stability range is favourable, algorithm 2C can be used in combination with algorithm 2A and 2B for calibration and derivation of dimensionless dissipation rate ψ, see subsection 5.2.

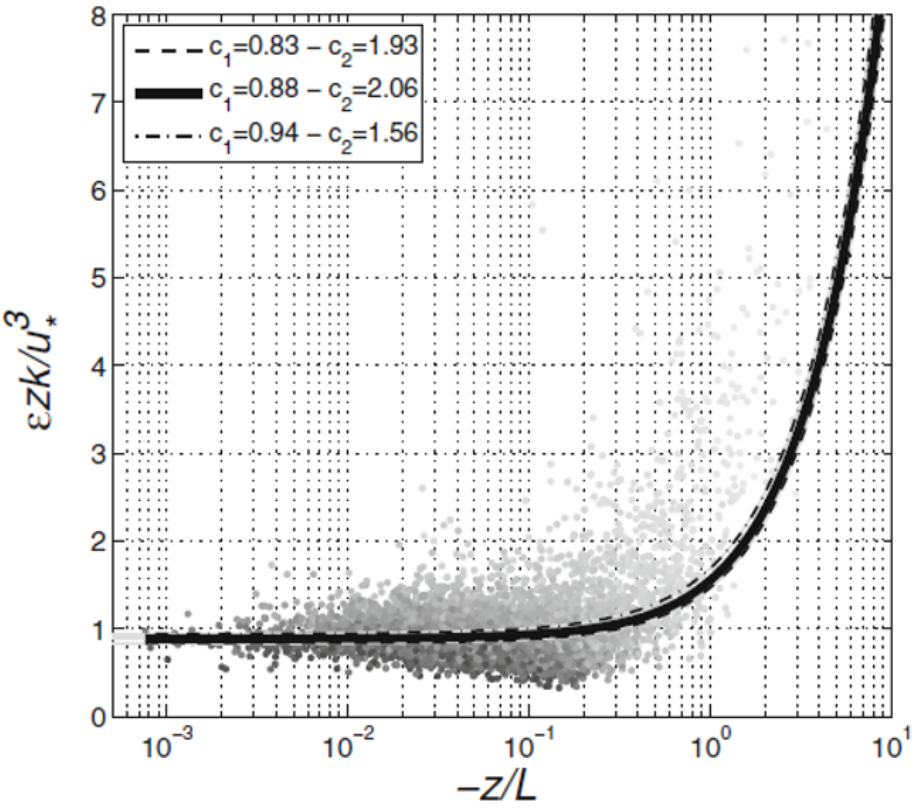

Figure 3.5: Y-axis is equal to ϕ_e. Gray dots represent data obtained from several field studies. Data uncertainty is represented by colour code, lighter colours indicate higher uncertainty. The black line represents the fit through the data, i.e. Equation 3.24. Plot retrieved from Kooijmans and Hartogensis (2016).

Description of data

The data of this study concerns two separate study areas. The Barbados study area covers the sea east of Barbados and the miscellaneous study areas cover various coastal parts of the Atlantic and Pacific, see Figure 4.1. The Barbados study area enjoys ample validation data from which all characterisation results can be validated whereas the miscellaneous study areas provide insight into characterisation performance under a broader range of atmospheric circumstances at the cost of less available validation data. The validation methods and datasets for the Barbados and miscellaneous study areas are included in the relevant chapters.

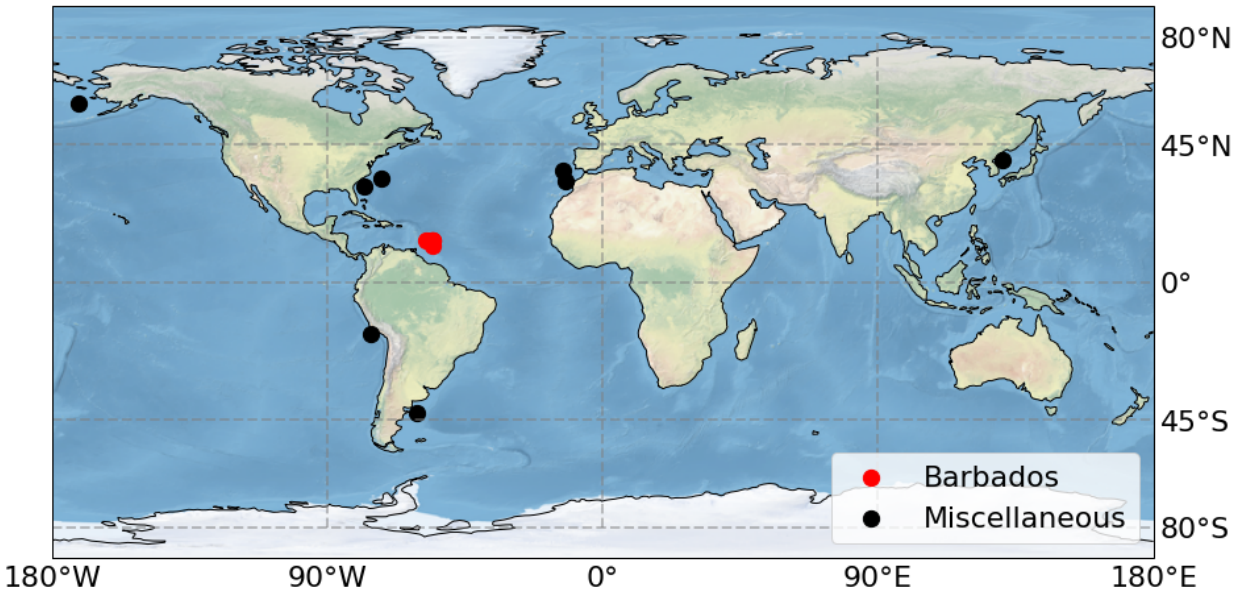

Figure 4.1: Location of various Sentinel-1 scenes subdivided into two study areas.

4.1 Barbados data

The main study area is located to the east of Barbados in the so-called trade wind alley (Stevens, B. et al., 2021). For this region validation data is available from the 2020 EUREC^{4}A campaign. The Sentinel-1 (S1) scenes for the Barbados area are presented in Figure A.1 with their respective overpass details in Table 5. Each radar scene is divided into several 25^2 km^2 tiles where each tile is composed of 83 by 83 pixels at 300 m resolution in both directions. Figure 4.2 contains a tiling example for January 27th B. The tile size proved large enough to provide repeatable results (since each tile contains similar amounts of either rolls or cells) whilst remaining sufficiently small to limit inhomogeneities (and thus invalidation of similarity theories (Khanna and Brasseur, 1997) and contamination of the two-dimensional spectrum). Additionally, at sixty tiles for a regular S1 Interferometric Wide (IW) swath scene, redundancy allows for the filtering of low-quality tiles. The choice of tile size is open for debate; the study area in Young (2000) is 37.5^2 km^2 whereas that in Sikora et al. (1997) is 5^2 km^2.

Prior to analysis each radar scene is classified as being dominated by two-dimensional rolls or three-dimensional cells since either convection mode requires slightly different processing approaches. A two-

pronged classification is performed. Each scene is classified using a custom binary Convolutional Neural Network (CNN) trained on a portion of the dataset retrieved from Wang et al. (2019b). The CNN classifies the individual tiles of the radar scenes as containing either two-dimensional rolls or three-dimensional cells after which the entire scene is classified as the majority mode of the individual tiles. This decreases classification outliers at the cost of worse classification spatial resolution. In addition to the automatic CNN classification, visual inspection is performed by comparing the two-dimensional orientation of greatest variance of the image spectra with the wind directions derived from the validation source. If these align the convection likely consists of three-dimensional cells whereas an approximate 90° offset indicates two-dimensional rolls. According to the CNN classifier all Barbados scenes were dominated by two-dimensional rolls. This assessment is supported by manual inspection results according to which all scenes but January 27th A were dominated by two-dimensional rolls. The January 27th B scene contains a sharp discontinuity and February 20th contains several patches of discontinuities. These will affect local results because the introduced wind variance of this discontinuity causes the turbulence spectra to deviate from the ideal turbulence spectra. Fortunately these discontinuities can be detected and removed through filtering, as described in subsubsection 3.5.3

Surface currents near Barbados are expected to manifest themselves as underestimation of the wind-field magnitude since the two main regional surface currents, namely the North Equatorial Current and the North Brazil Current, are directed approximately west-north-west (Schott et al., 2002; Barbie Bischof, 2003) along the observed easterly winds of the trade wind alley. Based on the location of the Barbados study area and the magnitudes of the two respective surface currents, the mean surface current is expected to be in the order of $\mathcal{O}$(cm) (e.g. Arnault, 1987; Bourlès et al., 1999). This would lead to an equal order underestimation of the wind-field magnitude.

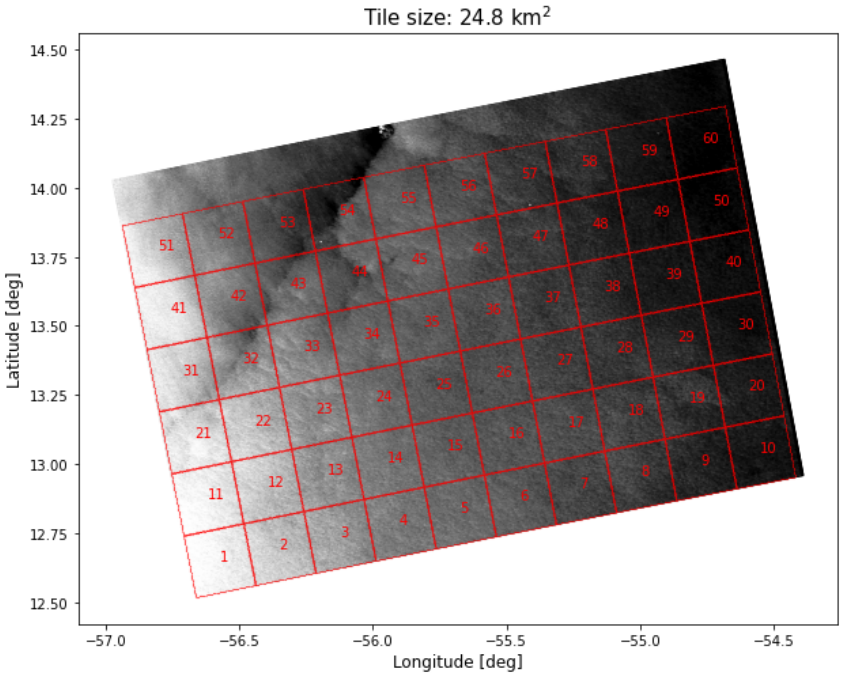

Figure 4.2: Scene January 27th B tiled into sixty equal sized squares.

Table 5: Metadata Barbados scenes.

Short name	Date	Path	Frame	Orbit	Mode	Polarisation	Abs. Orbit
Jan 15th	15-01-2020 21:54	120	1224	Ascending	IW	VV	30817
Jan 27th A	27-01-2020 21:53	120	1219	Ascending	IW	VV	30992
Jan 27th B	27-01-2020 21:54	120	1224	Ascending	IW	VV	30992
Feb 1st	01-02-2020 22:02	18	1224	Ascending	IW	VV	31065
Feb 8th	08-02-2020 21:54	120	1224	Ascending	IW	VV	31167
Feb 20th	20-02-2020 21:54	120	1224	Ascending	IW	VV	31342

4.2 Barbados validation

Results of the Barbados characterisation approaches are validated using several data sources. These include field measurements of the EUREC^{4}A campaign, optical satellite imagery and ECMWF atmospheric parameters (both from the Sentinel-1 Ocean product and the ERA5 database). The ideal validation data has identical spatial and temporal coverage compared to the testing data. The EUREC^{4}A campaign validation data is primarily composed of point observations whereas the data to be validated concerns large spatial extents. Taylor's hypothesis, which relates spatial and temporal scales, is invoked in order to compare these different scales and optical imagery is analysed in order to justify use of this hypothesis.

The EUREC^{4}A campaign spanned the early months of 2020 and covered the ocean to the east and south of Barbados. A complete description of the field campaign is provided in Stevens, B. et al. (2021). The research area of this study was selected to overlap with that of the EUREC^{4}A campaign in order to benefit from its vast quantity of observations. The EUREC^{4}A measurements used for validation include those made by instruments onboard research vessel (R/V) Meteor as well as a saildrone. Higher-level products of these measurement stations were not available at the time of research. Instead the in-situ measurements were used to compute higher-level products.

Validation data from both the R/V Meteor and saildrone are derived from two hours pre and post S1 observation, if available. Assuming Taylor's hypothesis, this spatially translates to approximately three to five 25^2 km^2 tiles centred at the observation point. Thus, the validation data from the measuring platforms represent a much smaller area than the S1 footprint. Limiting the comparisons to such scales would lead to the exclusion of most Barbados scenes since all validation data other than that from the R/V Meteor for February 1st and the saildrone for February 8th and February 20th were obtained from platforms outside the S1 footprint. This should be kept in mind when comparing SAR-derived values and validation-derived values since they are inherently unequal.

4.2.1 Research vessel Meteor

The research vessel (R/V) Meteor provided a host of convenient measurement systems including a ceilometer, cloud radar, wind lidar, radiosondes and eddy-covariance measurement systems. Each of these systems will be elaborated on below. A full description of the R/V Meteor can be found online at `http://eurec4a.eu/platforms/rv-meteor`. The predecessor and namesake to the R/V Meteor provided measurements used to study the vertical structure of the atmosphere in Augstein et al. (1974), whose conclusions were in turn used in this study. In other words, this study directly relies on knowledge obtained from the "old" and "new" R/V Meteor.

4.2.1.1 Ceilometer and cloud radar Both ceilometer data and cloud radar images, available at EUREC^{4}A (2020a) and EUREC^{4}A (2020b) respectively, will be used to derive the cloud base height. Since the cloud layer is located at the top of the mixed layer (Augstein et al., 1974; Stull, 1988), cloud base height can be used as a proxy for Z_i. A ceilometer uses optical wavelengths to determine the cloud base height. This tool yields good temporal resolution but it requires clouds to be present in order for it to make meaningful measurements. Meanwhile the cloud radar is capable of providing information on clouds beyond the first layer due its use of radio wavelengths. This also enables the cloud radar to detect rain events. In this study only the cloud radar's retrieved reflectivity profiles are used.

The interpretation of example ceilometer and cloud radar data is given to illustrate the method of Z_i deduction. Both the morning and evening S1 overpass on January 25th and the evening overpass on January 27th appeared to contain convective signatures in their respective radar imagery. The respective ceilometer and cloud radar measurements can be found in Figure 4.3 and Figure 4.4. Ceilometer data on the 25th shows erratic cloud base behaviour during the morning overpass. The cloud radar observations confirm that this was caused by a rain event. No further analyses were performed on data acquired over the 25th as the uncorrupted evening overpass occurred during a period of technical difficulties.

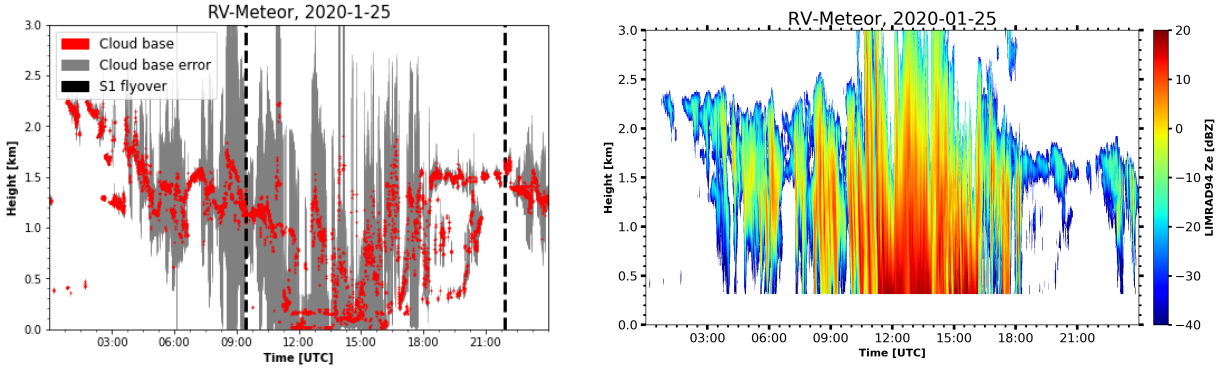

(a) Ceilometer **(b)** Cloud radar

Figure 4.3: Ceilometer and cloud radar data obtained onboard R/V Meteor on the 25th of January 2020. Cloud radar images retrieved from EUREC^{4}A (2020b).

On the 27th the cloud radar was down with technical difficulties, resulting in no measurements. Fortunately the scene does not have to be discarded because the ceilometer measurements can be used instead. The ceilometer displays two cloud bases: one at approximately 600 m and another briefly at 2000 m. The cloud base at 600 m likely represents the condensation level at the top of the mixed layer. It will be selected as Z_i. This base appears relatively constant in height during the day but tapers off during the evening as incoming solar radiation decreases. The cloud base at approximately 2000 m could represent clouds spreading laterally after reaching the trade inversion height, far beyond the relevant mixed layer.

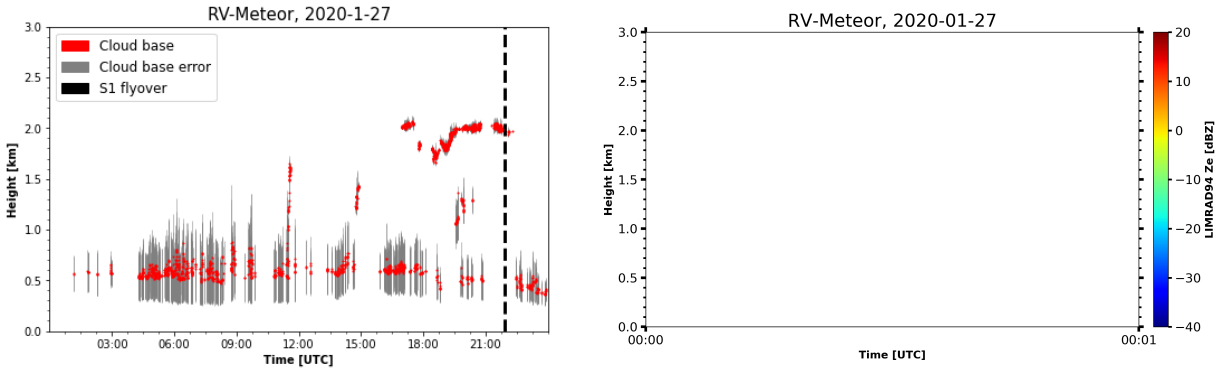

(a) Ceilometer **(b)** Cloud radar

Figure 4.4: Ceilometer and cloud radar data obtained onboard R/V Meteor on the 27th of January 2020. Cloud radar images retrieved from EUREC^{4}A (2020b).

4.2.1.2 Radiosonde More precise estimates of Z_i can be retrieved from radiosonde data available at EUREC^{4}A (2020c). Radiosondes released from the R/V Meteor measured detailed profiles up to an altitude of several kilometres. At the first inversion layer one expects to find strong vertical gradients of temperature and humidity (e.g. Malkus, 1958; Augstein et al., 1974; Stull, 1988). The height corresponding to these large gradients is taken as Z_i. The radiosonde data has a vertical spacing of 10 m. At such a resolution the gradients can appear quite erratic. Retrieved temperature profiles are smoothed with a one-dimensional Gaussian filter (sigma = 3) after which the gradients are calculated with a simple derivative. Next the temperature gradient and relative humidity are plotted up to an altitude of 4000 m. Altitudes beyond that level fall outside the reasonable range of Z_i. The approximate height of Z_i is visually determined from the plots corresponding closest in time with the S1 overpass. According to Stull (1988), the vertical variability of Z_i at equilibrium may be less than 10% over an horizontal extent of 1000 km. Thus, if the radiosonde measurement was acquired within a 100 km from the S1 footprint, its derived value of Z_i will be accepted as a reasonable estimate. By combining information from the ceilometer, cloud radar and the radiosondes a single amalgamated value of Z_i is retrieved. In the results this value is presented as $Z_{i,\ RV}$.

An example of radiosonde data acquired on February 8th is presented in Figure 4.5. On this date a S1 image was acquired close to the R/V Meteor at approximately 22:00 hours. Both the radiosonde before and after acquisition, 20:16 and 22:45 respectively, display a sharp transition at approximately 1800 m which, once again, is deemed to be the trade inversion height beyond the relevant mixed layer. Hence this inversion is ignored. At lower altitudes of approximately 650 and 900 m, at 20:16 and 22:45 respectively, one can find local maxima of relative humidity and increased gradients of temperature. Furthermore, below these respective heights the vertical temperature gradient is significantly smaller than over the remaining profile, indicating a well-mixed layer. Hence a value between 650 and 900 m will be used as the Z_i validation height. This height range corresponds to the Z_i estimated from the ceilometer and cloud radar data retrieved on the 8th of February (not shown). Based on these ancillary data sources, the increasing trend of Z_i visible in the ceilometer data and the maximum relative humidity values at 20:16 and 22:45 respectively, the $Z_{i,\ RV}$ value during the S1 overpass is estimated to be near 850 m.

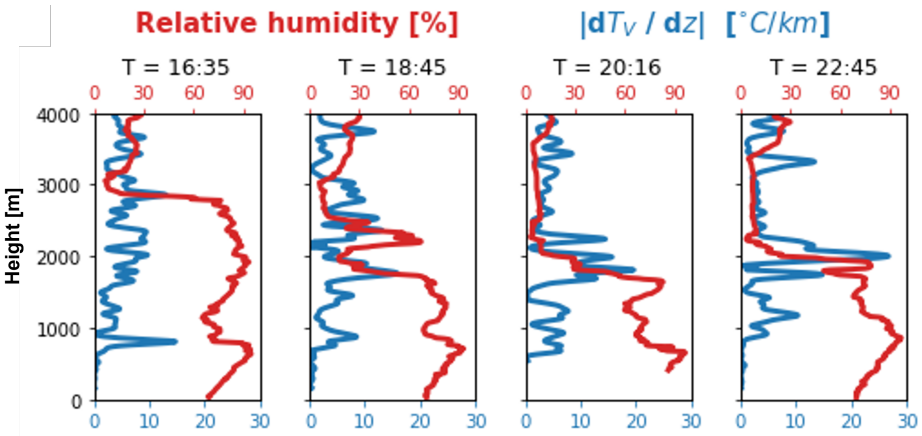

Figure 4.5: Radiosonde profiles acquired on February 8th, released from R/V Meteor, see Figure A.6.

4.2.1.3 Wind lidar The lidar onboard the R/V Meteor measured wind speed and orientation from four different directions for heights ranging between 40 and 250 m. The data is to be published in Baranowski et al. (2021). The preliminary data used in this study had previously been corrected for ship motion. The wind speeds of all four directions are averaged to obtain a single wind speed per 30 minutes, which decreases noise and yields the same temporal sampling as the eddy-covariance measurements. The wind speed at 10 m height U_{10} is estimated by extrapolating and fitting to a logarithmic wind-speed profile between heights 40, 60, 70, 80, 90, 100 and 110 m. Figure 4.6 shows forty-three out of forty-eight extrapolated wind-speed profiles made for January 27th. The remaining five profiles were removed as their U_{10} was greater than their U_{40}. Some scatter is still visible in the 40 to 110 m segments of several profiles. This could be reduced by further temporal averaging at the cost of temporal resolution. Depending on the degree of atmospheric instability, the wind-speed profiles might not follow logarithmic patterns (Archer et al., 2016). In that case either longer temporal averages or different fits entirely should be used to determine U_{10}.

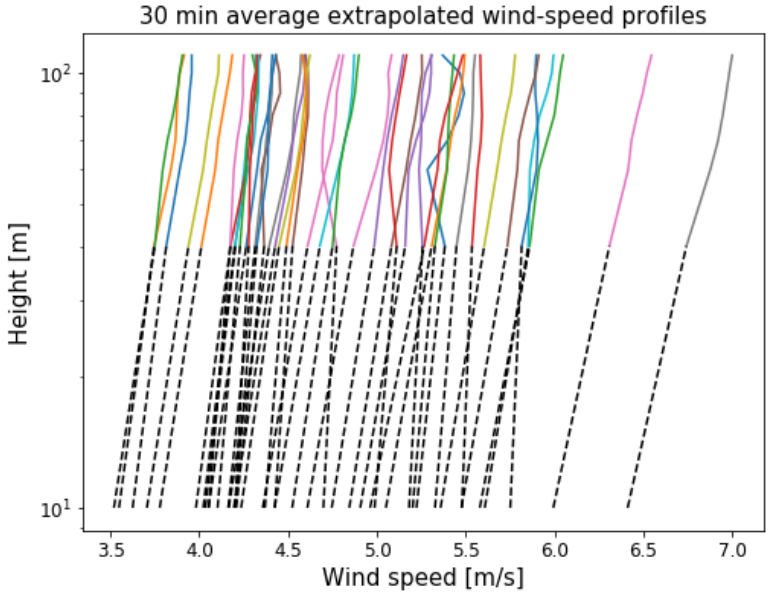

Figure 4.6: Examples of fitted wind-speed profiles based on lidar wind measurements for scene January 27th.

4.2.1.4 Eddy-covariance meteor The R/V Meteor measured latent and sensible heat fluxes between the 15th of January and the 25th of February. The data is to be published in Baranowski et al. (2021). Preliminary data made available for this study includes 30 min averages of latent and sensible heat measured from the mast. The Obukhov length L can be determined by combining this data with U_{10} retrieved from the wind lidar. This is accomplished through an iterative scheme similar to algorithm 1 and algorithm 2A. No stability correction is applied to the wind-speed estimates as they are in-situ measurements rather than measurements obtained under a hypothetical neutral stratification.

First x and ψ_m are calculated using Equation 3.14 and Equation 3.13 with an initial estimate of L. Next z_0 and C_d are calculated using Equation 3.10 and Equation 3.9 with an initial estimate of u_*. Then u_* is recalculated using Equation 3.8a where the lidar value of U_{10} is used for $\overline{U}$. Lastly L is calculated following (Verburg and Antenucci, 2010)

$$L = \frac{-u_*^3 \rho_{\text{air}} T_v}{\kappa g \left(\frac{H}{c_p} + 0.61 \frac{T_v E}{L_v} \right)}. \tag{4.1}$$

New parameters in Equation 4.1 are latent heat flux E (energy transfer in the form of phase changes, such as evaporation), sensible heat flux H (energy transfer in the form of temperature changes), the specific heat of air C_p of 1005 J kg^{-1} K^{-1} (Alpers and Brümmer, 1994) and latent heat of vaporisation L_v. The latter is calculated following

$$L_v = 2.501 \cdot 10^6 - 2370 T_0, \tag{4.2}$$

where T_0 represents the water surface temperature in °C (Verburg and Antenucci, 2010). Approximating this value as 20 °C will, at most, lead to a few percent error. Similarly, T_v will be approximated by 293 K. Convergence is typically achieved in less than ten iterations, yielding 30 min average values of L. These are used as validation for the SAR-derived values of L. Valid measurements from both the eddy-covariance system and wind lidar are required to calculate L. Combining the retrieved value of L with the estimated values of u_* and Z_i yields a R/V Meteor estimate of σ_u.

4.2.2 Saildrone

Saildrones were among the measuring platforms used during the EUREC^{4}A campaign. These unmanned vehicles measured bulk fluxes in coordination with the neighbouring research vessels. A full description of the drones can be found online at `http://eurec4a.eu/platforms/saildrones` with data provided in Quinn, Patricia K et al. (2021).

4.2.2.1 Bulk fluxes The saildrone measures surface stress τ, wind speeds U_{10}, specific humidity r_{10} (g kg^{-1}), sea surface temperature T_{SST} and air temperature T_{10}. Combining these parameters allows for the calculation of L. Friction velocity u_* is computed from τ following an inverse of Equation 3.8b where it is still assumed that ρ_{air} is 1.2 kg m^{-3}. Next the drag coefficient C_d is calculated by combining the known values for τ and U_{10} in

$$C_d = \frac{\tau}{\rho_{\text{air}} {U_{10}}^2}. \tag{4.3}$$

This equation is the combination of Equation 3.8a and Equation 3.8b. No iterations nor stability corrections are performed as the wind speed is obtained from in-situ measurements and τ is known. Following Alpers and Brümmer (1994) it is assumed that the heat transfer coefficient C_H is approximately equal to the drag coefficient C_d, i.e.

$$C_H \approx C_d. \tag{4.4}$$

The temperature difference ΔT is computed following

$$\Delta T = T_{10} - T_{\text{SST}}. \tag{4.5}$$

The parameters are combined to compute sensible heat flux H following

$$H = -\rho_{\text{air}} C_p C_H U_{10} \Delta T. \tag{4.6}$$

For the considered conditions the air temperature is lower than the sea surface temperature, i.e. $\Delta T < 0$ K. The negative sign in the H calculation results in a positive flux directed upwards into the atmosphere. Heat flux H is converted to kinematic heat flux $\overline{w'T'}$ following

$$\overline{w'T'} = \frac{H}{\rho_{\text{air}} C_p}. \tag{4.7}$$

The virtual potential temperature is calculated following (Stull, 1988; Donelan et al., 1997)

$$T_v = (T_{10} + 273.15)\,(1 + 0.61 R_{10})\,. \tag{4.8}$$

Where R_{10} is calculated by dividing the specific humidity by a factor 1000 to get units of kg kg^{-1},

$$R_{10} = \frac{r_{10}}{1000}. \tag{4.9}$$

For the final step T_v, $\overline{w'T'}$, u_* and known constants κ and g are used to compute the Obukhov length L with Equation 2.1. Combining the retrieved value of L with u_* and Z_i (retrieved from the R/V Meteor) yields a saildrone estimate of σ_u.

4.2.3 GOES-E optical imagery

Even on a local scale the atmospheric setting can change rapidly, such as near atmospheric fronts. For all Barbados scenes either one or both validation measurement platforms were located outside of the radar footprint. Optical imagery with a greater footprint than that of S1 was assessed in order to determine whether measurements from these exterior platforms are representative for the area within the footprint. To this end the cloud structures at the respective locations are compared in a qualitative sense. Similar cloud structures are a good indication of similar atmospheric conditions because convection-induced surface signatures are tied to that of cloud signatures, e.g. up- and downdrafts of two-dimensional rolls yields similar structures in the clouds and on the water surface.

Using Geostationary Operational Environmental Satellite-East (GOES-E) video time series provided online at EUREC^{4}A (2020d), the cloud structure outside the radar footprints were analysed. From these it was determined that the cloud structures at measurement platforms just outside the radar footprint are representative of the structure within the footprint for all scenes but January 27th A and January 27th B. Both scenes on the 27th happen to be located to east of an atmospheric front whereas the R/V Meteor is located to west. This could in fact have been deduced from the sharp transition in the top left corner of the radar imagery in Figure A.4. Thus the measurements from the R/V Meteor on the 27th of January might be less representative for the area within the radar footprint. Due to the apparent similar cloud structure, extra validation data is provided for January 27th A, January 27th B and February 1st from saildrone measurements located well outside of the radar footprints, see subsection A.4. However, because these saildrone measurements are separated by hundreds of kilometres from the study area, they too should be treated with caution.

4.2.4 ECMWF

The European Centre for Medium-Range Weather Forecasting (ECMWF) provides validation for several atmospheric parameters. Included in the Sentinel-1 Ocean (S1 OCN) product are a wind field U_n and wind directions δ (with an RMSE of 30°) retrieved from a three-hourly ECMWF atmospheric model (Collecte Localisation Satellites, 2016) covering the same extent as the S1 scene. The ECMWF Reanalysis 5th Generation (ERA5) database provides gridded hourly data for several other parameters of interest. Their boundary layer height value is included in the results as a proxy measurement for Z_i. Further parameters retrieved include mean surface sensible and latent heat fluxes, H and E respectively, sea surface temperature T_{SST} and friction velocity u_*. Combining these with Equation 4.1 and Equation 4.2 yields an estimate of Obukhov length L using ECMWF data only. In turn, combining L with ERA5's Z_i and u_* in Equation 3.11 yields σ_u. Thus, the ECMWF provides validation for six atmospheric parameters, $\overline{U_n}$ and δ through the S1 OCN product and Z_i, u_*, σ_u and L through the ERA5 database. For clarity the data from both S1 OCN and ERA5 will be referred to as originating from the ECMWF in the results section.

ERA5's 0.25° by 0.25° horizontal resolution is too coarse to capture convection events. Instead the relevant parameters have been retrieved through parameterisation. For this reason the estimates retrieved through ERA5 should be treated with caution. ERA5 ensemble statistics are calculated for an area slightly greater than each S1 observation. The ERA5 footprints used for the Barbados scenes are provided in Table 6. On temporal scales the ERA5 data is selected to the closest hour of the S1 observation.

Table 6: ECMWF input footprint coordinates for ERA5 validation data. Barbados scenes.

	Jan 15th	Jan 27th A	Jan 27th B	Feb 1st	Feb 8th	Feb 20th
N	14.50	13.00	14.50	14.75	14.50	14.50
E	-54.50	-54.00	-54.25	-56.50	-54.25	-54.25
S	12.50	11.00	12.50	12.75	12.50	12.50
W	-57.25	-56.75	-57.00	-59.25	-57.00	-57.00

4.3 Miscellaneous data

A selection of miscellaneous scenes are analysed to provide insight into characterisation performance under a broader range of atmospheric circumstances. These are selected on their visually apparent convective features, see Figure A.2. Their geographical locations are presented in Figure 4.1 with overpass details provided in Table 7. Using the custom CNN all scenes were classified as containing three-dimensional cells, albeit to varying degrees. Thus, the processing approach for three-dimensional cells was followed.

Table 7: Metadata miscellaneous scenes.

Short name	Date	Path	Frame	Orbit	Mode	Polarisation	Abs. Orbit
Carolina	09-01-2020 22:49	33	105	Ascending	IW	VV	30730
Sea of Japan	17-01-2020 21:22	31	460	Descending	IW	VV	19862
Bering Sea	14-11-2019 05:05	168	188	Ascending	IW	VV	18919
Georgia	31-12-2019 23:13	77	97	Ascending	IW	VV	30599
Portugal	09-12-2019 18:50	16	115	Ascending	IW	VV	19292
Madeira	08-01-2020 18:50	16	103	Ascending	IW	VV	30713
Peru	22-10-2019 23:32	18	1122	Ascending	IW	VV	18594
Argentina	15-10-2019 09:09	170	734	Descending	IW	VV	29467

4.4 Miscellaneous data validation

For the miscellaneous scenes no field campaign data is available. Instead validation is performed using available ECMWF data, namely $\overline{U_n}$ and δ from the S1 OCN product and Z_i, u_*, σ_u and L from the ERA5 database, see subsubsection 4.2.4. The ERA5 footprints for the miscellaneous data are provided in Table 8. The S1 OCN footprints are identical to that of the S1 observation.

Table 8: ECMWF input footprint coordinates for ERA5 validation data. Miscellaneous scenes.

	Carolina	Sea of Japan	Bering Sea	Georgia	Portugal	Madeira	Peru	Argentina
N	34.75	40.75	59.25	32.25	37.75	34.00	-15.75	-41.25
E	-70.50	132.50	-168.50	-76.00	-11.25	-10.50	-74.25	-58.75
S	32.50	38.75	57.25	30.00	35.25	31.75	-18.25	-44.00
W	-73.75	128.50	-174.00	-79.50	-15.00	-14.00	-77.25	-63.00

Results and discussion

Results are presented for two datasets, namely the Barbados study area and several miscellaneous study areas. The results concerning the Barbados study area are presented in subsection 5.1 followed by results for the miscellaneous radar scenes in subsection 5.2. Characterisation results for the Barbados study area are obtained using algorithm 2B only. The observed stability ranges of the Barbados scenes fall outside the resolvable range for either algorithm 2A or 2C. For a single miscellaneous scene a comparison of the Obukhov length, L, results obtained with algorithms 2A, 2B and 2C are presented in Figure 5.5. The remaining miscellaneous results are obtained using algorithm 2B.

The inertial subrange normalised standard deviation threshold is set to 0.15, as discussed in subsubsection 3.5.3, resulting in the removal of tiles whose spectral slope did not follow a -5/3 power law. Results for the whole Sentinel-1 scene are presented as median ± median of absolute deviation (MAD) to decrease the sensitivity to outliers. For data following a Gaussian distribution the standard deviation σ is equal to 1.4862·MAD (Rousseeuw and Croux, 1993). An overview of results obtained for the Barbados and miscellaneous scenes is presented in Figure 5.1.

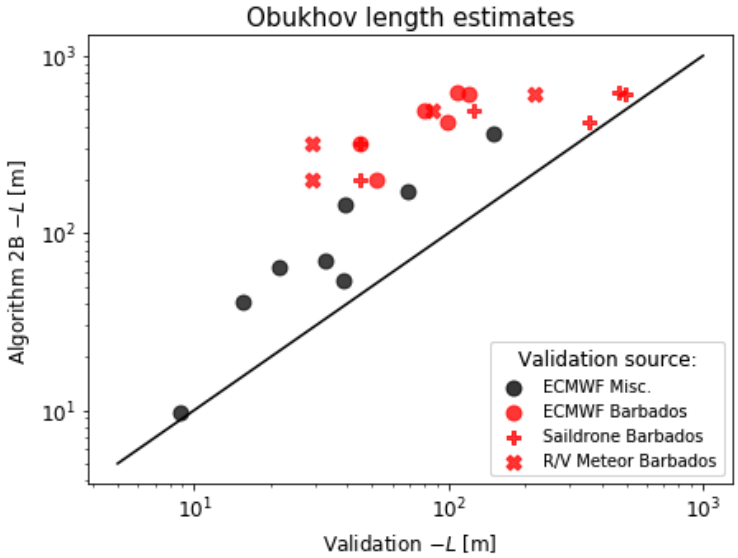

Figure 5.1: Median values of L estimated with scenario 2 of algorithm 2B using δ_{ECMWF}. Please note the Barbados results are presented up to three times, each compared to a different validation source.

5.1 Barbados

For the Barbados study area we focussed on the derivation of wind direction δ (180 degree ambiguity resolved) from subsection 3.2, CBL depth Z_i from subsection 3.4, friction velocity u_* and mean neutral wind speed $\overline{U_n}$ from algorithm 1A and horizontal wind standard deviation σ_u and Obukhov length L from algorithm 2B. A total of five scenarios are considered for each scene within this study area. Scenario 1 serves as a reference run. Its values were computed following the methodology of section 3. The remaining four scenarios test the characterisation sensitivity to various parameters, models and constants.

5.1.1 Scenario 1, 2 & 3: Reference and estimation sensitivity

Results are presented comparing reference scenario 1 to scenarios 2 and 3 and validation data. Scenario 2 uses the wind directions δ retrieved from ECMWF rather than those calculated following the steps in subsection 3.2. Since wind direction is estimated early in the methodology, see Figure 3.1, errors in its estimation propagate throughout all further calculations. Thus, by comparing scenario 1 and 2 one gains insight into the wind-direction estimation error as well as the propagated effect of this error on further estimates. In scenario 3 another source of uncertainty, the boundary layer height Z_i, is set using the in-situ collected data $Z_{i,\ RV}$. A comparison between scenarios 1, 2 and 3 gives insight into the error of manual Z_i estimation and its propagated effect on further estimates.

In Table 9 to Table 14 results for scenarios 1 to 3 are presented in combination with available validation data from the saildrone (SD), R/V Meteor (R/V) and the ECMWF. Each table shows δ, Z_i, $\overline{U_n}$, u_*, σ_u and L. Included for each scenario are the fraction of tiles used in analysis. Missing tiles were filtered out due to not meeting the thresholds set in subsection 3.3 and subsection 3.5, i.e. a fraction closer to 1 is better. Data in **bold** indicates a predetermined value, i.e. **bold** values for δ and Z_i indicate δ_{ECMWF} and $Z_{i,\ RV}$ respectively. In Figure 5.2 the spatial distribution of L estimates is plotted for a single scene using scenario 2. The spatial distributions for all scenes are presented in Figure A.10.

Table 9: Scenarios January 15th. Convection classified as two-dimensional rolls. Lack of $Z_{i,\ RV}$ measurement prevents the calculation of scenario 3 and $\sigma_{u,\ SD}$.

	Scenario 1	Scenario 2	Scenario 3	SD	R/V	ECMWF
Tiles	52/60	59/60	-	-	-	-
δ	62.1 ± 26.5	**78.3 ± 2.4**	-	-	-	78.3 ± 2.4
Z_i	1095 ± 269	956 ± 243	-	-	-	1102 ± 52
$\overline{U_n}$	10.9 ± 1.1	9.1 ± 0.3	-	-	-	9.0 ± 0.3
u_*	0.399 ± 0.047	0.323 ± 0.012	-	0.37 ± 0.01	-	0.34 ± 0.01
σ_u	0.885 ± 0.098	0.718 ± 0.027	-	-	-	0.88 ± 0.02
L	-561 ± 170	-585 ± 123	-	-469 ± 52	-	-109 ± 4

Table 10: Scenarios January 27th A. Convection classified as three-dimensional cells. Please note: the R/V Meteor was located outside S1 footprint on the other side of an atmospheric front while the saildrone was located well outside S1 footprint.

	Scenario 1	Scenario 2	Scenario 3	SD	R/V	ECMWF
Tiles	57/60	60/60	59/60	-	-	-
δ	112.1 ± 28.9	**79.5 ± 5.3**	**79.5 ± 5.3**	-	-	79.5 ± 5.3
Z_i	939 ± 142	969 ± 112	**500**	**500**	500	713 ± 53
$\overline{U_n}$	6.4 ± 0.5	5.9 ± 0.1	5.9 ± 0.1	-	-	5.9 ± 0.1
u_*	0.211 ± 0.019	0.192 ± 0.004	0.192 ± 0.004	0.13 ± 0.00	0.16 ± 0.01	0.22 ± 0.01
σ_u	0.504 ± 0.035	0.460 ± 0.007	0.433 ± 0.008	0.33 ± 0.01	0.47 ± 0.01	0.58 ± 0.02
L	-194 ± 38	-202 ± 26	-213 ± 36	-45 ± 5	-30 ± 8	-52 ± 5

Table 11: Scenarios January 27th B. Convection classified as two-dimensional rolls. Please note: the R/V Meteor was located outside S1 footprint on the other side of an atmospheric front while the saildrone was located well outside S1 footprint.

	Scenario 1	Scenario 2	Scenario 3	SD	R/V	ECMWF
Tiles	51/60	51/60	52/60	-	-	-
δ	111.6 ± 8.1	**94.8 ± 2.0**	**94.8 ± 2.0**	-	-	94.8 ± 2.0
Z_i	662 ± 145	647 ± 142	**500**	**500**	500	704 ± 59
$\overline{U_n}$	6.8 ± 0.4	5.9 ± 0.3	5.9 ± 0.2	-	-	5.8 ± 0.3
u_*	0.224 ± 0.018	0.193 ± 0.010	0.194 ± 0.009	0.13 ± 0.00	0.16 ± 0.01	0.21 ± 0.01
σ_u	0.504 ± 0.037	0.433 ± 0.022	0.433 ± 0.008	0.33 ± 0.01	0.47 ± 0.01	0.57 ± 0.03
L	-372 ± 94	-323 ± 71	-302 ± 62	-45 ± 5	-30 ± 8	-45 ± 4

Table 12: Scenarios February 1st. Convection classified as two-dimensional rolls. Please note: the saildrone was located well outside S1 footprint.

	Scenario 1	Scenario 2	Scenario 3	SD	R/V	ECMWF
Tiles	53/60	60/60	60/60	-	-	-
δ	75.2 ± 28.3	**82.8 ± 1.5**	**82.8 ± 1.5**	-	-	82.8 ± 1.5
Z_i	869 ± 251	657 ± 164	**650**	**650**	650	839 ± 34
$\overline{U_n}$	8.6 ± 0.9	7.2 ± 0.2	7.3 ± 0.2	-	-	7.3 ± 0.2
u_*	0.301 ± 0.038	0.246 ± 0.007	0.246 ± 0.007	0.22 ± 0.01	0.27 ± 0.01	0.27 ± 0.01
σ_u	0.655 ± 0.07	0.541 ± 0.015	0.537 ± 0.013	0.52 ± 0.02	0.68 ± 0.01	0.72 ± 0.01
L	-550 ± 157	-476 ± 88	-454 ± 86	-127 ± 12	-87 ± 5	-80 ± 3

Table 13: Scenarios February 8th. Convection classified as two-dimensional rolls. Please note: the R/V Meteor was located just outside S1 footprint.

	Scenario 1	Scenario 2	Scenario 3	SD	R/V	ECMWF
Tiles	59/60	58/60	59/60	-	-	-
δ	76.9 ± 4.8	**77.4 ± 2.1**	**77.4 ± 2.1**	-	-	77.4 ± 2.1
Z_i	815 ± 231	842 ± 249	**850**	**850**	850	1061 ± 213
$\overline{U_n}$	10.3 ± 0.3	9.4 ± 0.3	9.3 ± 0.4	-	-	9.3 ± 0.3
u_*	0.374 ± 0.014	0.333 ± 0.012	0.334 ± 0.012	0.35 ± 0.02	0.36 ± 0.02	0.35 ± 0.01
σ_u	0.823 ± 0.031	0.726 ± 0.024	0.730 ± 0.026	0.77 ± 0.04	0.83 ± 0.03	0.89 ± 0.03
L	-515 ± 105	-568 ± 105	-572 ± 108	-495 ± 51	-219 ± 75	-120 ± 18

Table 14: Scenarios February 20th. Convection classified as two-dimensional rolls. Please note: only a single measurement available from the R/V Meteor for $Z_{i,\ RV}$. Scene suffers from several local inhomogeneities, see Figure A.1.

	Scenario 1	Scenario 2	Scenario 3	SD	R/V	ECMWF
Tiles	44/60	50/60	52/60	-	-	-
δ	23.9 ± 10.4	**59.4 ± 1.0**	**59.4 ± 1.0**	-	-	59.4 ± 1.0
Z_i	1236 ± 207	996 ± 235	**800**	**800**	800	991 ± 27
$\overline{U_n}$	12.6 ± 1.3	8.7 ± 0.3	8.8 ± 0.4	-	-	8.7 ± 0.2
u_*	0.479 ± 0.060	0.307 ± 0.011	0.307 ± 0.011	0.30 ± 0.04	-	0.32 ± 0.02
σ_u	1.102 ± 0.129	0.692 ± 0.029	0.683 ± 0.024	0.69 ± 0.07	-	0.85 ± 0.03
L	-453 ± 101	-425 ± 57	-403 ± 41	-358 ± 138	-	-88 ± 11

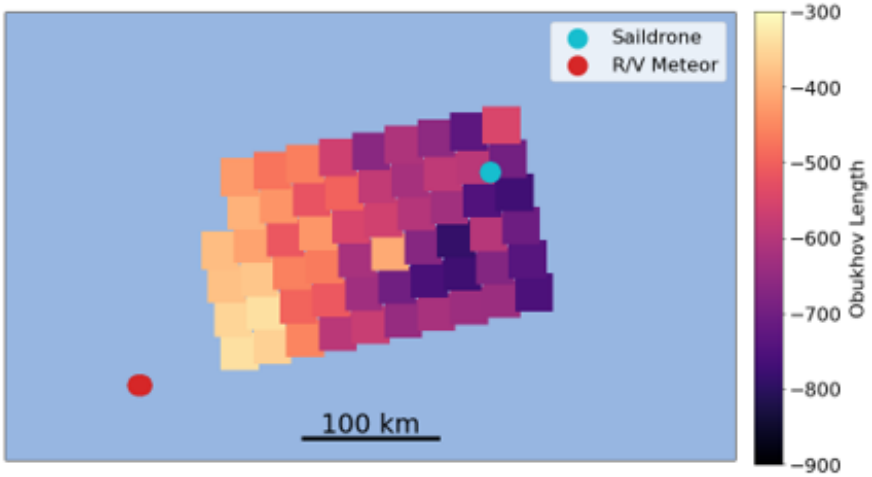

Figure 5.2: Spatial overview of Scenario 2 Obukhov Length L results for February 8th.

5.1.1.1 Wind direction The median wind directions, δ, of scenario 1 differ with those retrieved from ECMWF (RMSE is 18.2°). The wind directions of scenario 1 are offset in both directions with respect to δ_{ECMWF}. For scene February 20th the difference is greatest at over 35° whereas for scene February 8th the difference is less than 1°. The scenario 1 uncertainties (expressed as the MAD) are up to an order of magnitude greater than those from δ_{ECMWF}. For all scenes but February 20th the δ_{ECMWF} values fall within the MAD range of the δ estimates.

As is illustrated by scenario 1 and 2, the wind-direction estimation affects all subsequent parameters, albeit to varying degrees. When using δ_{ECMWF}, the quantity of tiles increases for all scenes but February 8th—whose δ already aligned with δ_{ECMWF}—meaning more tiles meet the thresholds set in subsection 3.3 and subsection 3.5. For all scenes the neutral wind speed $\overline{U_n}$ decreases, which simultaneously decreases u_* and σ_u. These new scenario 2 estimates of $\overline{U_n}$, u_* and σ_u are closer to the validation data than those from scenario 1. Similarly, on average the estimates of Z_i approach $Z_{i,\ RV}$ when using δ_{ECMWF}; the RMSE of Z_i estimates with respect to $Z_{i,\ RV}$ decreases from 258 m for scenario 1 to 165 m for scenario 2. There is little difference between the scenario 1 and 2 estimates for L because, despite affecting both u_* and σ_u by up to several tens of percents (see February 20th), the ratio σ_u/u_* stays approximately the same (the RMSE between the two is 1.0% of the average ratio). For scenes with relatively large uncertainty, such as

January 15th and February 1st, the respective uncertainty for $\overline{U_n}$, u_* and σ_u decreases by a factor ~4 or more in scenario 2. This suggests at least part of their scatter originates from scatter in wind-direction estimation.

A possible explanation for the difference between δ and δ_{ECMWF} is the bias between true wind direction and the direction of greatest variability for two-dimensional rolls. A 20° bias is used to account for rolls being orientated between the surface wind direction and the geostrophic wind direction (see subsubsection 2.1.2). However, based on the observed bias ranges in Figure 3 of Wang et al. (2019a), the introduced constant bias of 20° may still be off by tens of degrees. A second source of difference between δ and δ_{ECMWF} relates to the variations in convective structures. For instance, the scene February 1st was assumed to contain two-dimensional rolls yet the histogram of estimated wind directions displays a secondary distribution at approximately 90° offset with respect to the main distribution, see Figure 5.3. The effect of this secondary δ distribution visibly carries over in the distributions of u_*, $\overline{U_n}$ and σ_u. This indicates that a processing approach for rolls was erroneously applied on a tile dominated by cells, i.e. misclassification of tiles.

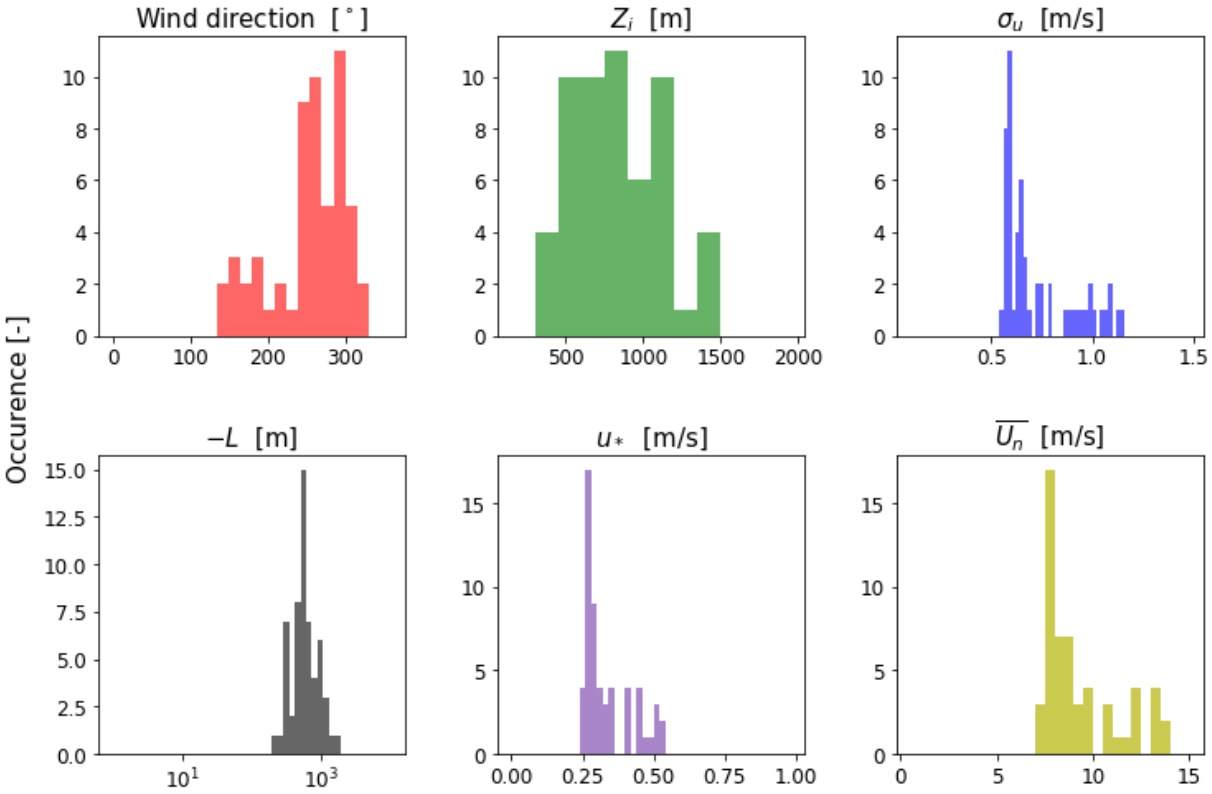

Figure 5.3: Scenario 1 results for February 1st, wind direction histogram not yet corrected for 180° ambiguity.

If one desires to precisely and consistently estimate wind direction using only the orientation of features within radar imagery, such as rolls or cells, a suitable method should be found capable of deriving the offset between surface-wind direction and the orientation of features rather than selecting a constant bias (such as 20° for rolls) to account for a stochastic offset. This is especially the case if interested in only σ_u or u_* as changes in wind direction can affect these parameters by up to several tens of percents (e.g. scene February 20th). Additionally, each tile should be classified separately and processed accordingly, rather than

processing each tile according to the most dominant convection mode of the whole scene (as was done in this study). The former approach was was not selected for this study because, due to the immaturity of our classification algorithm, it inadvertently increased the scatter of results. Even on the scale of an individual tile convective structures can contain both cells and rolls (e.g. Zecchetto and De Biasio, 2002), complicating classification. For such scenarios one could apply a filter to remove tiles for which the classification certainty falls below a certain threshold. Neither was this performed in our study due to the aforementioned limitations of our classification algorithm.

5.1.1.2 Convective Boundary Layer depth Scenario 1 estimates of Convective Boundary Layer (CBL) depth Z_i are consistently overestimated with respect to the in-situ boundary layer depth $Z_{i,\ RV}$. The largest discrepancies are observed for scenes January 27th A and February 20th, for which the difference exceeds 400 m. Only for scenes February 1st and February 8th the difference is within the uncertainty (MAD). Using δ_{ECMWF} improves the estimation of Z_i; The RMSE of Z_i estimates for scenario 1 and 2 with respect to $Z_{i,\ RV}$ are 258 m and 165 m respectively. This observation can be substantiated by theory: power in the two-dimensional spectrum will project itself onto longer wavelengths in the one-dimensional spectrum if not directly on the axis of analysis, thus leading to overestimation of Z_i when using an incorrect δ. The $Z_{i,\ \text{ECMWF}}$ values have an RMSE of 201 ms^{-1} with respect to $Z_{i,\ RV}$. However, their difference is so consistent that the coefficient of determination between $Z_{i,\ \text{ECMWF}}$ and $Z_{i,\ RV}$ is $\text{R}^2 = 0.996$, compared to a mere $\text{R}^2 = 0.010$ for scenario 2's Z_i and $Z_{i,\ RV}$.

The effect of errors in the Z_i estimation are negligible for further estimation of u_*, σ_u and L. Even for scene January 27th A—whose Z_i estimate is almost twice as high as $Z_{i,\ RV}$—scenario 2 and 3 estimates of L differ by only $\sim$5%. However, these results were obtained using algorithm 2B, which is mostly independent of Z_i (see Equation 3.21). When using algorithm 2A the errors in Z_i estimates would propagate as linear errors in the estimation of L following the linear dependence of L and Z_i in Equation 3.11. For January 27th A that could lead to a factor $\sim$2 overestimation of $-L$.

Errors in Z_i estimation could originate from the stochastic nature of aspect ratios. This study assumes a constant aspect ratio of 1.5 and 2 for three-dimensional cells and two-dimensional rolls respectively. For the latter Wang et al. (2019a) shows aspect ratios ranging between 0.5 and 10 (with a mean and standard deviation of 3.39 ± 1.79). Since aspect ratios are inverse linearly proportional to Z_i, see subsection 3.4, an aspect ratio of 4 would be sufficient to cause underestimation of Z_i for all scenes rather than the currently observed overestimation. In other words, results for Z_i are malleable depending on which aspect ratio is chosen, especially considering the range of plausible aspect ratios. Thus, in order to improve the estimation of Z_i, the aspect ratios should be derived for each scene rather than chosen from a stochastic distribution.

One cause of consistent Z_i overestimation to be excluded is that of elongation of cells in the along-wind direction. For five out of six study areas in the Barbados region the analysis was performed in the across-wind direction due to the roll-like alignment of convection. Thus in five out of six cases along-wind elongation could not have been a factor. Naturally the one scene with three-dimensional cells, namely January 27th A, could still suffer from elongation and subsequent Z_i overestimation.

The different dependencies of algorithms 2A, 2B and 2C on Z_i present an opportunity to estimate Z_i. For this one needs an accurate PSD and estimate of u_* from which both a filtered σ_u (using algorithm 2A) and L

(using either algorithm 2B or 2C) can be derived. Then by iterating different inputs of Z_i into Equation 3.11 from algorithm 2A, one can determine the true value of Z_i as the value which yields the same L as the L calculated in algorithm 2B or 2C independent of Z_i. This by-basses the need to calculate Z_i following the method of Sikora et al. (1997) and its inherent uncertainties related to the aspect ratio. For this to become feasible the limitations and uncertainties of algorithms 2A and 2B or 2C need to be resolved first.

5.1.1.3 Wind speed and friction velocity Scenario 1 results for $\overline{U_n}$ and u_* are consistently overestimated with respect to the validation results. Using the wind directions from ECMWF, δ_{ECMWF}, improves the estimation of both parameters. Compared to ECMWF data, the RMSE of scenario 1 estimates for $\overline{U_n}$ decreases from 1.6 ms^{-1} to < 0.1 ms^{-1} for scenario 2. Similarly, the coefficient of determination for the u_* values of scenario 1 and ECMWF is $R^2 = 0.766$ whereas that of scenario 2 and ECMWF is $R^2 = 0.995$ (both only for six scenes). A similar comparison between results from scenario 1 and 2 with the saildrone yields R^2=0.738 and R^2=0.980, respectively. Excluding the January 27th scenes (which self correlate and experience unfavourable validation platform locations, see subsubsection 4.2.3) the estimates of u_* from scenario 2 are within a few percent of validation. Compared to the saildrone, R/V Meteor and ECMWF validations data, the scenario 2 estimates of u_* are spread with the mean difference being 0.02, 0.00 and -0.02 ms^{-1}, respectively. Using a two-tailed paired t-test, the differences between scenario 2 estimates and saildrone or R/V Meteor validation is insignificant ($p > 50\%$). However, the difference with respect to ECMWF data is significant ($p < 0.1\%$).

5.1.1.4 Horizontal wind standard deviation Estimates for horizontal wind standard deviation σ_u improve when using δ_{ECMWF}. The coefficient of determination for σ_u's between scenario 1 and the saildrone, R/V Meteor and ECMWF is $R^2 = 0.720$, 0.988 and 0.765 respectively. A similar analysis using σ_u's from scenario 2 yields $R^2 = 0.982$, 0.930 and 0.987. Only four σ_u data points are retrieved from the R/V Meteor of which two for January 27th, which use identical validation data retrieved from unfavourable validation platform locations (see subsubsection 4.2.3). This could result in the high correlation observed for the R/V Meteor. The mean σ_u difference between scenario 2 and the validations platforms is 0.04, -0.07 and -0.15 ms^{-1} for the saildrone, R/V Meteor and the ECMWF respectively. Similar to u_* results, using a two-tailed paired t-test, the differences between scenario 2 estimates of σ_u with respect to saildrone or R/V Meteor validation are insignificant ($p < 50\%$ and $p < 20\%$ respectively) whereas the difference between scenario 2 estimates and ECMWF validation is significant ($p < 0.1\%$).

5.1.1.5 Obukhov Length Obukhov length L is used to indicate an atmospheric stability where the (in)stability is calculated as zL^{-1} (z being the measurement height of 10 m). For negative L's the atmosphere is considered unstable with values closer to zero indicating greater instability. Estimates of $|L|$ are consistently overestimated with respect to validation, leading to a smaller $|zL^{-1}|$ and thus underestimation of the atmospheric instability. The coefficient of determination increases when external inputs for δ and Z_i are used (scenario 2 and 3 respectively) with respect to all three validation sources. The greatest performance increase occurs from scenario 1 to scenario 2.

The overestimation of L is caused by underestimation of σ_u and or overestimation of u_*. Since $-L \propto (\sigma_u/u_*)^{-3}$, see Equation 3.11, minor relative differences in the ratio σ_u/u_* can greatly affect the Obukhov length estimate. The mean difference between this ratio from scenario 2 with respect to the saildrone,

R/V Meteor and ECMWF is -0.12, -0.42 and -0.38, respectively. Using a one-tailed paired t-test (instead of two-tailed because the mean difference in average ratios is negative for all), the differences between the ratios obtained through scenario 2 and the saildrone, R/V Meteor and ECMWF are statistically significant ($p < 5.0\%$, $p < 5.0\%$ and $p < 0.1\%$ respectively).

5.1.2 Scenario 4: GMF intercomparison

Scenario 4 compares results obtained using CMOD5.N (reference) with those obtained with CMOD-IFR2. Both GMFs were used following scenario 2, i.e. using wind direction δ_{ECMWF}. Alternatively one could use scenario 3 but then one cannot determine the influence on Z_i estimation. Furthermore, only five scenario 3 results are available versus six of scenario 2. Parameters affected by the GMF are included in Table 15.

Table 15: Comparison of CMOD5.N with CMOD-IFR2 using δ_{ECMWF}.

	Jan 15th		Jan 27th A		Jan 27th B	
CMOD	5.N	IFR2	5.N	IFR2	5.N	IFR2
Z_i	956 ± 243	926 ± 243	969 ± 112	969 ± 112	647 ± 142	657 ± 162
$\overline{U_n}$	9.1 ± 0.3	8.7 ± 0.4	5.9 ± 0.1	4.9 ± 0.1	5.9 ± 0.3	5.0 ± 0.3
u_*	0.323 ± 0.012	0.303 ± 0.016	0.192 ± 0.004	0.158 ± 0.005	0.193 ± 0.010	0.161 ± 0.011
σ_u	0.718 ± 0.027	0.706 ± 0.028	0.460 ± 0.007	0.410 ± 0.010	0.433 ± 0.022	0.382 ± 0.025
L	-585 ± 123	-297 ± 77	-202 ± 26	-109.4 ± 16.5	-323 ± 71	-164 ± 28
	Feb 1st		Feb 8th		Feb 20th	
CMOD	5.N	IFR2	5.N	IFR2	5.N	IFR2
Z_i	657 ± 164	635 ± 162	842 ± 249	815 ± 241	996 ± 235	996 ± 235
$\overline{U_n}$	7.2 ± 0.2	6.5 ± 0.2	9.4 ± 0.3	8.9 ± 0.4	8.7 ± 0.3	8.1 ± 0.3
u_*	0.246 ± 0.007	0.216 ± 0.009	0.333 ± 0.012	0.316 ± 0.015	0.307 ± 0.011	0.282 ± 0.012
σ_u	0.541 ± 0.015	0.495 ± 0.022	0.726 ± 0.024	0.710 ± 0.030	0.692 ± 0.029	0.669 ± 0.031
L	-476 ± 88	-210 ± 47	-568 ± 105	-316 ± 68	-425 ± 57	-216 ± 30

Compared to $\overline{U_n}$ retrieved from ECMWF, the CMOD5.N and CMOD-IFR2 estimated wind speeds have an RMSE of < 0.1 ms^{-1} and 0.7 ms^{-1} respectively. Results from scenario 4 illustrate the impact of a minor bias in the estimates of u_*. Compared to CMOD5.N, CMOD-IFR2 yields lower wind-speed estimates which results in lower values of u_*. The decrease in u_* affects the estimated Obukhov length by up to a factor 2 despite being partially counteracted by a decrease in σ_u. Thus, for an accurate estimate of L it is crucial to retrieve accurate values of both u_* and σ_u. An error of no more than 10% in either parameter is sufficient to hinder the estimation process. Using CMOD5.N, the estimated values of $\overline{U_n}$ and u_* are in line with those retrieved from validation for all scenes but those on the 27th of January. Thus, despite not experiencing consistent $|L|$ overestimation, CMOD-IFR2 accomplishes this through tweaking the "wrong" parameter.

5.1.3 Scenario 5: Sensitivity to constants

Several constants and parameters of the scenario 1 reference run are varied within spread found in literature to determine the L estimation sensitivity, see Figure 5.4.

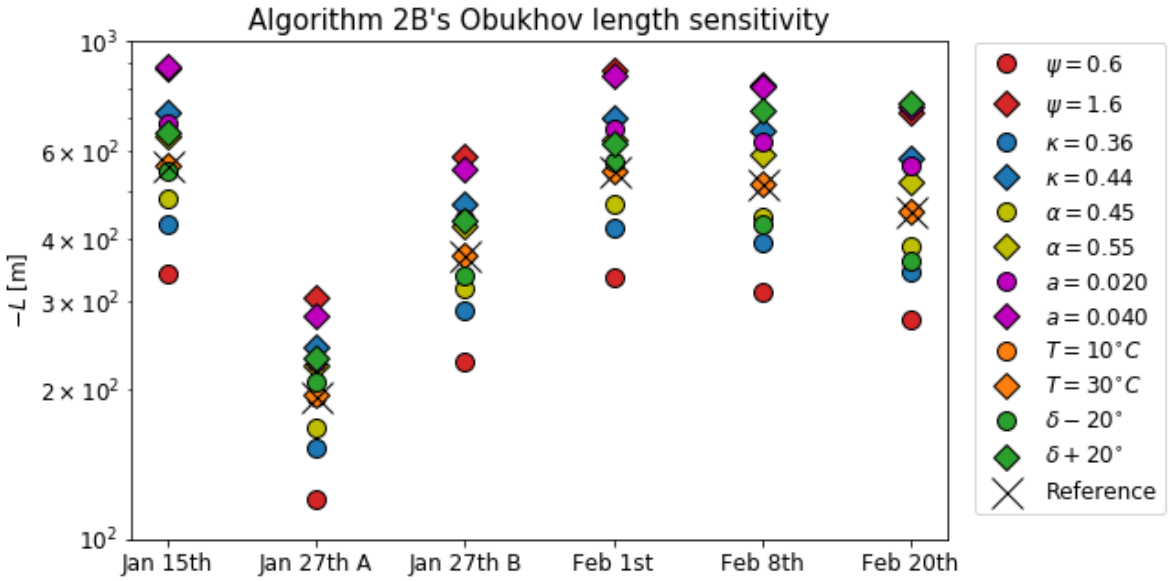

Figure 5.4: Algorithm 2B reference run used: $\psi = 1$, $\kappa = 0.4$, $\alpha = 0.5$, $a = 0.011$, $T = 20°$ and $\delta = \delta_{\text{scenario 1}}$.

Results of scenario 5 display the importance of correct constants and variables. The choice of dimensionless energy dissipation rate ψ introduces significant uncertainty to algorithm 2B. The natural spread of near-surface values for ψ (as per Figure 4 in Kaimal et al. (1976)) combined with the inverse dependence of $|L|$ on ψ can easily cause a factor 2 over- or underestimation. A 10% change in either κ or α propagates as a ∼25% change in $|L|$. However, frequently cited alternative values for κ or α tend to be within 5% of the reference values used for algorithm 2B rather than 10%. Furthermore, in practise the sensitivity to spread in κ is less than may appear from Figure 5.4 as the equations selected for this study were fine-tuned to $\kappa = 0.40$. Should the true value of κ be found to differ from 0.40, the empirical equations would cancel out most of the introduced error. The chosen value of 0.011 for a is suitable for oceans with swell (Hersbach, 2011). Should larger values of a be selected corresponding to a typical ocean, $a \approx 0.020$, or young ocean, $a \approx 0.040$ (Hersbach, 2011), the resulting estimates of $|L|$ would be up to 50% greater. Compared to the other variables, the choice of temperature has a negligible influence on $|L|$ estimation. The sensitivity to errors in wind-direction estimation differs from scene-to-scene. For February 1st the effect is minor whereas for February 20th it is almost as great as the sensitivity to ψ. The variable sensitivity could be caused by the uncertainty in the initial wind-direction estimates (see paragraph 5.1.1.1) and or a non-linear relation between wind direction and Obukhov length.

Considering that favourably low values are chosen for a, α and ψ, that offsets in δ can cause both under- and overestimation of $|L|$ rather than the observed overestimation only and that temperature changes have negligible influence on $|L|$, it is assumed that the aforementioned parameters can be excluded as likely sources of consistent $|L|$ overestimation. From the considered constants and parameters only κ can be a consistent source of $|L|$ underestimation, although the observed overestimation of $|L|$ is too large to be explained by a lower value of κ alone. Thus, the observed consistent overestimation of $|L|$ likely requires other contributing sources.

5.1.4 Currents and swell

Surface currents change the observed surface-stress field. For the Barbados region the mean surface-current vector is approximately aligned with the wind direction, as discussed in subsection 4.2. Thus, if present, surface currents could lead to a (minor) underestimation of $\overline{U_n}$ and u_* and therefore underestimation of $|L|$. Since the opposite is observed, it means currents would lead to a decrease of the observed Obukhov length overestimation. Scenario 4 results display the effect of a minor change in $\overline{U_n}$ on the estimation of u_* and L. Surface currents need only alter the observed velocity field by a few percent to achieve similar results. Since surface currents introduce a bias to $\overline{U_n}$ they are expected to influence low-wind scenarios relatively more.

Long-wavelength swell might affect the results of this study. Though a Charnock constant was chosen which, according to Hersbach (2011), is representative of oceans with swell, this does not fully account for the influence swell may have on characterisation. A review of Figure 10 in Drennan et al. (1999) indicates a significant swell-induced variability in drag coefficients for $U < 5$ ms^{-1}. A Charnock value between $0.010 < a < 0.040$ is unable to account for such variability. Furthermore, according to the aforementioned figure, the effect of swell is orientation dependent meaning that a Charnock constant should be chosen based on the magnitude and orientation of swell, rather than the former only. From Equation 3.8 it follows that a change in C_d affects u_* and since $L \propto -u_*^3$ (Equation 2.1), the effect of swell on u_* can significantly affect the estimation of L.

When using 50 m pixels instead of 300 m ones, two-dimensional spectra for all Barbados scenes contain spectral peaks at spatial wavelengths shorter than 300 m (not shown). These fall within the common $\mathcal{O}(100$ m) range of swell wavelengths (e.g. Vachon et al., 2004; Toffoli and Bitner-Gregersen, 2017). However, the estimated u_* values differ insignificantly with those retrieved from the saildrone or R/V Meteor and for all scenes but those from January 27th, the estimated values of u_* fall within a few percent of those retrieved from validation data. This implies swell did not significantly alter the expected parameter. Furthermore, according to Figures 9 and 10 from Donelan et al. (1997) and Drennan et al. (1999) respectively, swell can lead to over- or underestimation of C_d—and thus $|L|$—depending on the orientation of swell with respect to the wind direction. This study observes consistent overestimation only, which further supports the hypothesis that swell did not decisively contribute to the observed consistent $|L|$ overestimation. However, At only six observation for the Barbados region, statistical confidence is lacking. Additional data is required in order to determine the variable effect swell may induce on characterisation and to test whether ignoring that part of the two-dimensional spectrum containing swell signatures (e.g. by filtering spatial wavelengths < 300 m as performed in this study) is correct.

5.2 Miscellaneous scenes

Results are presented for several miscellaneous study areas. These scenes cover a wider range of atmospheric settings than those of Barbados and thus allow for usage of algorithms 2A and 2C. Additionally, the increased number of scenes allows for conclusions to be drawn based on statistical significance.

By combining algorithms 2A, 2B and 2C for the Carolina study area it is shown how to estimate ψ and the necessary wind-field slope multiplier to arrive at ECMWF's estimate of L_{ECMWF}. Applying a slope

multiplier involves the subtraction of the mean wind speed and the multiplication of the residuals followed by the readdition of the mean. This artificially increases the wind-field variance at all assessed spatial wavelengths. First a scenario 3 run of algorithms 2A, 2B and 2C is performed using a predetermined $Z_{i\ \mathrm{ECMWF}}$ and δ_{ECMWF} in combination with a slope multiplier of 1 (i.e. no multiplication) and $\psi = 1$, see Figure 5.5a. Algorithm 2A's and 2B's estimates of $|L|$ are greater than $|L_{\mathrm{ECMWF}}| = 15.5$ m, which implies underestimation of the wind-field variance. Additionally, algorithm 2A's estimates of $|L|$ are greater than that of algorithm 2B despite no spectral filtering being applied in algorithm 2A. For such an approach algorithm 2A should always yield lesser $|L|$ values than algorithm 2B. By multiplying the wind-field slope by a factor 1.7 the observed stability range allows for usage of algorithm 2C. For said slope multiplication algorithm 2C yields a median value of $|L| = 15.5$ m, algorithm 2B yields $|L| = 11.0$ m and algorithm 2A yields lesser values still. Algorithm 2A's values can be explained by the aforementioned lack of spectral filtering. Algorithm 2B's values should be identical to that of algorithm 2C. By increasing ψ from 1.0 to 1.6 the median results for algorithms 2B and 2C match. Thus, if we can assume $|L_{\mathrm{ECMWF}}| = 15.5$ m is correct, a slope multiplication of approximately 1.7 is necessary to arrive at L_{ECMWF} using algorithm 2C, which in turn requires ψ to be 1.6 for algorithm 2B to approximately align with algorithm 2C.

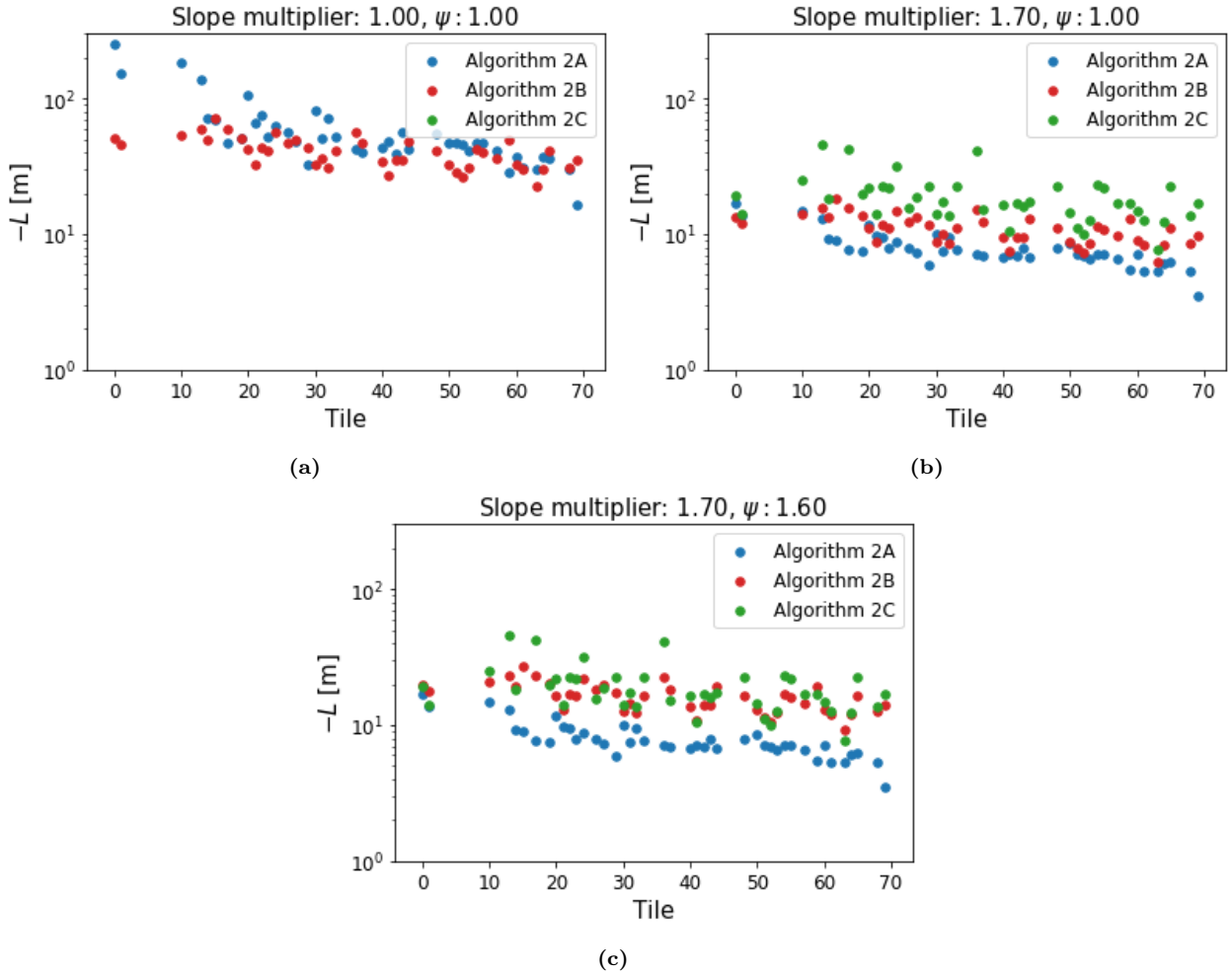

Figure 5.5: Iterative approach to arrive at estimated values for wind-field slope multiplication factor and ψ.

Results for a similar process applied on the Sea of Japan and Argentina study areas are presented in Table 16. The $|L_{\text{ECMWF}}|$ values for the remaining study areas are either too large or too small for algorithm 2C to be applied. A multiplication of the wind-field slope is required in order to align algorithm 2B's and 2C's results with that of the ECMWF. This discrepancy exist for all scenes, see data points validated with ECMWF in Figure 5.1, suggesting that either ECMWF or algorithm 2B suffers from a bias.

Table 16: Median values of L retrieved from ECMWF and a scenario 3 version of algorithm 2B. Where available the slope multiplier and deduced ψ are given to align algorithms 2B and 2C with L_{ECMWF}.

	L_{ECMWF}	L	Required slope multiplier	Deduced ψ
Carolina	-15.5	-41.1	1.7	1.6
Sea of Japan	-21.6	-63.6	1.8	1.7
Bering Sea	-149.6	-365.0	-	-
Georgia	-39.4	-145.1	-	-
Portugal	-38.5	-53.7	-	-
Madeira	-69.3	-170.8	-	-
Peru	-8.8	-9.8	-	-
Argentina	-33.0	-70.1	1.7	1.9

For all fourteen scenes (six from Barbados and eight miscellaneous) the scenario 3 results for $\overline{U_n}$, u_*, σ_u and σ_u/u_* are presented in Figure 5.6. The Barbados results differ slightly from those presented prior as here $Z_{i\ \text{ECMWF}}$ was used rather than $Z_{i\ RV}$.

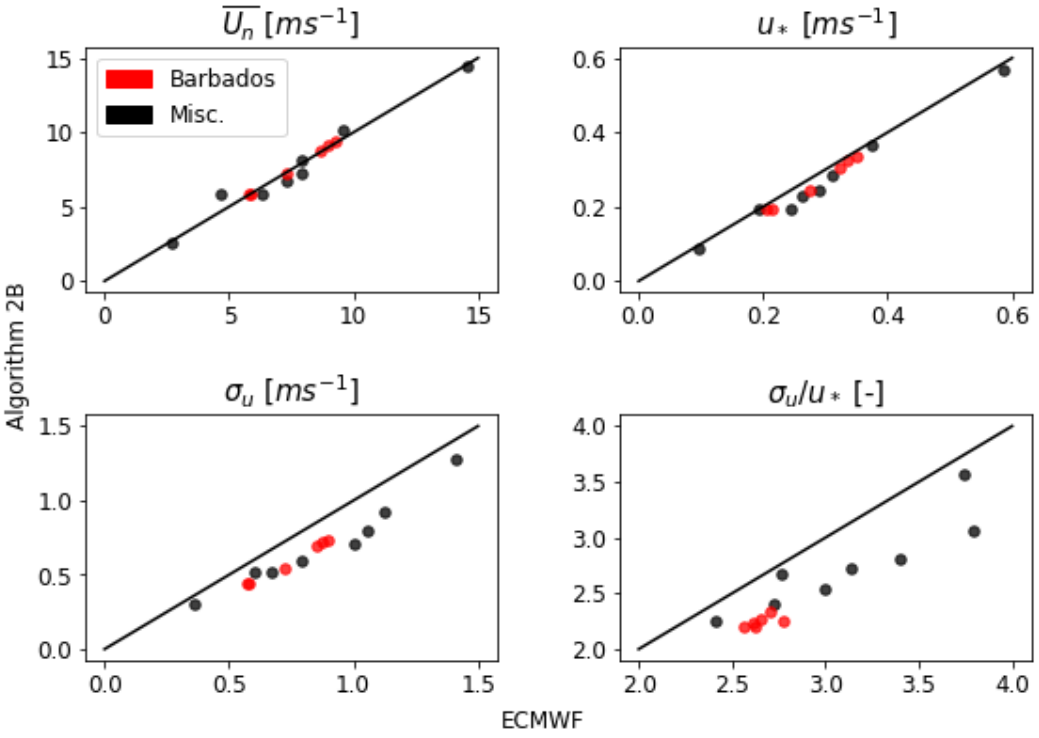

Figure 5.6: Median values of $\overline{U_n}$, u_* and σ_u estimated with scenario 3 of algorithm 2B using CMOD5.N, δ_{ECMWF} and $Z_{i\ \text{ECMWF}}$.

The RMSE of wind-speed estimates for all fourteen scenes with respect to ECMWF validation is 0.3 ms^{-1}, increasing to 0.8 ms^{-1} when using CMOD-IFR2 (not shown) over CMOD5.N (Figure 5.6). According to a two-tailed paired t-test, the difference between CMOD-IFR2 estimates and ECMWF validation is statistically significant ($p < 0.1\%$) whereas that been CMOD5.N and ECMWF is not ($p > 50\%$). Results from Figure 5.6 show that all ECMWF's median values for u_* are greater than those calculated using algorithm 2B despite no significant bias existing for average neutral wind speed $\overline{U_n}$. This can be explained by the choice of a favourably low Charnock constant a which decreases algorithm 2B's estimate of u_*. On average ECMWF's u_* values are 0.02 ms^{-1} larger than those estimated through algorithm 2B. From Equation 3.11 it follows that a greater u_* leads to a lesser σ_u/u_* and thus a greater $|L|$. However, ECMWF's values for σ_u are sufficiently large (on average 0.16 ms^{-1} larger than those from algorithm 2B), that despite the increased u_*'s, its ratio for σ_u/u_* exceeds that retrieved using algorithm 2B. On average for all fourteen study areas, the ECMWF ratio for σ_u/u_* is 15% greater than that calculated through algorithm 2B (i.e. algorithm 2B underestimates σ_u/u_* by 13%). Since $|L| \propto (\sigma_u/u_*)^{-3}$, see Equation 3.11, the ECMWF values for $|L|$ are a third smaller than those from algorithm 2B. Thus, underestimation of algorithm 2B's wind-field variance (with respect to that retrieved from ECMWF) leads to an average 50% overestimation of $|L|$. Algorithm 2B's consistent underestimation of σ_u, u_* and σ_u/u_* are all three statistically significant with $p < 0.05\%$ (using a one-tailed paired t-test).

5.3 Overview

Successful implementation of algorithm 2A, and to a lesser degree algorithms 2B and 2C, requires improved estimation of Z_i. In turn this requires a better understanding of the aspect ratios associated with rolls and cells with respect to Z_i. Ideally these aspect ratios would be derivable rather than setting them to a constant. Currently algorithm 2A is also impeded by asymptotes in its equations. This prevents use in cases such as the Barbados study area with high absolute Obukhov lengths. Lastly, algorithm 2A requires spectral filtering to retrieve σ_u from the spectrum directly. This requires a clear +1 power law leading up to a spectral peak from which to extrapolate. In the absence of a clear spectral peak (such as the case for most scenes of this study, see Figure A.11 for examples) the +1 power-law extrapolation becomes an art rather than a science. This yields malleable results due to the cubed dependence of $|L|$ on σ_u.

Algorithm 2B is impeded by uncertainties relating to near-surface values of ψ although its consistent overestimation of $|L|$ is unlikely to be explained by ψ alone, nor by reasonable variations of its constants/parameters. Algorithm 2C circumvents the major uncertainties relating to Z_i and ψ but it is only applicable on a limited stability range due to uncertainties relating to the empirical fit and its sensitivity to minor changes in ϵ. All three characterisation approaches are affected by errors in δ as these carry over into all subsequent derivations. For the limited number of Barbados scenes it was found that externally retrieved wind-direction data led to improved characterisation. In particular the stochastic difference between orientation of greatest variation and the wind direction limits the achievable precision of δ estimates.

Saildrone and R/V meteor validation of the Barbados results indicate statistically significant underestimation of σ_u/u_* leading to overestimation of $|L|$. Due to the limited number of Barbados scenes, the source of σ_u/u_* underestimation cannot be attributed to either underestimation of σ_u or overestimation of u_* using validation from the saildrone or R/V Meteor alone. Further analyses using the miscellaneous scenes and

ECMWF validation indicate a statistically significant underestimation of both σ_u and u_*. The former more than the latter which leads to an average 13% decreased σ_u/u_* ratio and a subsequent 50% overestimation of $|L|$ (with respect to ECMWF data).

Other than complications with respect to estimation techniques, stochastic constants, the GMF applicability, currents, swell and so forth, one should also consider which of the (often numerous) empirical equations are most suitable. The choice of different empirical derivations for x, ψ_m and L will influence results, albeit certainly less than the aforementioned other uncertainties. For that reason the major uncertainties should be resolved prior to fine-tuning the selection of equations.

A ranking of approximate uncertainties associated with constants and variables to the estimation of $|L|$ for the Barbados scenes is presented in Table 17. This ranking should not be seen as an error budget, rather as the potential order of improvements on a to-do list based on the scatter in results from scenario 1 through 5. Some unconsidered uncertainty sources include: the effect of image rotation on one-dimensional spectral analysis, the choice of spectral window and its effect on the spectral amplitude, the effect of radar viewing geometry on wind-direction estimation (and other parameters), the validity of Taylor's hypothesis under the selected circumstances and the validity of assuming the isotropic ratio of 4/3 during cross-wind analyses (i.e. $\beta = 4/3$ in Equation 3.16 or Equation 3.22) for the entirety of the $-5/3$ slope. This last point is expected to only affect cross-wind analysis such as performed on scenes containing two-dimensional rolls.

Table 17: Approximate uncertainty factor for L estimation of the Barbados scenes.

Factor > 2	2 ≥ Factor > 1.2	1.2 ≥ Factor
Z_i[a]	δ	κ
Ψ[b]	Swell[c]	α
GMF (wind magnitude)[d]	Currents[e]	ρ_{air}
	a[f]	T
	GMF (wind variance)[g]	

[a] Algorithm 2A only. Lesser effect on algorithms 2B and 2C.

[b] Algorithm 2B only.

[c] As per Figure 10 in Drennan et al. (1999).

[d] Based on the average difference between results obtained through CMOD-IFR2 and CMOD5.N.

[e] Minor effect expected for magnitude of currents in the Barbados study area. Uncertainty potential is greater for regions with stronger surface currents.

[f] For Charnock constants between $0.011 \leq a \leq 0.040$.

[g] Based on the average difference between results obtained through algorithm 2B and ECMWF and the assumption that this can (partially) be attributed to GMF-induced σ_u underestimation.

Conclusions and recommendations

6.1 Conclusions

The research objective of this study regards the spectral characterisation of the convective MABL by estimating key atmospheric parameters. Two existing characterisation methods (algorithms 2A and 2B) are tested and a new third method (algorithm 2C) is presented. All three methods are applied on newly available data from the Sentinel-1 constellation. Answers to the main research question and sub-questions are provided below.

Results of this study suggest shortcomings in all three characterisation methods. Algorithm 2A is unable to retrieve near-neutral values of L due to asymptotes in Equation 3.11 while errors in the estimation of Z_i can easily propagate a factor 2 error in the estimate of L. Similarly, considering the cubed power of σ_u in Equation 3.11, taking but minor liberties during spectral filtering can achieve a wide range of L's. The more frequently cited "silver bullet" method of spatial filtering to 300 m resolution does not achieve the desired effect either, as other authors inferred from results presented by Mourad et al. (2000), since it does not resolve any of the aforementioned limitations. For the analysed study areas algorithm 2B yields more precise results than algorithm 2A because its equations do not behave asymptotically for large $|L|$'s nor do they require spectral filtering. However, its estimates of $|L|$ suffer from uncertainty introduced by ψ and they are consistently overestimated with respect to validation. Overestimation of $|L|$ results in a lesser $|zL^{-1}|$ ratio meaning the atmospheric instability is underestimated. Results from the Barbados and miscellaneous scenes suggest the $|L|$ overestimation to be caused by statistically significant underestimation of σ_u rather than overestimation of u_*. The instability underestimation persists unless one assumes unreasonably favourable parameters and constants.

The CMOD5.N and CMOD-IFR2 GMFs employed in this study were not designed to take into account high-resolution sea-state variations. It is expected that these GMFs will underestimate the variability occurring at scales relevant to turbulent convection which would subsequently manifest itself as underestimation of the local wind-field slope and, thus, underestimation of σ_u and $|zL^{-1}|$. On the surface the observed consistent underestimation of σ_u and $|zL^{-1}|$ appears to support the GMF-induced underestimation hypothesis. However, definitive conclusions cannot be drawn due to limited number of scenes analysed as well as uncertainty relating to other influencing factors. There is reason to believe that neither currents, swell, estimation errors nor reasonable variations in constants could individually cause the observed $|L|$ overestimation, though unfortuitous combinations of these four can not be excluded. The older CMOD-IFR2 does not suffer from $|L|$ overestimation although this is due to it yielding lower wind speeds rather than taking into account variable sea states. A minor multiplication of CMOD5.N's wind-field slope tends to be sufficient at achieving the validation values.

The suitability of GMFs appears to have gone unquestioned in previous studies due to the uncertainty and malleability of results. A new characterisation approach (algorithm 2C) was developed which circumvents major uncertainties inherent to algorithms 2A and 2B. Additionally, algorithm 2C uses the more applicable surface-layer spectral characteristics rather than algorithm 2B's mixed-layer spectral characteristics. Due to limitations of its own, algorithm 2C produces results over a limited stability range only. This being

between approximately 10 m $< |L| <$ 50 m. For all other stability ranges algorithm 2B is preferred. An example is provided showing the ability of algorithm 2C to estimate ψ when combined with algorithm 2B. It is thought that, if applied over the appropriate stability range, a combination of algorithms 2C and 2A could yield independent estimates of Z_i by exploiting their respective different dependencies on this parameter. Improvements with respect to the estimation of TKE dissipation rate ϵ or the dimensionless gradient profile function ϕ_e are necessary before algorithm 2C could replace algorithm 2B over a larger stability range.

Answers to the sub-questions:

1. *What imprints does the MABL leave on the water surface?*

   Convective two-dimensional rolls and three-dimensional cells within the MABL exert a stress on the water surface representative of their respective wind-field structure. These stress patterns result in increased surface roughness and, in turn, an increase in observed radar signal. Thus, imprints of MABL convection are visible in radar imagery as water-surface roughness patterns following the structure of convective wind fields.

2. *Can the imprints caused by the MABL be separated from other signal sources?*

   Contamination of the MABL-induced convection signatures can be mitigated by only analysing homogeneous study areas for which the visual structures have been classified as either "clean" roll or cell-like convection. For such areas this study found approximate -5/3 spectral power laws within spatial wavelengths corresponding to microscale turbulence (after a microscale peak or plateau). Thus, for homogeneous areas with strong convection, the MABL's imprints are mostly separable from other signal sources. Exceptions include surface imprints caused by swell and surface currents. Both these phenomena can interfere with that of the MABL without obvious deterioration of the spectral slope, especially for low wind speed settings ($\overline{U} < 5$ ms^{-1}). Further studies could use differential polarimetry, such as discussed in Ufermann and Romeiser (1999), to isolate and quantify the influence of surface currents. Quantifying the influence of swell remains a separate issue.

3. *Are the employed GMFs capable of estimating the MABL-induced wind-field variations?*

   This study displays the characterisation sensitivity to minor alterations of σ_u and u_* and thereby the importance of an accurate GMF. Results from this study support the GMF-induced σ_u underestimation hypothesis; estimates of $|L|$ are consistently greater than those retrieved from validation and the source for this overestimation appears to be underestimation of σ_u. Quantifying the net effect of possible GMF-induced underestimation on characterisation is complicated by the limited number of scenes analysed as well as uncertainty relating to other influencing factors. Thus, modern GMFs may limit successful MABL characterisation, though uncertainties relating to other parameters and constants equally or exceedingly limit characterisation beyond that of possible GMF-induced σ_u underestimation.

4. *How can the MABL's imprints be related to a MABL state?*

   Three characterisation methods are shown that employ similarity theories to relate estimates of the wind direction, convective boundary layer height and wind-field information to a specific atmospheric stability. Results of this study suggest limitations of all considered characterisation methods. The

estimations of Z_i and δ are complicated by stochastic constants and it is hypothesised that the GMF is responsible for underestimation of σ_u. These and further uncertainties propagate as errors in the estimation of the atmospheric instability.

Answer to the main research question of this study:

- *"To what extent is it feasible to characterise the state of the marine atmospheric boundary layer over the ocean by means of spectral analysis of Sentinel-1 SAR amplitude observations?"*

  Characterisation feasibility is assessed through six atmospheric parameters, namely: wind direction δ, average neutral wind speed $\overline{U_n}$, friction velocity u_*, horizontal wind-field variance σ_u^2, CBL depth Z_i and Obukhov length L. Of particular interest are the latter three as these cannot be estimated (on relevant scales) with contemporary scatterometers.

  The characterisation performance varies per atmospheric parameter. Estimated wind directions yield worse further characterisation results than wind directions retrieved from ECMWF. Spatial averaging and improved empirical constants could improve wind-direction estimation. Compared to in-situ validation data, estimates of Z_i are more accurate but less precise than those retrieved from ECMWF (RMSE = 165 m and $R^2 = 0.100$ versus RMSE = 201 m and $R^2 = 0.996$ respectively). The RMSE of estimated average neutral wind speeds for all scenes with respect to validation is 0.3 ms^{-1} and 0.8 ms^{-1} using CMOD5.N and CMOD-IFR2 respectively. The difference between the latter and validation being statistically significant ($p < 0.1\%$) whereas that between the former and validation is not ($p > 50\%$). The choice of GMF greatly affects further characterisation; absolute Obukhov lengths estimated with CMOD-IFR2 are a factor 2 smaller than those estimated with CMOD5.N due to the former's underestimation of neutral wind speed. When using the more suitable CMOD5.N, the σ_u/u_* ratio is consistently underestimated with respect to validation. Since $-L \propto (\sigma_u/u_*)^{-3}$, an underestimated ratio leads to overestimation of $|L|$ and in turn underestimation of the atmospheric instability $|zL^{-1}|$. An analysis of the Barbados and miscellaneous scenes suggests that a statistically significant underestimation of σ_u results in an average 13% underestimation of σ_u/u_* and a subsequent 50% overestimation of $|L|$.

  To summarise, wind directions retrieved from atmospheric models are favoured over those estimated in this study. When using a suitable GMF, estimated wind speeds and friction velocities are approximately on equal footing to those received from in-situ validation and an atmospheric model. Estimates of CBL depth are slightly more accurate but substantially less precise than those received from atmospheric models with respect to in-situ validation. Lastly, estimates for horizontal wind-field variance and Obukhov length are biased with respect to validation. Of the above, the estimation of wind direction and CBL depth can be improved through refinement of the relevant empirical constants whereas the estimation of horizontal wind-field variance and Obukhov length can be improved by finding and quantifying the source(s) of horizontal wind-field variance underestimation.

To conclude, spaceborne characterisation of the marine atmospheric boundary layer still faces numerous challenges that limit the practical utility of remote sensing over in-situ measurements. But no doubt science will find its way with the contemporary challenges, just like the scientific understanding of water and turbulence has come a long way since Leonardo da Vinci's *Studies of water* from 1510.

6.2 Recommendations

The methodology described in this study contains a host of steps and processes that could each be improved upon further. However, the purpose of this study concerns the general characterisation of the MABL, not the optimisation of a specific processing step. To this end the recommendations shall focus on those that could lead to a direct improvement in the characterisation effort. Based on the encountered deficiencies, this study recommends the following improvements be made in potential successor studies.

1. *Collect large database of radar scenes with two-dimensional or three-dimensional convection with known atmospheric conditions*

   This study relies on but a few radar scenes for which fewer still have validation beyond that provided by ECMWF. A larger database of radar scenes with corresponding validation data is required in order to achieve greater statistical confidence and to make quantitative statements regarding the impact of specific parameters. Ideally this would be achieved by collocation of radar scenes with a network of ocean buoys. A more feasible starting point may be to use the labelled image database provided my Wang et al. (2019b) in combination with the ERA5 database, similar to Wang et al. (2019a).

2. *Derive constants for Z_i and δ rather than using stochastic constants*

   The derivation of both Z_i and δ requires use of empirical constants. The stochastic nature of these constants adds significant uncertainty to further computations. The overall characterisation process would benefit if these constants could be derived rather than arbitrarily set. One possibility for deriving Z_i could be to use the different dependencies of L on Z_i in algorithms 2A, 2B and 2C.

3. *Derive ψ in an independent fashion in order to apply algorithm 2B*

   The natural variability and importance of ψ dictate that a constant value will not suffice in algorithm 2B. An independent derivation of ψ should be used in order to consistently and successfully apply algorithm 2B.

4. *Improve algorithm 2C to be applicable over larger stability range*

   Usage of algorithm 2C is restricted to a limited stability range. Considering the benefits of algorithm 2C over algorithms 2A and 2B, increasing the feasible stability range of algorithm 2C would improve characterisation efforts.

5. *Adapt GMF for usage in high-resolution variable sea states*

   Should further research support the hypothesised inadequacy of current GMFs, a new GMF ought to be developed capable of accounting for the sea state. This could include, for instance, a spatial awareness term in the GMF yielding variable results depending on the estimated local wind-field slope. In other words, the GMF would be trained assuming a Charnock constant based not only on wind-field magnitude but also on wind-field slope.

6. *Quantify the effect of swell on characterisation and determine the validity of removing swell signatures from two-dimensional spectrum*

Previous studies illustrate the ability of swell to influence ocean-atmosphere coupling. Depending on the frequency and severity of contamination, the influence of swell on characterisation methods should be quantified in order to remove its signal from further analyses. Alternatively, the great abundance of satellite observations could be exploited by identifying and removing all scenes containing significant swell signatures.

7. *Improve threshold filters*

   Tiles were filtered based on anomalous PSD amplitude and the fit to the -5/3 power law. Additional filters could be put in place to remove further low-quality results. Furthermore, rather than considering each tile as separate, one could include neighbouring tiles for quality control, e.g. by comparing the δ estimate of a tile to its direct neighbours and or by applying spatial averaging.

8. *Improve convection classifier*

   Although this study does not focus on the classification of radar images, it was found that a basic CNN classifier struggled to discern between rolls and cells. While classification results may appear fine visually, the corresponding two-dimensional spectra could suggest the opposite class. Thus, the classification metrics should more heavily weigh the distribution and orientation of power in the two-dimensional spectrum. Further improvements to the classifier could be achieved by incorporating more distinct classes (rather than rolls and cells only) and the addition of an object and or land removal higher up the SNAP processing chain. The eventual goal of the classifier should be to perform classification on a tile level rather than on a scene level.

References

Alpers, W. and Brümmer, B. (1994). Atmospheric boundary layer rolls observed by the synthetic aperture radar aboard the ers-1 satellite. *Journal of Geophysical Research: Oceans*, 99(C6):12613–12621.

Alpers, W. and Hennings, I. (1984). A theory of the imaging mechanism of underwater bottom topography by real and synthetic aperture radar. *Journal of Geophysical Research: Oceans*, 89(C6):10529–10546.

Andreas, E. L. et al. (1989). Thermal and size evolution of sea spray droplets.

Archer, C. L., Colle, B. A., Veron, D. L., Veron, F., and Sienkiewicz, M. J. (2016). On the predominance of unstable atmospheric conditions in the marine boundary layer offshore of the us northeastern coast. *Journal of Geophysical Research: Atmospheres*, 121(15):8869–8885.

Ardhuin, F., Chapron, B., and Collard, F. (2009). Observation of swell dissipation across oceans. *Geophysical Research Letters*, 36(6).

Arnault, S. (1987). Tropical atlantic geostrophic currents and ship drifts. *Journal of Geophysical Research: Oceans*, 92(C5):5076–5088.

Augstein, E., Schmidt, H., and Ostapoff, F. (1974). The vertical structure of the atmospheric planetary boundary layer in undisturbed trade winds over the atlantic ocean. *Boundary-Layer Meteorology*, 6(1):129–150.

Baranowski et al. (2021). EUREC4A's Meteor. Manuscript in preparation for ESSD.

Barbie Bischof, Arthur J. Mariano, E. H. R. (2003). The North Brazil Current. Online at https://oceancurrents.rsmas.miami.edu/atlantic/north-brazil.html; accessed June 14th 2021.

Bourlès, B., Gouriou, Y., and Chuchla, R. (1999). On the circulation in the upper layer of the western equatorial atlantic. *Journal of Geophysical Research: Oceans*, 104(C9):21151–21170.

Brown, R. A. (1980). Longitudinal instabilities and secondary flows in the planetary boundary layer: A review. *Reviews of Geophysics*, 18(3):683–697.

Brüning, C., Alpers, W., and Hasselmann, K. (1990). Monte-carlo simulation studies of the nonlinear imaging of a two dimensional surface wave field by a synthetic aperture radar. *Int. J. Remote Sensing*, 2(10):1695–1727.

Caughey, S. and Palmer, S. (1979). Some aspects of turbulence structure through the depth of the convective boundary layer. *Quarterly Journal of the Royal Meteorological Society*, 105(446):811–827.

Champagne, F., Friehe, C., LaRue, J., and Wynagaard, J. (1977). Flux measurements, flux estimation techniques, and fine-scale turbulence measurements in the unstable surface layer over land. *Journal of Atmospheric Sciences*, 34(3):515–530.

Chan, Y. K. and Koo, V. (2008). An introduction to synthetic aperture radar (sar). *Progress In Electromagnetics Research B*, 2:27–60.

Charnock, H. (1955). Wind stress on a water surface. *Quarterly Journal of the Royal Meteorological Society*, 81(350):639–640.

Cheynet, E., Jakobsen, J. B., and Reuder, J. (2018). Velocity spectra and coherence estimates in the marine atmospheric boundary layer. *Boundary-layer meteorology*, 169(3):429–460.

Collecte Localisation Satellites (2016). Sentinel-1 Product Definition. ref. S1-RS-MDA-52-7440. Online at https://sentinel.esa.int/web/sentinel/user-guides/sentinel-1-sar/document-library/-/asset_publisher/1dO7RF5fJMbd/content/sentinel-1-product-definition; accessed May 14th 2021.

Deardorff, J. W. (1970). Preliminary results from numerical integrations of the unstable planetary boundary layer. *Journal of the Atmospheric Sciences*, 27(8):1209–1211.

Deardorff, J. W. (1974). Three-dimensional numerical study of the height and mean structure of a heated planetary boundary layer. *Boundary-Layer Meteorology*, 7(1):81–106.

Donelan, M. A., Drennan, W. M., and Katsaros, K. B. (1997). The air–sea momentum flux in conditions of wind sea and swell. *Journal of Physical Oceanography*, 27(10):2087–2099.

Dorman, G. E. and Mollo-Christensen, E. (1973). Observation of the structure on moving gust patterns over a water surface ("cat's paws"). *Journal of Physical Oceanography*, 3(1):120–132.

Drennan, W. M., Kahma, K. K., and Donelan, M. A. (1999). On momentum flux and velocity spectra over waves. *Boundary-Layer Meteorology*, 92(3):489–515.

ESA (2020). Report for assessment: Earth explorer 10 candidate mission harmony. Technical report, Noordwijk, The Netherlands.

ESA (2021). Atmospheric convective cells. Online at https://earth.esa.int/web/guest/missions/esa-operational-eo-missions/ers/instruments/sar/applications/tropical/-/asset_publisher/tZ7pAG6SCnM8/content/atmospheric-convective-cells; accessed March 4th 2021.

ESA (2021a). Sentinel-1. ref. S1-RS-MDA-52-7440. Online at https://sentinel.esa.int/web/sentinel/missions/sentinel-1; accessed May 15th 2021.

ESA (2021b). Sentinel-1 SAR instrument. ref. S1-RS-MDA-52-7440. Online at https://sentinel.esa.int/web/sentinel/technical-guides/sentinel-1-sar/sar-instrument; accessed May 15th 2021.

Etling, D. and Brown, R. (1993). Roll vortices in the planetary boundary layer: A review. *Boundary-Layer Meteorology*, 65(3):215–248.

EUREC^{4}A (2020a). Ceilometer. Data retrieved from https://observations.ipsl.fr/aeris/eurec4a-data/SHIPS/RV-METEOR/ceilometer/; accessed September 4th 2021.

EUREC^{4}A (2020b). Cloud radar. Data retrieved from https://observations.ipsl.fr/aeris/eurec4a-data/SHIPS/RV-METEOR/cloudradar/hydrometeor-fraction/; accessed September 4th 2021.

EUREC^{4}A (2020c). Radiosondes. Data retrieved from https://observations.ipsl.fr/aeris/eurec4a-data/PRODUCTS/MERGED-MEASUREMENTS/RADIOSOUNDINGS/v3.0.0/level2/; accessed September 4th 2021.

EUREC^{4}A (2020d). GOES-E video time series. Data retrieved from https://observations.ipsl.fr/aeris/eurec4a-data/PRODUCTS/GOES-E_movies/Visible/; accessed September 4th 2021.

Fairall, C., Edson, J., Larsen, S. E., and Mestayer, P. (1990). Inertial-dissipation air-sea flux measurements: a prototype system using realtime spectral computations. *Journal of Atmospheric and Oceanic Technology*, 7(3):425–453.

Fairall, C. W., Bradley, E. F., Rogers, D. P., Edson, J. B., and Young, G. S. (1996). Bulk parameterization of air-sea fluxes for tropical ocean-global atmosphere coupled-ocean atmosphere response experiment. *Journal of Geophysical Research: Oceans*, 101(C2):3747–3764.

Faller, A. J. (1964). The angle of windrows in the ocean 1. *Tellus*, 16(3):363–370.

Fiedler, F. and Panofsky, H. A. (1970). Atmospheric scales and spectral gaps. *Bulletin of the American Meteorological Society*, 51(12):1114–1120.

Filipponi, F. (2019). Sentinel-1 grd preprocessing workflow. In *Multidisciplinary Digital Publishing Institute Proceedings*, volume 18, page 11.

Foken, T. (2006). 50 years of the monin–obukhov similarity theory. *Boundary-Layer Meteorology*, 119(3):431–447.

Foster, R. (2013). Signature of large aspect ratio roll vortices in synthetic aperture radar images of tropical cyclones. *Oceanography*, 26(2):58–67.

Geldsetzer, T., Khurshid, S. K., Warner, K., Botelho, F., and Flett, D. (2019). Wind speed retrieval from simulated radarsat constellation mission compact polarimetry sar data for marine application. *Remote Sensing*, 11(14):1682.

Gerling, T. (1986). Structure of the surface wind field from the seasat sar. *Journal of Geophysical Research: Oceans*, 91(C2):2308–2320.

Hersbach, H. (2008). *CMOD5. N: A C-band geophysical model function for equivalent neutral wind*. European Centre for Medium-Range Weather Forecasts.

Hersbach, H. (2010). Comparison of c-band scatterometer cmod5. n equivalent neutral winds with ecmwf. *Journal of Atmospheric and Oceanic Technology*, 27(4):721–736.

Hersbach, H. (2011). Sea surface roughness and drag coefficient as functions of neutral wind speed. *Journal of Physical Oceanography*, 41(1):247–251.

Högström, U. (1996). Review of some basic characteristics of the atmospheric surface layer. *Boundary-Layer Meteorology*, 78(3):215–246.

Holt, B. (2005). Chapter 2 sar imaging of the ocean surface. *Synthetic Aperture Radar Marine User's Manual (NOAA/NESDIS); Jackson, CR, Apel, JR, Eds*, pages 25–80.

IPCC (2013). *Observations: Ocean*, book section 3, page 255–316. Cambridge University Press, Cambridge, United Kingdom and New York, NY, USA.

James, S. (2017). Using sentinel-1 sar satellites to map wind speed variation across offshore wind farm clusters. In *Journal of Physics: Conference Series*, volume 926, page 012004. IOP Publishing.

Kaimal, J., Wyngaard, J., Haugen, D., Coté, O., Izumi, Y., Caughey, S., and Readings, C. (1976). Turbulence structure in the convective boundary layer. *Journal of Atmospheric Sciences*, 33(11):2152–2169.

Kaimal, J. C., Wyngaard, J., Izumi, Y., and Coté, O. (1972). Spectral characteristics of surface-layer turbulence. *Quarterly Journal of the Royal Meteorological Society*, 98(417):563–589.

Katul, G. and Chu, C.-R. (1998). A theoretical and experimental investigation of energy-containing scales in the dynamic sublayer of boundary-layer flows. *Boundary-Layer Meteorology*, 86(2):279–312.

Kerbaol, V., Chapron, B., and Vachon, P. W. (1998). Analysis of ers-1/2 synthetic aperture radar wave mode imagettes. *Journal of Geophysical Research: Oceans*, 103(C4):7833–7846.

Khanna, S. and Brasseur, J. G. (1997). Analysis of monin–obukhov similarity from large-eddy simulation. *Journal of Fluid Mechanics*, 345:251–286.

Koch, W. (2004). Directional analysis of sar images aiming at wind direction. *IEEE Transactions on Geoscience and Remote Sensing*, 42(4):702–710.

Kooijmans, L. M. and Hartogensis, O. K. (2016). Surface-layer similarity functions for dissipation rate and structure parameters of temperature and humidity based on eleven field experiments. *Boundary-Layer Meteorology*, 160(3):501–527.

Larsén, X., Smedman, A.-S., and Högström, U. (2004). Air–sea exchange of sensible heat over the baltic sea. *Quarterly Journal of the Royal Meteorological Society: A journal of the atmospheric sciences, applied meteorology and physical oceanography*, 130(597):519–539.

Lemone, M. A. (1973). The structure and dynamics of horizontal roll vortices in the planetary boundary layer. *Journal of Atmospheric Sciences*, 30(6):1077–1091.

Lilly, D. K. (1989). Two-dimensional turbulence generated by energy sources at two scales. *Journal of Atmospheric Sciences*, 46(13):2026–2030.

Lundquist, J. and Bariteau, L. (2015). Dissipation of turbulence in the wake of a wind turbine. *Boundary-Layer Meteorology*, 154(2):229–241.

Malkus, J. S. (1958). On the structure of the trade wind moist layer.

Monin, A. S. and Obukhov, A. M. (1954). Basic laws of turbulent mixing in the surface layer of the atmosphere. *Contrib. Geophys. Inst. Acad. Sci. USSR*, 151(163):e187.

Mourad, P. D. (1996). Inferring multiscale structure in atmospheric turbulence using satellite-based synthetic aperture radar imagery. *Journal of Geophysical Research: Oceans*, 101(C8):18433–18449.

Mourad, P. D., Thompson, D. R., and Vandemark, D. C. (2000). Extracting fine-scale wind fields from synthetic aperture radar images of the ocean surface. *Johns Hopkins APL technical digest*, 21(1):108–115.

Nastrom, G., Gage, K. S., and Jasperson, W. (1984). Kinetic energy spectrum of large-and mesoscale atmospheric processes. *Nature*, 310(5972):36–38.

Nicholls, S. and Readings, C. (1981). Spectral characteristics of surface layer turbulence over the sea. *Quarterly Journal of the Royal Meteorological Society*, 107(453):591–614.

NOAA (2020). How much of the ocean have we explored? Online at https://oceanservice.noaa.gov/facts/exploration.html; accessed February 20th 2021.

Oncley, S. P., Friehe, C. A., Larue, J. C., Businger, J. A., Itsweire, E. C., and Chang, S. S. (1996). Surface-layer fluxes, profiles, and turbulence measurements over uniform terrain under near-neutral conditions. *Journal of Atmospheric Sciences*, 53(7):1029–1044.

Panofsky, H. A., Tennekes, H., Lenschow, D. H., and Wyngaard, J. (1977). The characteristics of turbulent velocity components in the surface layer under convective conditions. *Boundary-Layer Meteorology*, 11(3):355–361.

Park, J.-W., Korosov, A. A., Babiker, M., Sandven, S., and Won, J.-S. (2017). Efficient thermal noise removal for sentinel-1 topsar cross-polarization channel. *IEEE Transactions on Geoscience and Remote Sensing*, 56(3):1555–1565.

Paulson, C. A. (1970). The mathematical representation of wind speed and temperature profiles in the unstable atmospheric surface layer. *Journal of Applied Meteorology and Climatology*, 9(6):857–861.

Quilfen, Y., Chapron, B., Collard, F., and Vandemark, D. (2004). Relationship between ers scatterometer measurement and integrated wind and wave parameters. *Journal of Atmospheric and Oceanic Technology*, 21(2):368–373.

Quilfen, Y., Chapron, B., Elfouhaily, T., Katsaros, K., and Tournadre, J. (1998). Observation of tropical cyclones by high-resolution scatterometry. *Journal of Geophysical Research: Oceans*, 103(C4):7767–7786.

Quinn, Patricia K et al. (2021). Measurements from the rv ronald h. brown and related platforms as part of the atlantic tradewind ocean-atmosphere mesoscale interaction campaign (atomic). *Earth System Science Data*, 13(4):1759–1790.

Rizaev, I., Karakuş, O., Hogan, S. J., and Achim, A. (2021). Modeling and sar imaging of the sea surface: a review of the state-of-the-art with simulations. *arXiv preprint arXiv:2102.05199*.

Robinson, I. S. (2010). *Ocean surface waves*, pages 293–332. Springer Berlin Heidelberg, Berlin, Heidelberg.

Robinson, I. S. and Fangohr, S. (2010). *Fluxes through the air–sea interface*, pages 359–390. Springer Berlin Heidelberg, Berlin, Heidelberg.

Rousseeuw, P. J. and Croux, C. (1993). Alternatives to the median absolute deviation. *Journal of the American Statistical association*, 88(424):1273–1283.

Schott, F. A., Brandt, P., Hamann, M., Fischer, J., and Stramma, L. (2002). On the boundary flow off brazil at 5–10 s and its connection to the interior tropical atlantic. *Geophysical Research Letters*, 29(17):21–1.

Sikora, T., Young, G., Beal, R., and Edson, J. (1995). Use of spaceborne synthetic aperture radar imagery of the sea surface in detecting the presence and structure of the convective marine atmospheric boundary layer. *Monthly weather review*, 123(12):3623–3632.

Sikora, T., Young, G., Beal, R., Monaldo, F., and Vachon, P. (2006). Applications of synthetic aperture radar in marine meteorology. *WIT Transactions on State-of-the-art in Science and Engineering*, 23.

Sikora, T. D., Bleidorn, J. C., and Thompson, D. R. (1999). On the extraction of atmospheric structure from synthetic aperture radar imagery. In *IEEE 1999 International Geoscience and Remote Sensing Symposium. IGARSS'99 (Cat. No. 99CH36293)*, volume 4, pages 1972–1974. IEEE.

Sikora, T. D. and Thompson, D. (2002). Air-sea fluxes from synthetic aperture radar: An update. In *11th Conference on Satellite Meteorology and Oceanography*.

Sikora, T. D., Thompson, D. R., and Bleidorn, J. C. (2000). Testing the diagnosis of marine atmospheric boundary-layer structure from synthetic aperture radar. *JOHNS HOPKINS APL TECHNICAL DIGEST*, 21(1):95.

Sikora, T. D. and Ufermann, S. (2004). Marine atmospheric boundary layer cellular convection and longitudinal roll vortices. *Synthetic aperture radar marine user's manual*, pages 321–330.

Sikora, T. D., Young, G. S., Shirer, H. N., and Chapman, R. D. (1997). Estimating convective atmospheric boundary layer depth from microwave radar imagery of the sea surface. *Journal of Applied Meteorology*, 36(7):833–845.

Smedman, A.-S., Högström, U., Hunt, J. C., and Sahlée, E. (2007). Heat/mass transfer in the slightly unstable atmospheric surface layer. *Quarterly Journal of the Royal Meteorological Society: A journal of the atmospheric sciences, applied meteorology and physical oceanography*, 133(622):37–51.

Smith, S. D. (1988). Coefficients for sea surface wind stress, heat flux, and wind profiles as a function of wind speed and temperature. *Journal of Geophysical Research: Oceans*, 93(C12):15467–15472.

Smith, S. D., Fairall, C. W., Geernaert, G. L., and Hasse, L. (1996). Air-sea fluxes: 25 years of progress. *Boundary-Layer Meteorology*, 78(3):247–290.

Sreenivasan, K. R. (1995). On the universality of the kolmogorov constant. *Physics of Fluids*, 7(11):2778–2784.

Stevens, B. et al. (2021). Eurec 4 a. *Earth System Science Data*, 13(8):4067–4119.

Stull, R. B. (1988). *An introduction to boundary layer meteorology*, volume 13. Springer Science & Business Media.

Thompson, T., Liu, W., and Weissman, D. (1983). Synthetic aperture radar observation of ocean roughness from rolls in an unstable marine boundary layer. *Geophysical research letters*, 10(12):1172–1175.

Toffoli, A. and Bitner-Gregersen, E. M. (2017). Types of ocean surface waves, wave classification. *Encyclopedia of Maritime and Offshore Engineering*, pages 1–8.

Trindade, A., Portabella, M., Stoffelen, A., Lin, W., and Verhoef, A. (2019). Erastar: a high-resolution ocean forcing product. *IEEE Transactions on Geoscience and Remote Sensing*, 58(2):1337–1347.

Ufermann, S. and Romeiser, R. (1999). Numerical study on signatures of atmospheric convective cells in radar images of the ocean. *Journal of Geophysical Research: Oceans*, 104(C11):25707–25719.

Vachon, P., Monaldo, F., Holt, B., Lehner, S., Jackson, C., and Apel, J. (2004). Ocean surface waves and spectra. *Synthetic Aperture Radar Marine User's Manual*, pages 139–169.

Vachon, P. W., Krogstad, H. E., and Paterson, J. S. (1994). Airborne and spaceborne synthetic aperture radar observations of ocean waves. *Atmosphere-Ocean*, 32(1):83–112.

Vachon, P. W., Wolfe, J., and Greidanus, H. (2012). Analysis of sentinel-1 marine applications potential. In *2012 IEEE International Geoscience and Remote Sensing Symposium*, pages 1734–1737. IEEE.

Verburg, P. and Antenucci, J. P. (2010). Persistent unstable atmospheric boundary layer enhances sensible and latent heat loss in a tropical great lake: Lake tanganyika. *Journal of Geophysical Research: Atmospheres*, 115(D11).

Wackerman, C. C., Rufenach, C. L., Shuchman, R. A., Johannessen, J. A., and Davidson, K. L. (1996). Wind vector retrieval using ers-1 synthetic aperture radar imagery. *IEEE Transactions on Geoscience and Remote Sensing*, 34(6):1343–1352.

Wang, C., Mouche, A., Foster, R. C., Vandemark, D., Stopa, J. E., Tandeo, P., Longepe, N., and Chapron, B. (2019a). Characteristics of marine atmospheric boundary layer roll vortices from sentinel-1 sar wave mode. In *IGARSS 2019-2019 IEEE International Geoscience and Remote Sensing Symposium*, pages 7908–7911. IEEE.

Wang, C., Mouche, A., Tandeo, P., Stopa, J. E., Longépé, N., Erhard, G., Foster, R. C., Vandemark, D., and Chapron, B. (2019b). A labelled ocean sar imagery dataset of ten geophysical phenomena from sentinel-1 wave mode. *Geoscience Data Journal*, 6(2):105–115.

Wiehle, S., Pleskachevsky, A., and Gebhardt, C. (2019). Automatic bathymetry retrieval from sar images. *CEAS Space Journal*, 11(1):105–114.

Wilson, J. (2008). Monin-obukhov functions for standard deviations of velocity. *Boundary-layer meteorology*, 129(3):353–369.

Woodcock, A. H. (1975). Thermals over the sea and gull flight behavior. *Boundary-Layer Meteorology*, 9(1):63–68.

Wyngaard, J. and Coté, O. (1971). The budgets of turbulent kinetic energy and temperature variance in the atmospheric surface layer. *Journal of Atmospheric Sciences*, 28(2):190–201.

Yelland, M. and Taylor, P. K. (1996). Wind stress measurements from the open ocean. *Journal of Physical Oceanography*, 26(4):541–558.

Young, G. (1987). Mixed layer spectra from aircraft measurements. *Journal of Atmospheric Sciences*, 44(9):1251–1256.

Young, G. S. (1988). Turbulence structure of the convective boundary layer. part ii. phonenix 78 aircraft observations of thermals and their environment. *Journal of Atmospheric Sciences*, 45(4):727–735.

Young, G. S. (2000). Sar signatures of the marine atmospheric boundary layer: implications for numerical forecasting. *Johns Hopkins APL technical digest*, 21(1):27–32.

Young, G. S. and Kristensen, L. (1992). Surface-layer gusts for aircraft operation. *Boundary-layer meteorology*, 59(3):231–242.

Young, G. S., Kristovich, D. A., Hjelmfelt, M. R., and Foster, R. C. (2002). Rolls, streets, waves, and more: A review of quasi-two-dimensional structures in the atmospheric boundary layer. *Bulletin of the American Meteorological Society*, 83(7):997–1002.

Young, G. S., Sikora, T. D., and Winstead, N. S. (2000). Inferring marine atmospheric boundary layer properties from spectral characteristics of satellite-borne sar imagery. *Monthly weather review*, 128(5):1506–1520.

Zecchetto, S. and De Biasio, F. (2002). On shape, orientation, and structure of atmospheric cells inside wind rolls in two sar images. *IEEE transactions on geoscience and remote sensing*, 40(10):2257–2262.

Zecchetto, S., Trivero, P., Fiscella, B., and Pavese, P. (1998). Wind stress structure in the unstable marine surface layer detected by sar. *Boundary-layer meteorology*, 86(1):1–28.

Appendix

A.1 Python code

Python scripts for the processes described in section 3 (with the exclusion of those performed in SNAP) are publicly accessible in the following repository https://github.com/owenod1/MSc_thesis. The repository contains four separate scripts, namely MSc.py, MSc_equations.py, CMOD5N.py and CMOD_IFR2.py. The MSc.py script is the main script in which inputs are loaded and which calls the other three scripts. MSc_equations.py contains all the relevant custom functions with the exclusion of the GMF functions contained in CMOD5N.py and CMOD_IFR2.py respectively.

A.2 Radar scenes

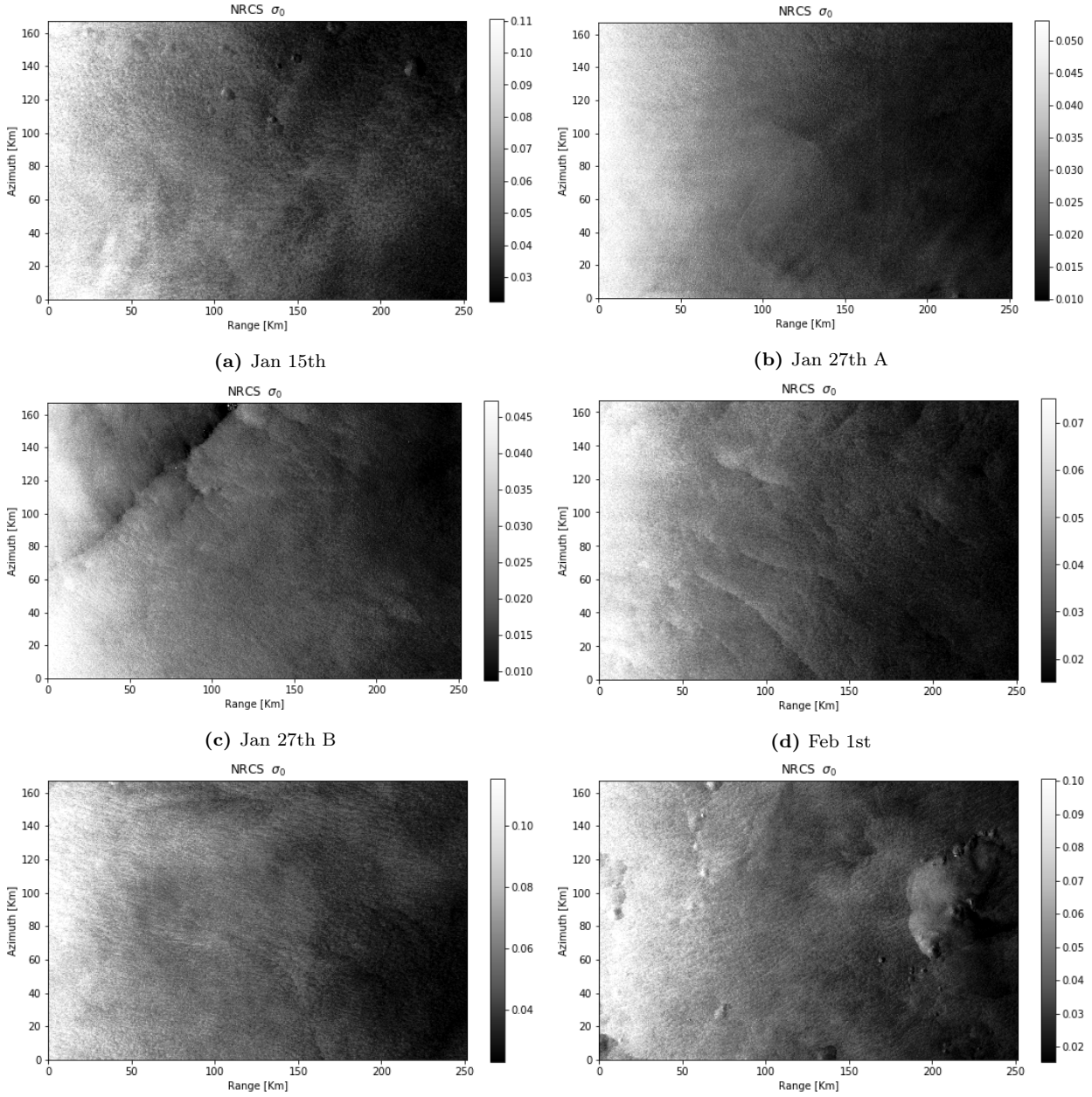

(a) Jan 15th

(b) Jan 27th A

(c) Jan 27th B

(d) Feb 1st

(e) Feb 8th

(f) Feb 20th

Figure A.1: Sentinel-1 scenes used in the Barbados study area. Metadata can be found in Table 5.

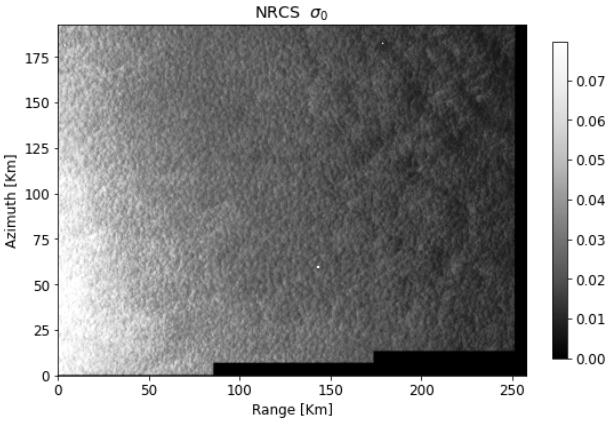

(a) Carolina

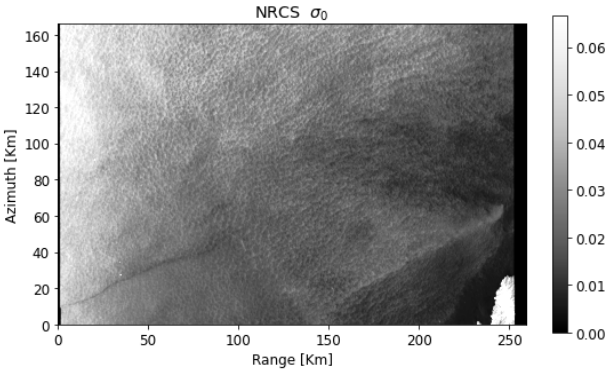

(b) Sea of Japan

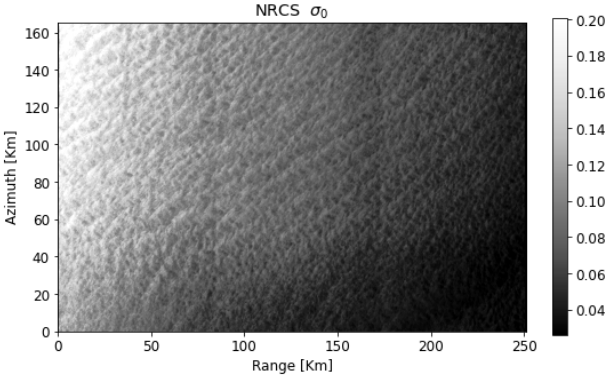

(c) Bering Sea

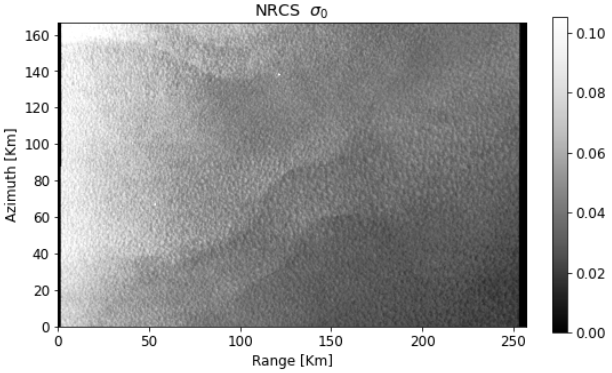

(d) Georgia

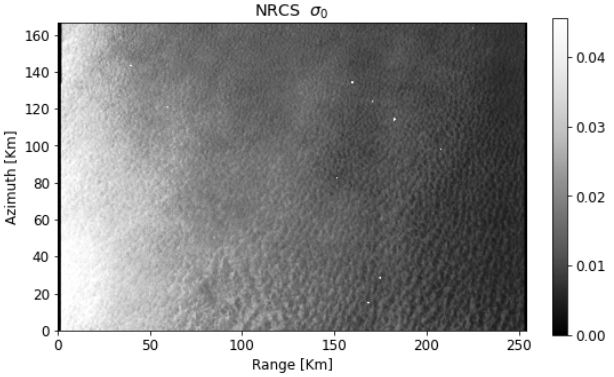

(e) Portugal

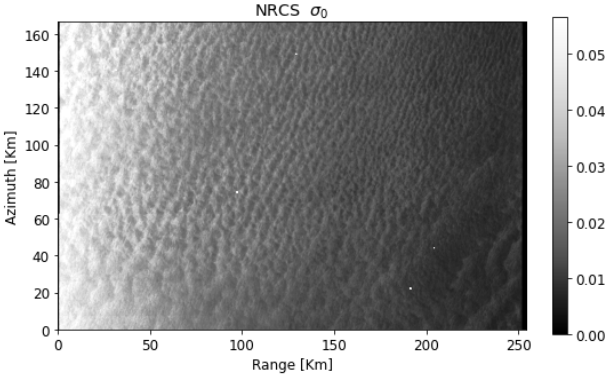

(f) Madeira

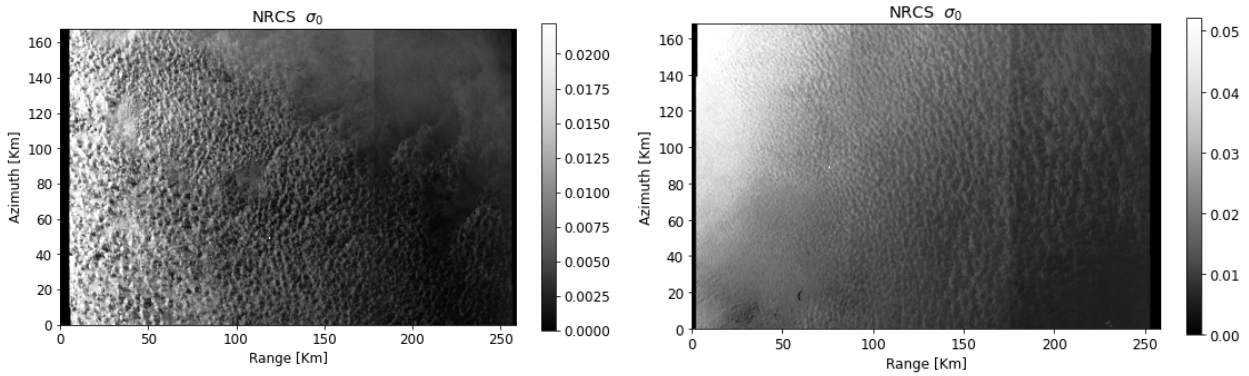

(g) Peru **(h)** Argentina

Figure A.2: Miscellaneous Sentinel-1 scenes. Metadata can be found in Table 7. Contamination by snippet of North Korean coast next to the Sea of Japan is avoided by providing median results, as is contamination by the occasional strong reflector.

A.3 Location validation data

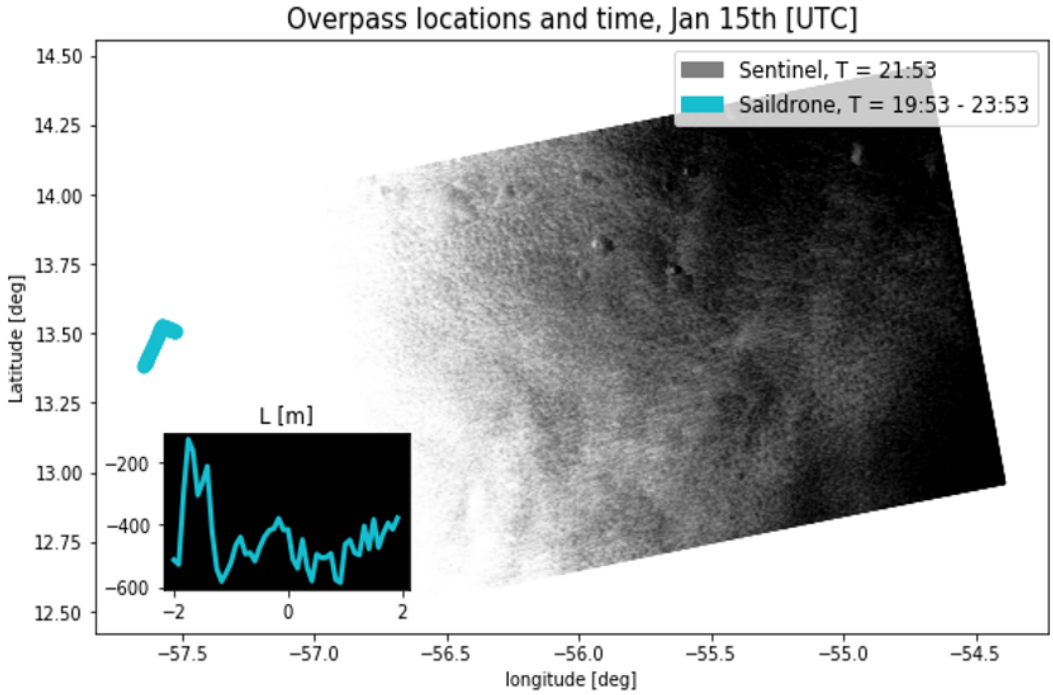

Figure A.3

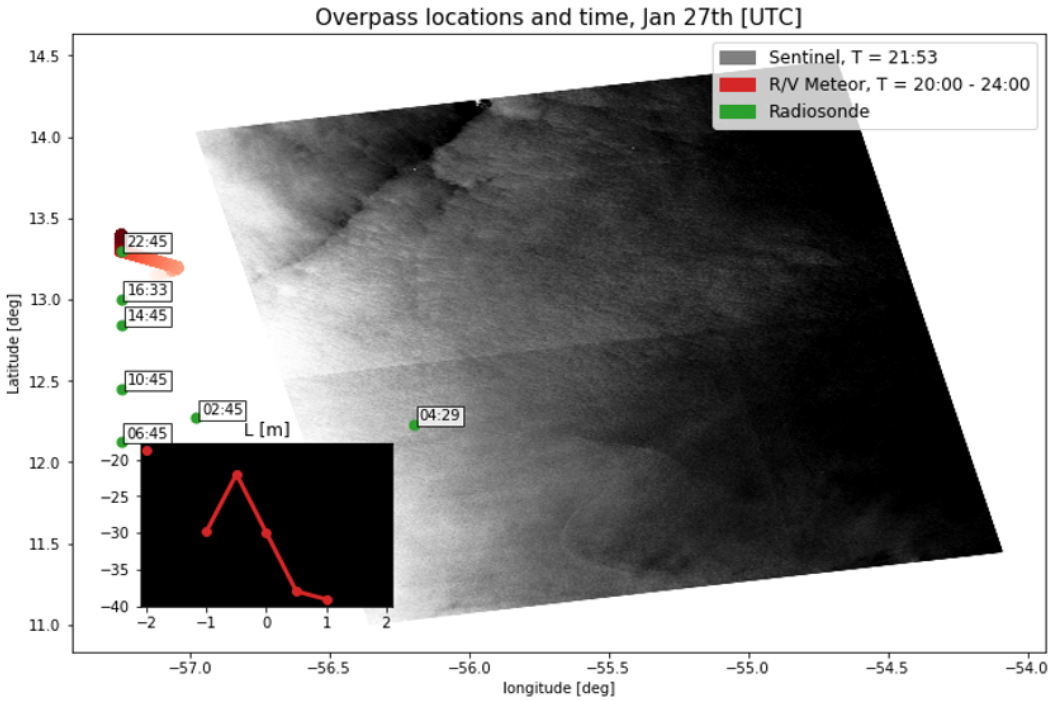

Figure A.4: Contains two radar scenes. Jan 27th B located north of Jan 27th A.

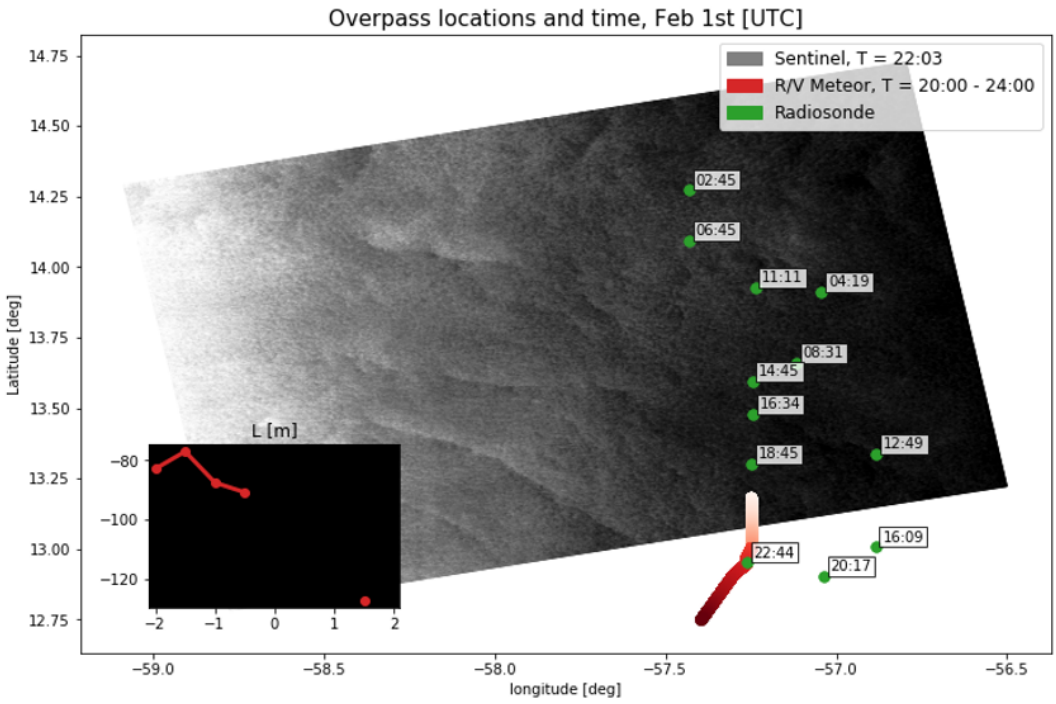

Figure A.5

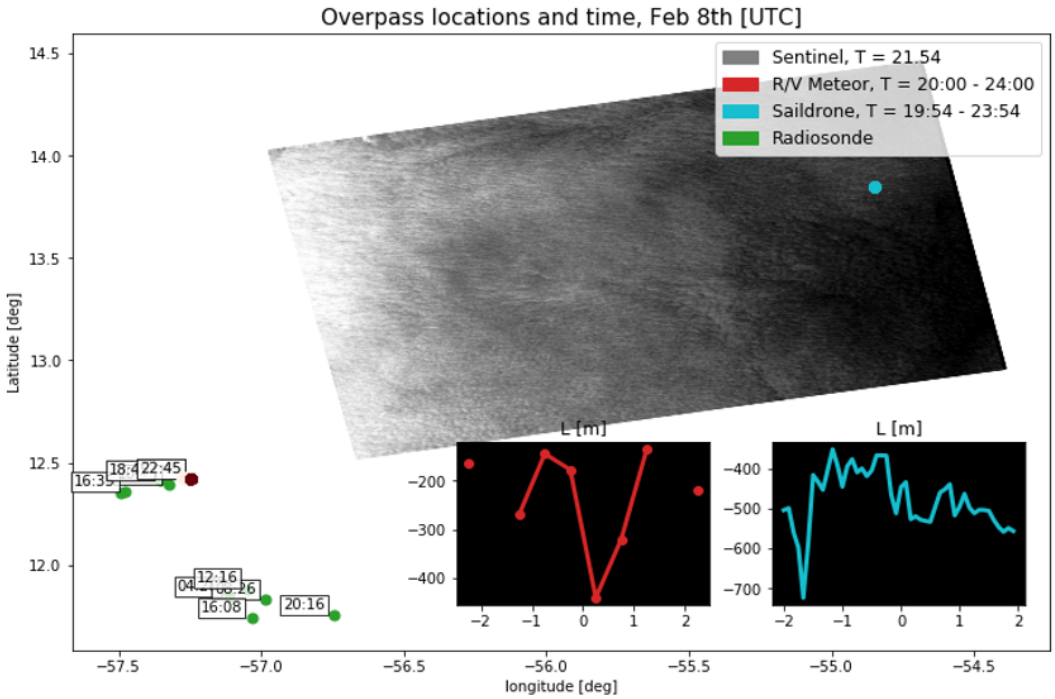

Figure A.6: location R/V Meteor hidden near radiosonde time stamp 22:45.

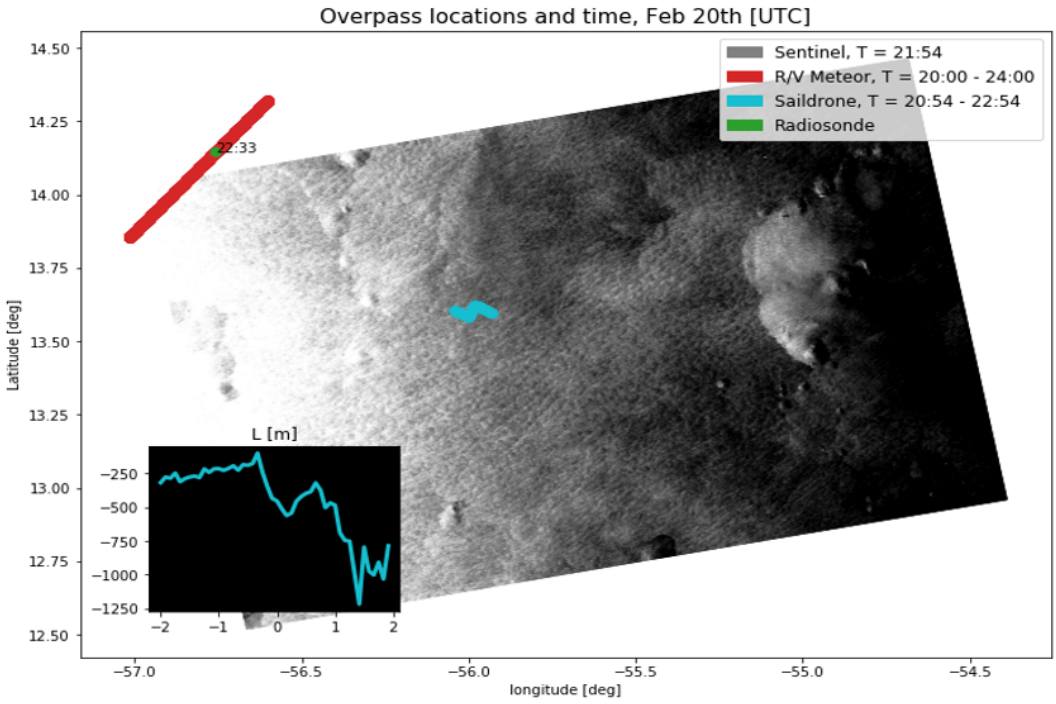

Figure A.7

A.4 Extended locations validation data

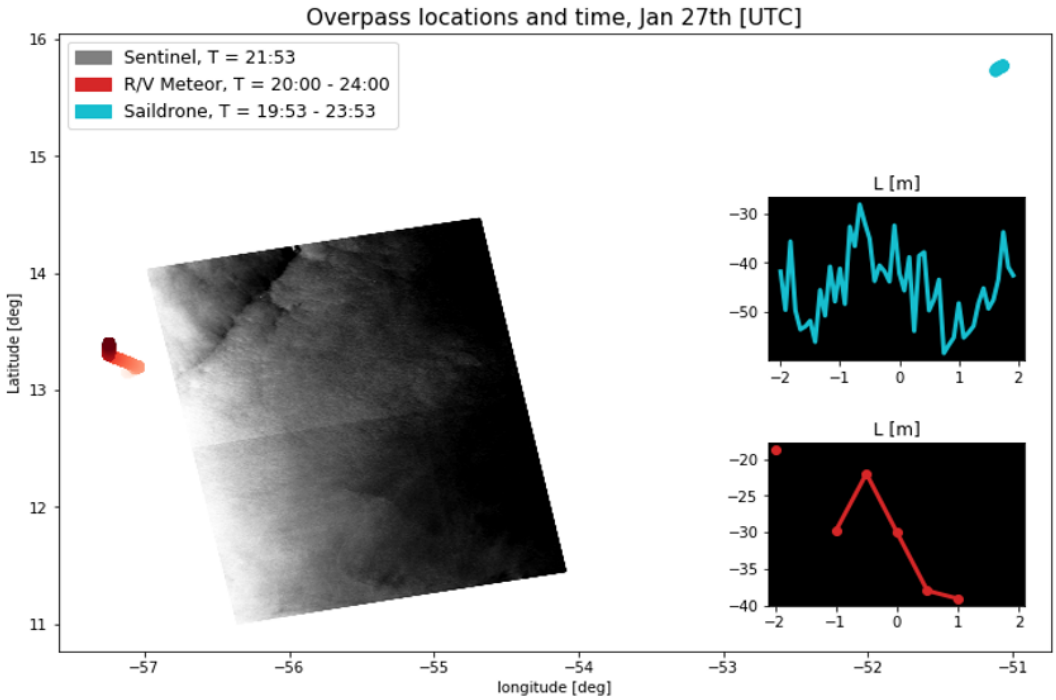

Figure A.8

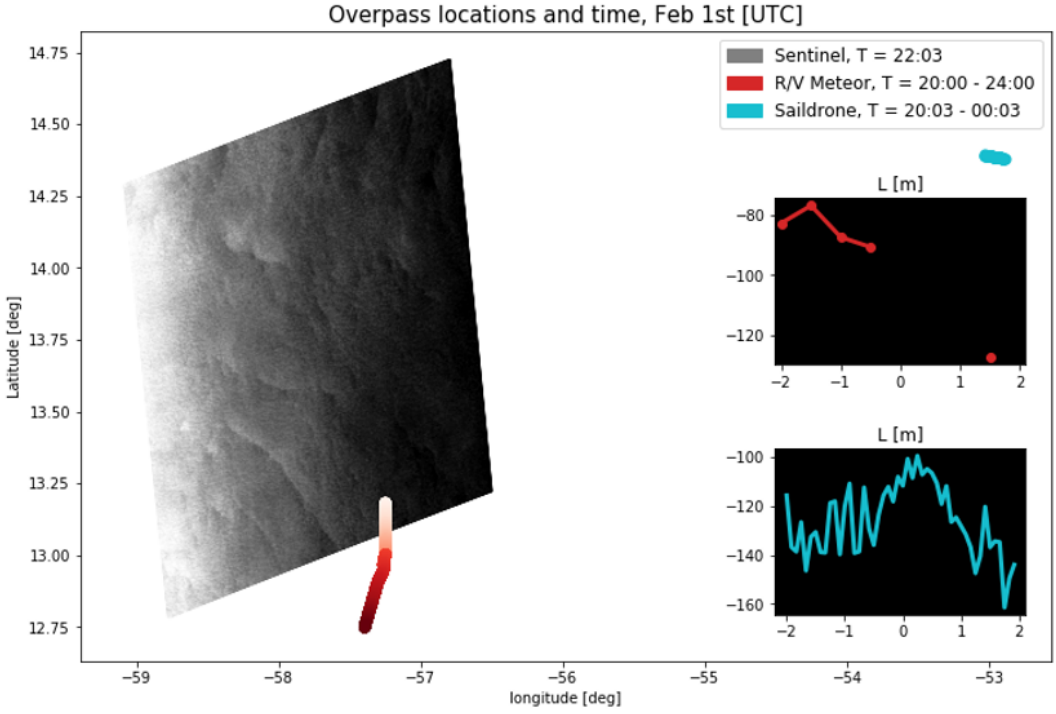

Figure A.9

A.5 Spatial distribution results

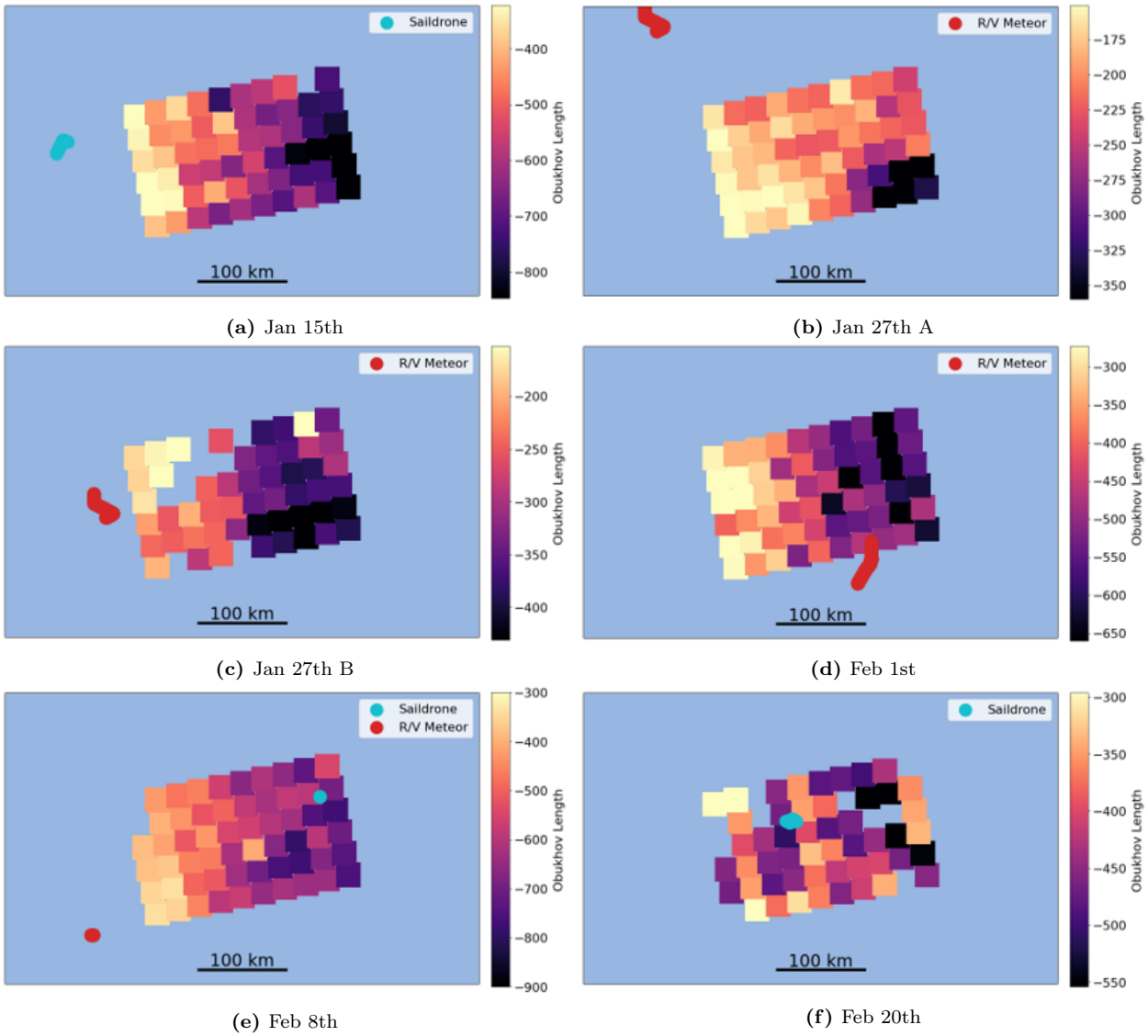

(a) Jan 15th

(b) Jan 27th A

(c) Jan 27th B

(d) Feb 1st

(e) Feb 8th

(f) Feb 20th

Figure A.10: Spatial distribution of L derived for Sentinel-1 scenes in the Barbados study area using scenario 2 of algorithm 2B. Location of nearby validation sources included for two hour pre and post Sentinel-1 observation time.

A.6 Miscellaneous

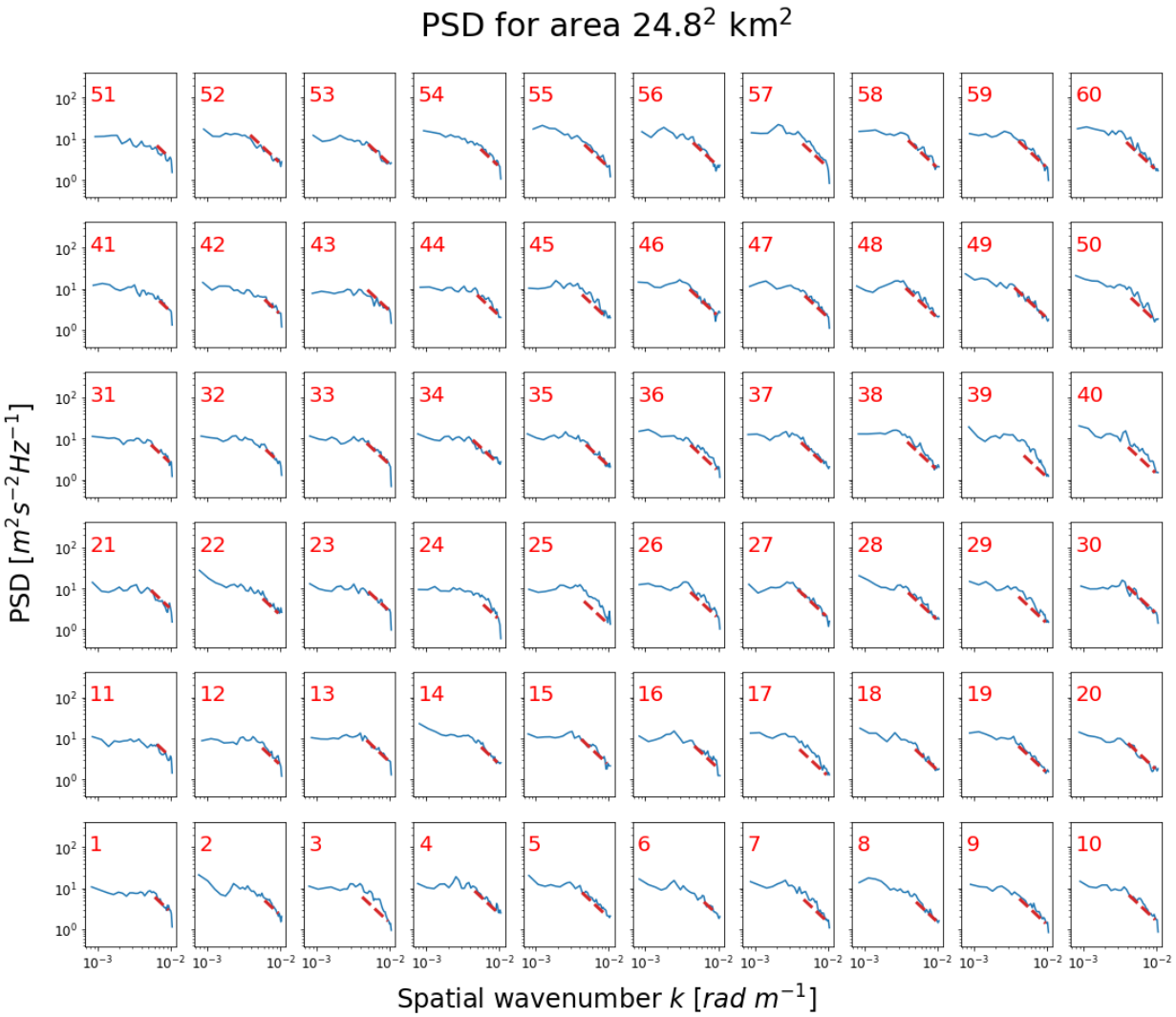

Figure A.11: Calculated 1D spectra for each tile of scenario 2 results for Jan 27th A. Dashed red line indicates a -5/3 power law.